FINAL REPORT

09121-3300-02.FINAL

Displacement & Mixing in Subsea Jumpers – Experimental Data & CFD Simulations
09121-3300-02

April 22, 2013

Principal Investigator
Dr. Michael Volk
Associate Vice President of Research & Technology Development
The University of Tulsa
800 South Tucker Drive
Tulsa, OK 74104

LEGAL NOTICE

This report was prepared by the University of Tulsa, as an account of work sponsored by the Research Partnership to Secure Energy for America, RPSEA. Neither RPSEA members of RPSEA, the National Energy Technology Laboratory, the U.S. Department of Energy, nor any person acting on behalf of any of the entities:

a. MAKES ANY WARRANTY OR REPRESENTATION, EXPRESS OR IMPLIED WITH RESPECT TO ACCURACY, COMPLETENESS, OR USEFULNESS OF THE INFORMATION CONTAINED IN THIS DOCUMENT, OR THAT THE USE OF ANY INFORMATION, APPARATUS, METHOD, OR PROCESS DISCLOSED IN THIS DOCUMENT MAY NOT INFRINGE PRIVATELY OWNED RIGHTS, OR

b. ASSUMES ANY LIABILITY WITH RESPECT TO THE USE OF, OR FOR ANY AND ALL DAMAGES RESULTING FROM THE USE OF, ANY INFORMATION, APPARATUS, METHOD, OR PROCESS DISCLOSED IN THIS DOCUMENT.

THIS IS A FINAL REPORT. THE DATA, CALCULATIONS, INFORMATION, CONCLUSIONS, AND/OR RECOMMENDATIONS REPORTED HEREIN ARE THE PROPERTY OF THE U.S. DEPARTMENT OF ENERGY.

REFERENCE TO TRADE NAMES OR SPECIFIC COMMERCIAL PRODUCTS, COMMODITIES, OR SERVICES IN THIS REPORT DOES NOT REPRESENT OR CONSTIITUTE AND ENDORSEMENT, RECOMMENDATION, OR FAVORING BY RPSEA OR ITS CONTRACTORS OF THE SPECIFIC COMMERCIAL PRODUCT, COMMODITY, OR SERVICE.

ABSTRACT

This study involves the experimental and computational study of the mixing and displacement phenomena that take place during hydrate inhibition of jumper type configurations using monoethylene-glycol (MEG) and methanol. All experiments were conducted in a three-inch jumper system at the University of Tulsa Hydrate Formation Project.

This thesis presents the experimental results with respect to effect of inhibitor type, injection rate, brine salinity and liquid loading. Different dispersion and partitioning mechanisms were observed for methanol and MEG, especially in the vertical sections and low spots. Repeated MEG tests were conducted with Labview® data historian system installed after improving the jumper facility. Methanol displacement tests were conducted following the tests matrix, and conclusions were made based on the experimental results. Methanol overriding the water phase at both horizontal low spots was observed for the low velocity experimental cases. Low pressure hydrates formation tests with cyclopentane were also conducted under different inhibited environments. Hydrates grow rapidly after nucleating at the cyclopentane - water interface. Slurry mass that formed in the elbow was permeable to gas but not liquid. More hydrates formed in the elbow of first low spot.

Simulations using 1D transient multiphase flow simulator OLGA were conducted to evaluate its capacity to predict the thermodynamic inhibitor dispersion by using the inhibitor tracking module. Large discrepancy between OLGA simulation results and experimental data exists for low injection rate cases. Computational fluid dynamic (CFD) simulations help optimize the amount and flow rates of chemicals required as well as to optimize the location of the injection ports. The results are presented for the miscible displacement of thermodynamic inhibitors (THI) in

the jumper configurations. The 2D CFD simulations were performed with the commercial software FLUENT® 6.3.26. Comparisons were made between the simulation results and experimental data from full fresh water loading jumper displacement tests with MEG and methanol. Both 2D and 3D CFD simulations provide reasonable prediction for THI distribution along the jumper after displacement test, except that neither was able to reproduce methanol overriding water phase at both low spots. The results obtained by Star-CCM+ 3D generally gave better agreement with the results from the experiment.

Signature

4/22/13
Date

Michael Volk, Principal Investigator
University of Tulsa
Associate Vice President of Research and Technology Development

THIS PAGE INTENTIONALLY LEFT BLANK

TABLE OF CONTENTS

Page

ABSTRACT 1

LIST OF TABLES 6

LIST OF FIGURES 6

CHAPTER 1: INTRODUCTION 9
1.1 Problem statement 10
1.2 Scope of work 12

CHAPTER 2: LITERATURE REVIEW 14
2.1 Hydrates in offshore production 16
2.2 Hydrate control methods 18
2.2.1 Dehydration 19
2.2.2 Heating and insulation 19
2.2.3 Inhibitor injection 21
2.3 Hydrate-related computational fluid dynamics studies 28

CHAPTER 3: EXPERIMENTAL FACILITY AND PROGRAM 32
3.1 Experimental jumper facility 32
3.1.1 Jumper facility description 32
3.1.2 Special provisions for MeOH tests 39
3.2 Experimental program 40
3.2.1 THI operating procedure 40
3.2.2 THI displacement experiments 42
3.2.3 Cyclopentane hydrate experiments 43

CHAPTER 4: EXPERIMENTAL RESULTS 46
4.1 MEG displacement tests results 46
4.1.1 Comparison with Mele's results 46
4.1.2 Displacement tests with MEG and fresh water 49
4.1.3 Displacement tests with MEG and 12 percent brine 51
4.1.4 Visual observations 53
4.2 Methanol displacement tests results 54
4.2.1 Displacement tests with methanol and fresh water 54
4.2.2 Displacement tests with methanol and 12 percent brine 58
4.2.3 Visual observations 59
4.3 Comparison between methanol and MEG tests 61
4.4 Cyclopentane hydrates experiments 64
4.4.1 Run No.1: Fresh water and cyclopentane 66
4.4.2 Run No.2: 3.5 percent Brine and cyclopentane 67
4.4.3 Run No.3: 12 percent MEG and cyclopentane 69
4.4.4 Run No.4: Fresh water and cyclopentane in both low spots 70

CHAPTER 5: SIMULATION RESULTS 72
5.1 OLGA simulations 72
5.1.1 OLGA inhibitor tracking module 72
5.1.2 OLGA simulation setup 74

5.2 CFD (FLUENT®) simulations 84
5.2.1 CFD model description 84
5.2.2 FLUENT® simulation results with MEG 90
5.2.3 FLUENT® simulation results with methanol 92
5.3 3D CFD (STAR-CCM+®) simulations by CD-Adapco 100
5.3.1 CFD 3D (STAR-CCM+) simulations for MEG 101
5.3.2 CFD 3D (STAR-CCM+) simulations for methanol 102
5.4 Comparisons among 1D, 2D and 3D simulations for THI displacement tests 103
5.4.1 Comparison among 1D, 2D, 3D simulations for MEG displacement tests ... 103
5.4.2 Comparison among 1D, 2D, 3D simulations for methanol displacement tests 107
CHAPTER 6: CONCLUSIONS AND RECOMMENDATIONS 109
REFERENCES 114
APPENDIX A 117
APPENDIX B 120
APPENDIX C 123
APPENDIX D 124
APPENDIX E 125

LIST OF TABLES

Page

TABLE 2- 1: SUMMARY OF THE LITERATURE REVIEW FOR GAS HYDRATES 14
TABLE 2- 2: APPROACHES FOR ELECTRICAL HEATING TECHNIQUES 20
TABLE 2- 3: THE ADVANTAGES AND DISADVANTAGES OF THI APPLICATION (COCHRAN, 2003) 21
TABLE 3 - 1: CHARACTERISTICS OF THE INHIBITOR INJECTION PUMP 35
TABLE 3 - 2: PARAMETERS OF JUMPER LABVIEW HISTORIAN SYSTEM 38
TABLE 3 - 3: TEST PARAMETERS FOR INHIBITOR DISPLACEMENT TESTS 43
TABLE 3 - 4: TEST MATRIX FOR CYCLOPENTANE HYDRATE EXPERIMENTS 45
TABLE 4 - 1: METHANOL DISPLACEMENT TESTS WITH FRESH WATER - FULL LIQUID LOADING 55
TABLE 4 - 2: METHANOL AND MEG RADIAL CONCENTRATION PROFILE AT THE 1ST LOW SPOT FRESH WATER (FULL LIQUID LOAD – ONE JUMPER VOLUME DISPLACED) 63
TABLE 4 - 3: METHANOL AND MEG RADIAL CONCENTRATION PROFILE AT THE 2ND LOW SPOT (FRESH WATER – FULL LIQUID LOAD – ONE JUMPER VOLUME DISPLACED) 64
TABLE 4 - 4: TEST MATRIX FOR CYCLOPENTANE HYDRATE EXPERIMENTS 66

LIST OF FIGURES

Page

FIGURE 2- 1: HYDRATE STRUCTURES (SLOAN, 2000) 15
FIGURE 2- 2: A LARGE GAS HYDRATE PLUG FORMED IN A SUBSEA HYDROCARBON PIPELINE. PICTURE FROM PETROBRAS (BRAZIL) 17
FIGURE 2- 3: HYDRATE EQUILIBRIUM CURVE FOR A TYPE II GAS 18
FIGURE 2- 4: CHEMICAL STRUCTURE OF A MONOETHYLENE GLYCOL MOLECULE ($C_2H_6O_2$) (SOURCE: WIKIPEDIA) 22
FIGURE 2- 5: DENSITY OF MONOETHYLENE GLYCOL AS A FUNCTION OF TEMPERATURE (FERNANDEZ-SEMPRE ET AL., 1966) 23
FIGURE 2- 6: VISCOSITY OF MONOETHYLENE GLYCOL AS A FUNCTION OF TEMPERATURE (FERNANDEZ-SEMPRE ET AL., 1966) 23
FIGURE 2- 7: CHEMICAL STRUCTURE OF METHANOL MOLECULE (CH_3OH) (SOURCE: WIKIPEDIA) 24
FIGURE 2 - 8: DENSITY OF METHANOL AS A FUNCTION OF WEIGHT CONCENTRATION (LIDE ET AL., 1996) 26
FIGURE 2 - 9: VISCOSITY OF METHANOL AS A FUNCTION OF WEIGHT CONCENTRATION (LIDE ET AL., 1996) 26
FIGURE 3 - 1: JUMPER TEST SECTION LAYOUT 33
FIGURE 3 - 2: LOCATION OF SAMPLING PORTS ALONG THE JUMPER TEST SECTION 34
FIGURE 3 - 3: INHIBITOR INJECTION SYSTEM 36
FIGURE 3 - 4: COLLECTING TANKS AND BRINE TRANSFER PUMP 36
FIGURE 3 - 5: DIFFERENTIAL PRESSURE TRANSMITTERS AND THERMOCOUPLE 37
FIGURE 3 - 6: LABVIEW INTERFACE FOR THE JUMPER FACILITY 37
FIGURE 3 - 7: METTLER-TOLEDO DE40 DENSITY METER 39
FIGURE 3 - 8: NITROGEN PURGING SYSTEM FOR METHANOL STORAGE TANK 40
FIGURE 3 - 9: REPRESENTATION OF INITIAL LIQUID LOADINGS 43
FIGURE 3 - 10: LIQUID LOADING FOR HYDRATES FORMATION TESTS 45
FIGURE 4 - 1: COMPARISONS OF CONCENTRATION PROFILES OF MEG 47
FIGURE 4 - 2: COMPARISONS OF CONCENTRATION PROFILES OF MEG 48
FIGURE 4 - 3: COMPARISONS OF CONCENTRATION PROFILES OF MEG 48
FIGURE 4 - 4: DIMENSIONLESS CONCENTRATION PROFILES OF MEG 49
FIGURE 4 - 5: DIMENSIONLESS CONCENTRATION PROFILES OF MEG 50
FIGURE 4 - 6: DIMENSIONLESS CONCENTRATION PROFILES OF MEG 51

FIGURE 4 - 7: DIMENSIONLESS CONCENTRATION PROFILES OF MEG 52
FIGURE 4 - 8: SECTIONS OF JUMPER FOR OBSERVATION STUDY 54
FIGURE 4 - 9: DISPERSION AND DISPLACEMENT 54
FIGURE 4 - 10: EXPERIMENTAL MEOH CONCENTRATION PROFILES 56
FIGURE 4 - 11: COMPARISON OF MEG AND METHANOL CONCENTRATION PROFILES 57
FIGURE 4 - 12: EXPERIMENTAL MEOH CONCENTRATION PROFILES 59
FIGURE 4 - 13: METHANOL OVERRIDING WATER PHASE 60
FIGURE 4 - 14: METHANOL DISTRIBUTION 61
FIGURE 4 - 15: METHANOL MIXING 61
FIGURE 4 - 16: LIQUID ACCUMULATION ZONES DURING GAS RESTART (COLETTA, 2009) 65
FIGURE 4 - 17: CYCLOPENTANE HYDRATE EQUILIBRIUM CURVES 65
FIGURE 4 - 18: TEST PROCEDURE AND JUMPER OBSERVATIONS 67
FIGURE 4 - 19: TEMPERATURE TRACE FOR RUN NO.2 68
FIGURE 4 - 20: TEMPERATURE TRACE FOR RUN NO.3 69
FIGURE 4 - 21: TEMPERATURE TRACE FOR RUN NO.4 71
FIGURE 5 - 1: JUMPER GEOMETRY BUILT IN OLGA 75
FIGURE 5 - 2: OLGA 7 JUMPER SYSTEM LAYOUT 75
FIGURE 5 - 3: REPEATED EXPERIMENTAL VS. OLGA SIMULATED 78
FIGURE 5 - 4: EXPERIMENTAL VS. OLGA SIMULATED 79
FIGURE 5 - 5: OLGA MEG TRACKING MODULE PERFORMANCE, MELE (2010) 80
FIGURE 5 - 6: OLGA MEG TRACKING MODULE PERFORMANCE FOR REPEATED MEG TESTS 81
FIGURE 5 - 7: EXPERIMENTAL VS. OLGA® SIMULATED 83
FIGURE 5 - 8: GRID STRUCTURE AND JUMPER 2D GEOMETRY 84
FIGURE 5 - 9: CONTOUR OF MEG MASS FRACTION 90
FIGURE 5 - 10: EXPERIMENTAL AND CFD 2D SIMULATIONS COMPARISON 91
FIGURE 5 - 11: EXPERIMENTAL VS. FLUENT® SIMULATED CONCENTRATION PROFILES 92
FIGURE 5 - 12: EXPERIMENTAL VS. CFD PREDICTIONS 94
FIGURE 5 - 13: EXPERIMENTAL VS. CFD PREDICTIONS 95
FIGURE 5 - 14: CONTOUR OF METHANOL MASS FRACTION 96
FIGURE 5 - 15: CONTOUR OF METHANOL MASS FRACTION 97
FIGURE 5 - 16: EXPERIMENTAL RESULTS VS. PROFILES PREDICTED BY THE CFD MODEL 99
FIGURE 5 - 17: EXPERIMENTAL RESULTS VS. PROFILES PREDICTED BY THE CFD MODEL 99
FIGURE 5 - 18: CONTOUR OF METHANOL MASS FRACTION 100
FIGURE 5 - 19: MEG CONCENTRATION PROFILES VS. EXPERIMENTAL RESULTS 101
FIGURE 5 -20: MEG CONCENTRATION PROFILES VS. EXPERIMENTAL RESULTS 103
FIGURE 5 -21: DIFFERENCE IN INJECTION VELOCITY 105
FIGURE 5 -22: DIFFERENCE IN INJECTION VELOCITY 106
FIGURE 5 -23: DIFFERENCE IN INJECTION VELOCITY 106
FIGURE 5 -24: DIFFERENCE IN INJECTION VELOCITY 107
FIGURE 5 -25: COMPARISONS AMONG 1D, 2D AND 3D SIMULATIONS WITH METHANOL TESTS 108
FIGURE A - 1: COMPARISON RESULTS – MEG AND METHANOL AT 1 GPM 117
FIGURE A - 2: COMPARISON RESULTS – MEG AND METHANOL AT 5 GPM 118
FIGURE A - 3: COMPARISON RESULTS – MEG AND METHANOL AT 10 GPM 118
FIGURE A - 4: COMPARISON RESULTS – MEG AND METHANOL AT 20 GPM 119

FIGURE B - 1: COMPARISON RESULTS – 1 GPM 120
FIGURE B - 2: COMPARISON RESULTS – 5 GPM 121
FIGURE B - 3: COMPARISON RESULTS – 10 GPM 121
FIGURE B - 4: COMPARISON RESULTS – 20 GPM 122
FIGURE E - 1 - SYMMETRIC CROSS SECTIONS OF THE JUMPER 127
FIGURE E - 2 - DISCRETIZING THE JUMPER 128
FIGURE E - 3 - INCREASING THE NUMBER OF TIME STEPS INCREASES THE TEMPORAL ACCURACY OF THE SOLUTION IN THE JUMPER 129
FIGURE E - 4. – CONCENTRATION IN JUMPER 130
FIGURE E - 5 – SIMULATION RESULTS AT SAMPLE POINT 1 131
FIGURE E - 6 – SAMPLE RESULTS 132
FIGURE E - 7 – SAMPLE RESULTS 133
FIGURE E - 8 – SAMPLE RESULTS 135
FIGURE E - 9 - COMPARISON OF MEG INJECTION EXPERIMENTS TO CORRESPONDING SIMULATIONS. 137
FIGURE E - 10 – MEG EXPERIMENT – 1 GPM 138
FIGURE E - 11 – GRAVITY SETTLING EFFECT 139
FIGURE E - 12 – MEG SIMULATIONS AND EXPERIMENTS AT 5 GPM 140
FIGURE E - 13 – GRAVITY SETTLING EFFECT – 2% CONCENTRATION CHANGE 141
FIGURE E - 14 – MEG EXPERIMENT AND SIMULATION AT 10 GPM 142
FIGURE E - 15 – GRAVITY SETTLING EFFECT 143
FIGURE E - 16 – MEG EXPERIMENTS AT 20 GPM 144
FIGURE E - 17 – METHANOL SIMULATION RESULTS 145
FIGURE E - 18 – 1 GPM MEOH SIMULATION 146
FIGURE E - 19 – 5 GPM MEOH SIMULATION 147
FIGURE E - 20 – 10 GPM MEOH SIMULATION 148
FIGURE E - 21 – 20 GPM MEOH SIMULATION 149
FIGURE E - 22 – COMPARISON OF EXPERIMENTAL DATA AND EQUIVALENT VOLUME FLOWED SIMULATION RESULTS 150

CHAPTER 1: INTRODUCTION

Nowadays, the risk of gas hydrate formation has become a major concern for offshore flow assurance. Hydrate formation can cause blockage of production lines and subsea equipment. According to DeepStar, five to eight percent of the total operating cost is estimated to be spent on inhibiting the formation of gas hydrates by the oil and gas industry (Desselles et al., 2011). The replacement of hydrate-plugged lines in Gulf of Mexico deep water environments costs one million dollars per mile on average (Chandrageupthan, 2011). In offshore production systems, hydrates may form when light hydrocarbons and water are present under certain pressure and temperature condition. These conditions for hydrate formation commonly occur during transient operations, for example, shutdown and restart conditions due to low temperatures, but they may also be encountered under steady-state production conditions. Subsea jumpers are commonly employed to connect the flowline to a manifold, tree, PLET (pipeline end termination), sled, or even another pipeline. Due to their characteristic configuration with small diameters (in comparison with production and distribution lines) and low spots where the water is prone to accumulate, subsea jumpers are particularly susceptible to hydrate plugging.

Hydrate formation can reduce flow and even form a solid plug to block the production in a short time period. Remediation of gas hydrates is expensive and can be dangerous depending on the location and size of the blockage. This can cause severe failure, resulting in equipment damage, injury, and even loss of life. Current operational procedures to avoid the risk of hydrate plugging of subsea jumpers include installing insulation, electrical heating, dead crude oil displacement and injection of thermodynamic inhibitors (THI). Thermal methods (e.g., insulated flowlines, active heating) can be expensive, impractical, and/or ineffective under some conditions. The most common way to prevent hydrates is chemical inhibition. There are two main methods of chemical

inhibition: THI and low dosage hydrate inhibitors (LDHIs). Solutions of methanol (MeOH) and monoethylene-glycol (MEG) are most often employed as thermodynamic inhibitors.

1.1 Problem statement

The current practice in establishing a hydrate control strategy using thermodynamic inhibitors is primarily based on thermodynamic equilibrium data, previous operational guidelines and the application of safety factors. This conservative approach may in many cases have a negative impact on the project economics. In order to optimize the hydrate prevention procedures and reduce the associated capital and operational expenditures, other system characteristics should be taken into account. These characteristics include fluid properties (hydrocarbons, water and inhibitors), distribution of the phases and physical design/configuration of the particular subsea system.

In the case of jumper flushing with THI, an appropriate mixing of water and inhibitor is expected to prevent the formation of hydrate plugs. However, the rates at which these chemicals are completely mixed with the aqueous phase are not well defined. Density difference and viscosity play an important role in determining if the inhibitor and water are sufficiently mixed. The presence of a third immiscible phase (e.g., heavy oil), may also hinder the physical contact between the MEG or methanol and the water. Gravity also has an effect on the degree of diffusion of inhibitors into the water, particularly in upward sections of jumper configurations. A better understanding of the interactions between these factors would contribute to optimizing the dispersion mechanism, minimizing operational risks, reducing the size of umbilicals and decreasing capital costs related to equipment and chemicals.

Another challenge is to determine the operational envelope of MEG and methanol with regard to hydrate inhibition in subsea jumpers. Recycling and environmental aspects should be taken into account, but also the effect of the inhibitor's physical properties on hydrate prevention

and remediation. For instance, since MEG is denser than water it might be more effective at dissociating a hydrate plug at the bottom of a water column. Conversely, the density of methanol is less than water which will assist it in rising through a water column to reach a hydrate blockage located higher up a riser if injected at the bottom. As mentioned earlier, density and viscosity differences may also affect the mixing process during inhibition. A lighter phase injected on top of the water might require a strong forced convection be applied (i.e., high velocity) to obtain a favorable dispersion of the inhibitor in water. Efforts are needed that would investigate and compare the suitability and effectiveness of MEG and methanol in jumper flushing procedures.

Although transient simulation models have been extensively used to design and evaluate subsea jumpers/flowlines as well as to address the interaction between production chemistry and multiphase flow during restart operations, a better insight into the complex physical phenomena taking place is required to explore all the potential variables and their resulting effects on operability and system performance. In order to manage the uncertainty linked to 1D models, more experimental data is required as well as the use of 2D or 3D codes capable of simulating the complex interaction of liquids and gases with surfaces defined by boundary conditions.

Computational fluid dynamics (CFD) offers the possibility of improving the design process of subsea components by tackling issues early in the engineering project. Likewise, numerical analysis enables one to study in depth the mixing and displacing mechanisms that occur during jumper flushing operations in order to optimize key factors such as the position of the injection port and the flow rate of a required chemical inhibitor. This study involves the experimental and computational assessment of the mixing and displacement phenomena that take place during hydrate inhibition of jumper type configurations using MEG and methanol. The experimental studies allow visual observation of the flow and diffusion behavior inside the jumper test section upon restart as well as the concentration profile of inhibitors throughout the system. The results

from the experimental runs serve as input to set up the CFD simulation and to validate the model once constructed. In addition, findings from the experiments will help to define the range of inhibitor velocities that favor mixing and the range of flow rates promoting the displacement of water out of the system. Since CFD simulations enable a better insight into the physical phenomena of jumper inhibition, the use of this engineering tool might help optimize the amount and flow rates of production chemicals required and optimize the location of the injection ports.

1.2 Scope of work

The scope of this project involves conducting experimental and modeling work to investigate and compare the suitability and effectiveness of MEG and methanol on inhibiting and displacing the water in jumper type configurations during flushing procedures. A better understanding of the displacement and mixing mechanisms would help select the most appropriate inhibitor and help to define the range of inhibitor flow rate that favor mixing and promote the displacement of water out of the system.

Chapter 2 is a literature review of hydrates issues in offshore production, hydrate inhibition methods, and CFD approach to study hydrate-related problems.

Chapter 3 describes the experimental facility and laboratory equipment used in this study. Parameters in the test matrix include different liquid loadings, inhibitor injection rates, water salinity and amount of MEG and methanol to be added in terms of volumes of jumper displaced.

The experimental results are presented and discussed in Chapter 4. Low pressure hydrate formation results with cyclopentane are also presented in Chapter 4.

In Chapter 5, different modeling approaches are presented and compared to the experimental results. Commercial software (OLGA from SPT Group) is used to conduct 1-D simulations, while a

2-D CFD model (FLUENT) is used to study the flow behavior and mixing during flushing with inhibitors. A 3-D CFD model using Star-CCM+ has also been used to model the experiments. Chapter 5 discusses the modeling effort and describes the performance of the different models.

Finally, Chapter 6 summarizes the conclusions of this research and provides recommendations for future studies.

CHAPTER 2: LITERATURE REVIEW

A hydrate is a physical combination of water and other small molecules to produce a solid which has an ice-like appearance but possesses a different structure than ice. In oil and gas production, hydrate formation is favored at low temperature and high pressure with free water and natural gas, which is the case deep in water environments. During the first 100 years after the discovery of gas hydrates, the interest in these compounds was essentially academic. Identification of the species that can form hydrates and the pressure temperature conditions at which the formation occurs was the main research focus.

In 1934, when the oil and gas industry in the United States was growing rapidly, it was recognized that the plugging of natural gas pipelines was due not to ice formation but to formation of clathrate hydrates of natural gas (Hammerschmidt, 1934). Powell (1948) at the University of Oxford was the first to describe the clathrate structure and named clathrate compounds those inclusion compounds in which two or more components are associated without ordinary chemical union but through complete enclosure of one set of molecules in a suitable structure formed by another. Hagan (1962) and Atwood et al. (1984) published comprehensive coverage of the subject of inclusion compounds. Table 2-1 summarizes the literature review for gas hydrates from previous studies.

TABLE 2- 1: SUMMARY OF THE LITERATURE REVIEW FOR GAS HYDRATES

Author	Reviewed topic
Mandelcorn (1959)	The structure, molecular and thermodynamic properties, and uses of clathrates
Van der Waals and Platteeuw (1959)	Knowledge on clathrate hydrates and presented a model to describe the chemical potential of water in the hydrate
Byk and Pomina (1968)	The structure and properties

Hand et al. (1974)	A general view of gas hydrates
Davidson (1973)	The most comprehensive review on the properties and structures
Jeffrey and McMullan (1967, 1984a)	The structure of clathrate hydrates
Holder et al. (1988)	The gas hydrate equilibrium predictive methods

Natural gas hydrates typically form one or more of the following three crystal structures: cubic structure I (sI), cubic structure II (sII), and hexagonal structure H (sH), as shown in Figure 2-1. Structure I is formed with small molecules such as methane, ethane. Structure II is formed with larger molecules such as propane. Structure H is formed with even larger molecules such as iso-pentane when accompanied by other small molecules.

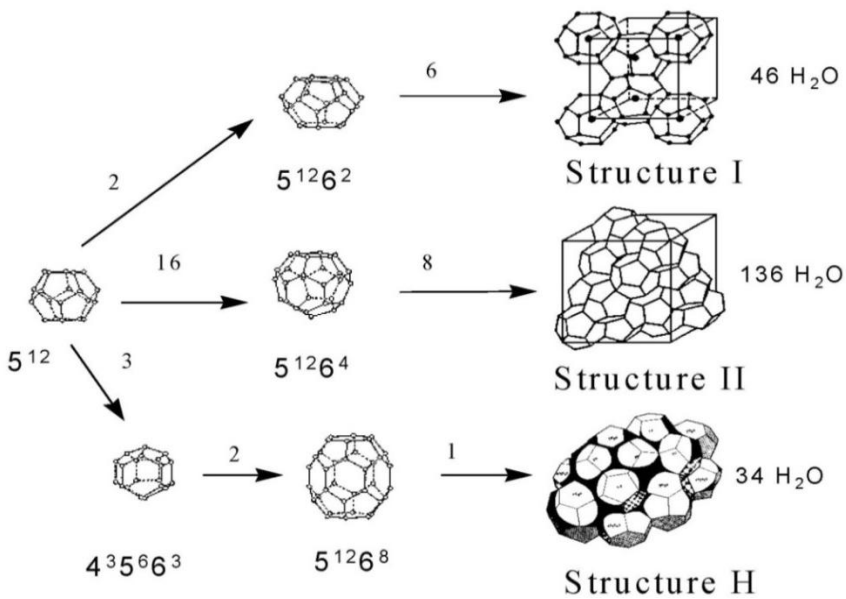

FIGURE 2- 1: HYDRATE STRUCTURES (SLOAN, 2000)

2.1 Hydrates in offshore production

Hydrate formation poses a serious threat to production systems during flowing and shut-in conditions. In his Hydrate Engineering, Sloan (2000) presents several case studies where the equipment was severely damaged and lives were lost during an attempt to dissociate a hydrate plug. Even though engineers try to design hydrate free systems, they still do occur on a regular basis. Figure 2-2 shows an ice-like hydrate plugs formed in a subsea hydrocarbon pipeline in Brazil offshore production. Figure 2-3 illustrates a typical hydrate equilibrium curve. To the right of the curve, hydrates are thermodynamically unstable. The production system will be safe from hydrate blockages by operating in this region. To the left of the curve, hydrates are thermodynamically stable and tend to form hydrate plugs.

Hydrate issues may come up during normal production; however, transient operations are more easily at risk of hydrate formation. For example, during a shut-in, the temperature of the subsea flowline decreases to the ambient temperature (typically 40 $^{\circ}$F). Hydrates readily form under these high pressures and low temperatures in offshore deepwater systems. During shut-in, hydrates form in a thin brittle layer at the water/oil interface. Upon restart, the agitation breaks the hydrate layer and allows mixing of the super cooled water and gas, leading to rapid hydrate formation and possible blockages downstream of where the water is prone to accumulate (Ellison et al., 2000). Hydrate plug risk increases as the water cut increases, because sufficient hydrate particles can contact each other and stick together.

FIGURE 2- 2: A LARGE GAS HYDRATE PLUG FORMED IN A SUBSEA HYDROCARBON PIPELINE. PICTURE FROM PETROBRAS (BRAZIL)

Hydrate blockages are more likely to be formed at low spots where water tends to accumulate in an offshore production system (Coletta, 2009). Kinnari et al. (2006) presented important conclusions related to hydrate formation tendencies of subsea templates and spools during restart. In this work, the locations where growing hydrate restrictions are prone to occur in a jumper-type configuration were also identified. The study also determined that hydrates particles were transported far away from the contact location between the gas and the aqueous phase, even at low water loadings corresponding to roughly the low spot volume. Estanga's (2007) study at The University of Tulsa focused on restarts in low spots. Research showed that at lower restart velocity less permeable plugs were formed. Meanwhile, plugs developed during segregated conditions tend to travel and form further downstream. Moreover, higher salinities did not prevent plugging but they played the role of delaying the formation of plug. Anti- agglomerants were tested to be effective if injected prior to shut-in.

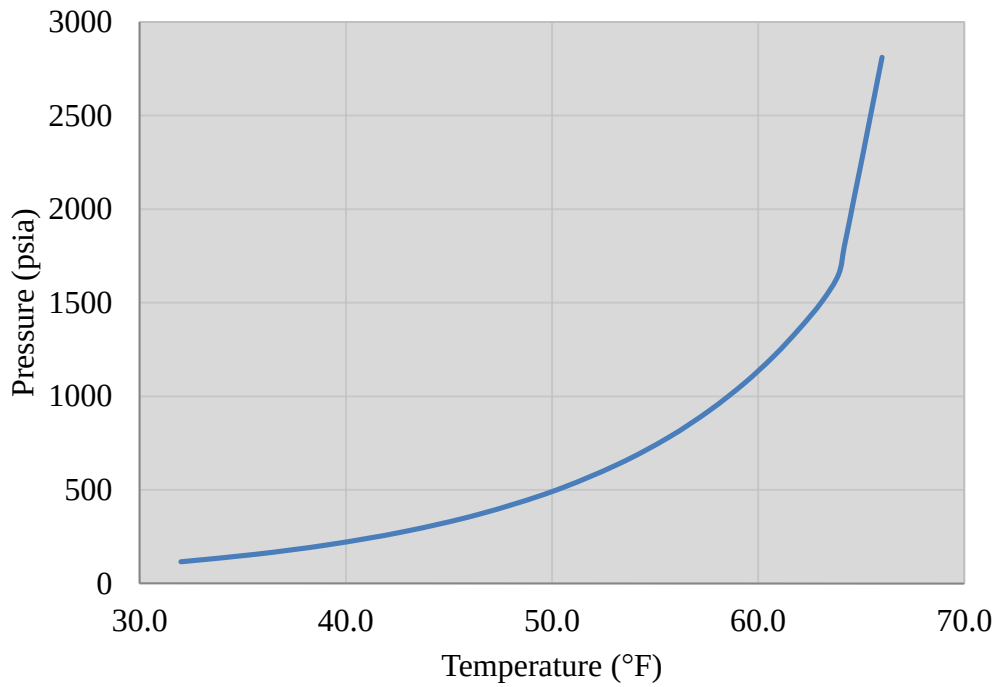

FIGURE 2- 3: HYDRATE EQUILIBRIUM CURVE FOR A TYPE II GAS

2.2 Hydrate control methods

Hydrate control and remediation is one of the biggest flow assurance issues in deepwater oil field developments. A great amount of effort is usually invested in the design phase to develop the production system and achieve hydrate control. Cochran (2003) provided a design guide for evaluating hydrate control and remediation techniques for concept selection and feasibility work. The most risky locations for hydrates to form and accumulate are low spots, where water tends to accumulate, points of gas expansion, where cooling from Joule-Thomson effect cools the fluids down below the hydrate formation temperature and points of changes in geometry for flow obstructions. To prevent problems related to hydrates, it is necessary to implement hydrate control methods. Some of these methods are described in this section.

2.2.1 Dehydration

Dehydration is an essential procedure in the processing of natural gas to meet pipeline specifications. Water removal is commonly required to prevent condensation of an aqueous phase which can lead to hydrate formation and corrosion in the gas system (Hubbard, 1991). The removal of water from natural gas can be accomplished mainly in three commercial methods: adsorption (glycol dehydration), adsorption (dry desiccant), and condensation (glycol/methanol injection). The first two ways utilize mass transfer of the water molecule into a liquid solvent to a crystalline structure. Molecular sieves are crystalline solids designed to adsorb specific molecules, in this case water. They are commonly found in low temperature processes, such as turbo-expander discharge temperatures less than -150°F. The third method employs cooling to condense the water molecule to the liquid phase with the subsequent injection of inhibitor to avoid hydrates. The most common method of gas dehydration is to use a tri-ethylene glycol (TEG) absorber. Tri-ethylene glycol absorbs water from the gas through hydrogen bonding. Contact between TEG and gas is performed in a packed or tray column. The TEG is transferred to a regeneration unit where water is recovered before recycling it to the absorber.

2.2.2 Heating and insulation

Active heating techniques include electrical heating, hot fluid circulation and hot oil circulation. These methods have been applied to deepwater flowlines and risers. Thermal insulation is commonly combined to minimize power requirements. Electrical heating can be employed for continuous operation, shutdown and restarts. Table 2-2 summarizes different approaches for electrical heating techniques. Hot oil circulation is a more common technique applied to restart cold production systems. Hot dead oil is circulated through dual flowlines and risers until they have warmed above hydrate forming conditions. The wells can be restarted once the flowlines and risers

are warm. Esaklul et al. (2003) presented a field application of active heating control in deepwater flowlines and proved active heating was a practical and effective method to control hydrates during production and short-term shutdowns. However, offshore pipelines can be very long and heating the pipe can be very cost-prohibitive. In reality, other hydrate prevention approaches are implemented into operational procedures.

Passive methods such as thermal insulation provide hydrate control by maintaining temperatures above hydrate formation conditions. Subsea equipment, like subsea trees, jumpers and manifolds, are normally insulated in deepwater oil developments with syntactic foam. The insulation material must withstand the hydrostatic pressure imposed in deepwater for offshore system with external insulation. The cost of insulation systems per unit length increases with decreasing overall heat transfer coefficient.

TABLE 2- 2: APPROACHES FOR ELECTRICAL HEATING TECHNIQUES

Direct heating	Pipe-in-pipe (PIP)
	Fully insulated single pipe (closed system)
	Earthed current single pipe (open system)
	Direct heating for pipe bundle
Indirect heating	Induction heating
	Trace heating

2.2.3 Inhibitor injection

2.2.3.1 Thermodynamic inhibitor (THI)

Thermodynamic hydrate inhibitors include glycols and methanol. THI prevents hydrate formation by reducing the temperature at which hydrates form by changing the chemical potential of the water. Table 2-3 includes the advantages and disadvantages of THI application.

Christiansen (2012) presented several case studies on the rate of hydrate inhibition in long subsea pipelines. Simplified HYSYS models of the upstream part of Ormen Lange and Snøhvit gas Fields on the Norwegian Continental Shelf were evaluated on calculating the injection rate and storage capacity of monoethylene glycol (MEG). His work concluded that hydrates form on the pipe wall in gas dominated pipelines, while they are formed in the bulk fluid in oil-dominated systems. The amount of inhibitor needed is influenced greatly by the heat transfer coefficient and the seabed temperature. MEG was proven to be better suited than MeOH as THI in these two long distance multiphase tie backs.

TABLE 2- 3: THE ADVANTAGES AND DISADVANTAGES OF THI APPLICATION (COCHRAN, 2003)

Advantages	Disadvantages
Reduced hydrate formation temperatures	Large quantities may be needed
Commercial codes are available to predict the effect of an inhibitor on the hydrate formation curve	Large storage volumes and pumping requirements are often required which can lead to significant capital costs
THI prevent hydrates under most conditions with sufficient quantities	Incompatibilities may exist between THI and other production chemicals such as wax or corrosion inhibitors
MeOH inhibits both liquid and vapor phases, which is advantageous during transient operations such as start-up	Incompatibilities may exist between THI and materials of construction such as umbilical
THI works for any hydrocarbon system	THI may cause salts to precipitate from the produced water

- Monoethylene glycol (MEG)

Monoethylene glycol is a colorless, practically odorless, low-volatility liquid that is completely miscible with water and many organic fluids. Its molecular weight, density and viscosity have been reported to be 62.07 g/mol, 1.113 g/cm^3 and 16.9 cP at 25°C (77°F), respectively. Figure 2-4 illustrates the chemical structure associated to a monoethylene glycol molecule. Physical properties of monoethylene glycol and MEG-water mixtures as a function of temperature are given in Figures 2-5 to 2-6. As depicted in these two figures, the viscosities of ethylene glycol and its aqueous solutions increases significantly as temperature decreases, which impose high energy requirements for its transport through subsea umbilicals.

FIGURE 2- 4: CHEMICAL STRUCTURE OF A MONOETHYLENE GLYCOL MOLECULE ($C_2H_6O_2$) (SOURCE: WIKIPEDIA)

Mele (2010) conducted experimental and modeling work in the University of Tulsa jumper facility with the aim of understanding the MEG displacement process as a function of different operational parameters, such as water cut, liquid loading, and injection rate. She found that glycol concentrations above 90 percent can be achieved when jumper configurations are flushed at sufficiently high superficial velocities (> 0.45 ft/s). Findings from this work agree with the experimental results obtained by Cagney et al. (2006). At low superficial velocities, less water is removed and inhibited against hydrate formation (concentrations below 50 percent were monitored in the second low spot). She also found that injecting more than one jumper volume of ethylene glycol did not improve significantly the level of water inhibition, particularly at high inhibitor flow

rates. Any additional flushing only resulted in displacing MEG out of the end of the wellhead jumper.

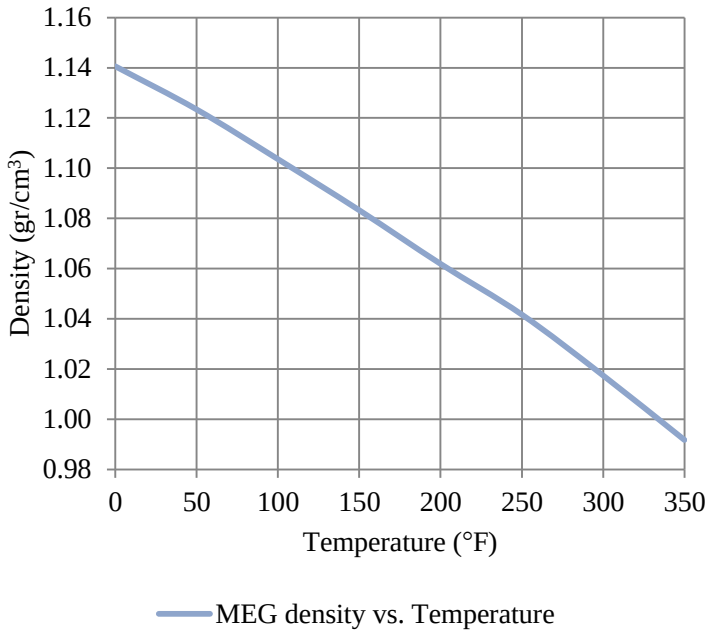

FIGURE 2- 5: DENSITY OF MONOETHYLENE GLYCOL AS A FUNCTION OF TEMPERATURE (FERNANDEZ-SEMPRE ET AL., 1966)

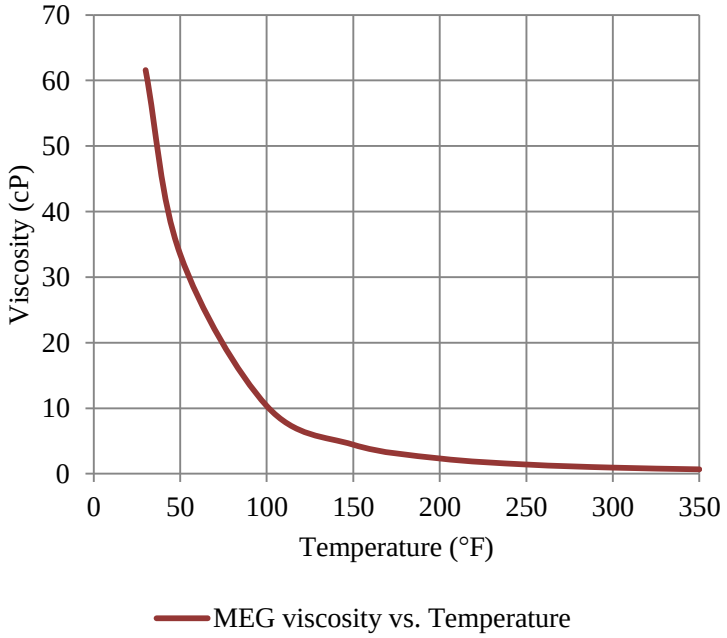

FIGURE 2- 6: VISCOSITY OF MONOETHYLENE GLYCOL AS A FUNCTION OF TEMPERATURE (FERNANDEZ-SEMPRE ET AL., 1966)

- Methanol (MeOH)

Methanol is a colorless alcohol, hygroscopic, and completely miscible with water, but much lighter (specific gravity 0.8). It is a good solvent, but very toxic and extremely flammable. This simple single-carbon alcohol is a volatile solvent and a light fuel. The use of methanol presents some safety and economic issues. MeOH is highly flammable with a flash point of 11°C, which indicates that MeOH presents a great safety risk with respect to handling and storage, especially on offshore installations with limited area. Moreover, MeOH burns with an invisible flame, which makes fire detection a more difficult problem. Methanol is very hazardous and large quantities must be stored on topsides facilities. Methanol is also difficult to recover from the oil phase and recently, refineries have started to impose penalties when the methanol content exceeds a certain amount. Figure 2-7 illustrates the chemical structure of methanol. The physical properties of methanol aqueous mixtures as a function of weight concentration are given in Figures 2-8 to 2-9.

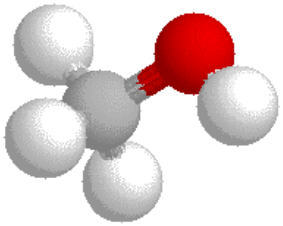

FIGURE 2- 7: CHEMICAL STRUCTURE OF METHANOL MOLECULE (CH_3OH) (SOURCE: WIKIPEDIA)

Methanol is the most commonly injected THI for oil systems. Compared to other thermodynamic inhibitors, methanol is more effective at reducing the hydrate formation temperature. It is less viscous and more effective for restarts. Overall, it is better for remediation of hydrate blockages. According to Cochran (2003), methanol can only protect equipment in the production system downstream of the injection point. It is also very important to determine the locations of the injection points. Cochran suggested the possible locations can be downhole

immediately above the SCSSV (surface-controlled subsurface safety valve), at the tree, or on the manifold. The cost of methanol varies from US$ 500 per BBL in the Gulf of Mexico to US$ 150 per BBL offshore West Africa (Loch, 2000).

Herrmann et al. (2004) conducted an experimental study to investigate the effect of varying the water cut, gas volume fraction, header inclination angle from horizontal, and the oil density. The distribution of methanol injected into a vertical wellbore was also examined. Uninhibited water remained in the header after methanol injection and no protection was provided against hydrate formation in all test cases. Diffusion of methanol into the water phase was really small and the methanol and water remained segregated. The study results can be also applied to determine the maximum amount of inhibitor that need to be pumped to inhibit a shut-in header section. The experiments conducted in their study provided some explanation for the insights to the timing of chemical injection. In this work, explanation for the success of this common practice of methanol inhibition was provided. Sufficient quantities of methanol injection can provide full protection against hydrate formation. However, an under-inhibited methanol system will exhibit accelerated kinetics of hydrate formation.

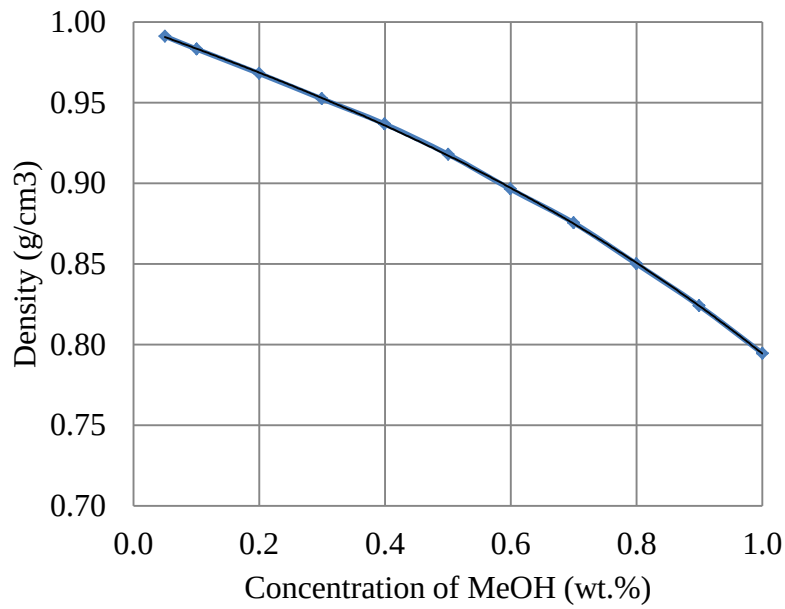

FIGURE 2 - 8: DENSITY OF METHANOL AS A FUNCTION OF WEIGHT CONCENTRATION (LIDE ET AL., 1996)

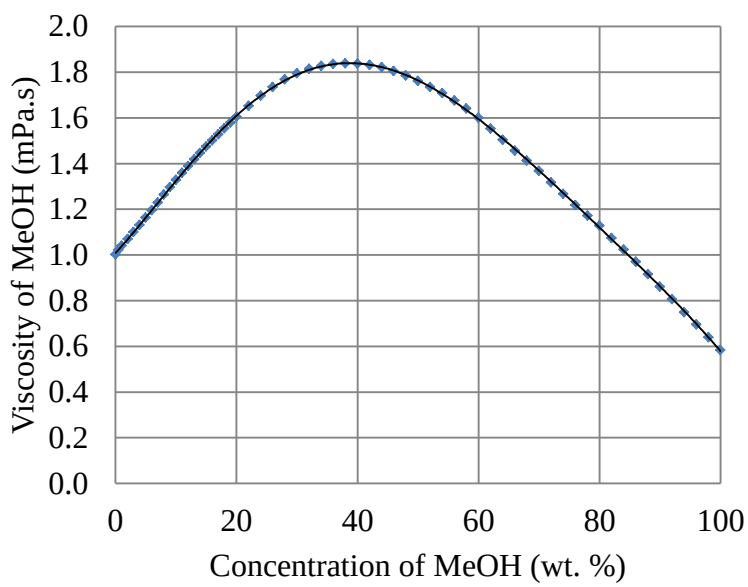

FIGURE 2 - 9: VISCOSITY OF METHANOL AS A FUNCTION OF WEIGHT CONCENTRATION (LIDE ET AL., 1996)

2.2.3.2 Low-dosage hydrate inhibitors

Low-dosage hydrate inhibitors (LDHI) have been introduced in industry recently. LDHI is more expensive than conventional inhibitors (methanol and glycol) on a per unit basis; however, they have become popular because only small quantities are required to inhibit hydrate formation. In addition to the savings in operating costs, implementation of low-dosage inhibitors is expected to reduce capital expenditures (Paez et al., 2001). LDHIs can be also combined with other types of chemical treatments, reducing the number of umbilicals needed.

Kinetic hydrate inhibitor (KHI) is one of the low-dosage inhibitors whose function is to interfere with the nucleation and growth process of hydrate crystals. Their efficiency is limited by time and sub-cooling. Kelland (1995) developed a curve showing the theoretical pressure-temperature limitations for use of hydrate inhibitors and a safe pressure/temperature region is delineated for low-dosage inhibitors known at the time the curve was constructed. Anti-agglomerants (AA) are polymers and surfactants, which are added at low concentrations (<1 wt. %). These chemicals allow hydrate formation, but prevent the agglomeration of hydrates so that the hydrate crystals do not grow large enough to plug flowlines, but are transportable as a slurry (Paez et al., 2001). AA's are very surface-active chemicals and sometimes create micro-emulsions. Anti-agglomerants only work in the presence of both water and liquid hydrocarbon phases, but the mechanism of inhibition has not been well understood. Kelland (1995) proposed that emulsification is the mechanism which prevents the hydrates from agglomerating. Increasing salinity or water cut (up to a maximum of 40 percent water by volume) decreases the effect of anti-agglomerants. Oil and condensate composition may also affect anti-agglomerant performance.

Even though low-dosage inhibitors appear to be a good replacement for thermodynamic inhibitors, only limited case studies of successful low-dosage inhibitor deployment have been

published. A successful field test with a combination anti-agglomerant/kinetic polymeric inhibitor in a gas producing well located in Canadian foothills was presented by Lovell et al. (2002).

2.2.3.3 Depressurization

To maintain system pressures low enough to be below the hydrate formation curve is referred as low pressure operation. The pressure normally needs to be 150 psia or less for deepwater with an ambient temperature of 39°F. Using depressurization instead of heating to bring the system outside the hydrate stable zone is easier except in the case of a liquid filled riser. The hydrostatic head exerted on the system present the pressure to be reduced outside the hydrate stability zone. Hydrate plugs must be depressurized from both sides to prevent accidents.

2.3 Hydrate-related computational fluid dynamics studies

Computational fluid dynamics (CFD) is widely used in the field of fluid flow, heat and mass transfer, chemical reactions, and related phenomena by solving numerically a set of governing equations including conversation of mass, momentum, energy. CFD has been extensively applied to the oil and gas industry to provide better understanding on the performance, design, and troubleshooting for reservoir design, drilling, production, and transport. CFD enables analysts to evaluate various design plans and to predict effects of process parameters variation. Its powerful post-processing functions are helpful to generate visual graphics to understand the physics of particle movement as well as predict the future hydrate deposition locations and potential hydrate plugging risk spots caused by inefficient inhibitor injection.

Rensing and Sloan (2008) conducted CFD simulations of hydrate aggregate structure. The aggregation of hydrates particles and fractal structure information is really difficult to acquire experimentally, which is the reason a three dimensional discrete element method (3D-DEM) model

is needed. In their study, detailed solutions to Newton's equations of motion for individual particles were calculated by 3D-DEM model coupled with CFD code. The effect on viscosity also has been calculated by CFD. These simulations were useful to study the effects of attractive forces on relative viscosity. The simulations allowed the researchers to visualize aggregation and the effect of flow on the aggregation.

Sean et al. (2006) investigated the dissociation processes of methane hydrates under water flow conditions by a combination of experimental observations and numerical simulations using CFD. Three-dimensional unsteady CFD code was developed by Jung and Sato (2006). The model adopts collocated finite-volume formulation and moving unstructured grids, which has been successfully applied to predict the behavior of a rising and deforming droplet. The model assumed that ambient fluid was incompressible and no bubble formation occurred in the flow. In this paper, basic transport equations and boundary conditions for CFD method was listed.

Jassim et al. (2008) performed a study to locate a flow restriction induced hydrate deposition in a pipeline using a numerical CFD-based model. The model applied CFD algorithms for configuring the flow field using real gas models and also prediction of the actual fluid properties. The mechanism of the deposition based on the most recent theories of the depositional phenomenon is developed relying on CFD techniques. The study presented the theory in turbulent regime for different hydrate particle sizes thoroughly. Commercial software FLUENT was used to predict the particle velocity profile. In their work, they found out that two mechanisms dependent on the particle size can be applied to explain the particle deposition. They also concluded that the hydrate particles' velocity profile was similar to the carrier fluid velocity profile. However the particles move slower compared to the carrier fluid velocity as the particle size increases.

Balakin et al. (2010) described their experimental study of Freon R11 hydrate transport in turbulent flow through a model-scale pipeline of complex configuration. They assumed that the size

of hydrate particles was uniform and constant; they also assumed that the apparent viscosity of the hydrate slurry follows a dependence gained from experimental measurements of the pressure drop of the pipeline. The Eulerian - Eulerian CFD model was used to model the experimental rig and validated with the tests' results. The model was turbulent, three-dimensional and two-way coupled. CFD simulations supported the experimental study on the dissociation rate of a hydrate ball suspended in a flow cell. Jassim et al. (2008)'s theoretical work on the dynamic process of methane hydrate deposition in a pipeline was also considered in their study.

Fatnes (2010) summarized the work of numerical simulation of the flow and plugging behavior of hydrate particles. The purpose of this study was to investigate the physics of hydrate particle flow in pipelines using commercial CFD code ANSYS CFX and to compare the simulation performance with another study that used STAR-CD. The interpretation of the physics of bed formation was also examined in this study. The numerical code successfully reproduced the hydrate bed formation within the same flow pattern as was observed experimentally. Experimental results from a multiphase flow loop were collected to compare with results from the numerical simulations for both software packages. A Eulerian - Eulerian two-fluid model was built using ANSYS CFX. The apparent viscosity of the hydrate particle suspensions was well studied. To assess the effect of the apparent viscosity and the particle size on the model results, a sensitivity study of the model was performed.

Mele (2010) employed the FLUENT species transport model to simulate the mixing process between MEG and water at low flushing velocities in a jumper configuration. The K-ε turbulent model was chosen to capture the physical details during MEG mixing with the water phase. Inhibitor concentration gradient predictions showed good agreement with experimental measurements. In her work, she concluded that convection constitutes the major mechanism of glycol distribution at extended periods of time; no significant improvements were obtained between

the concentration profiles gained before the incorporation of the correlation for diffusion coefficient and the MEG fraction gradients estimated upon this modification. Empirical trends with an average deviation of approximately ± 10 percent were reproduced. In comparison with the Volume of Fluid (VOF) model, the Species Transport model with the assumption of negligible of diffusion coefficient gave better predictions for the MEG concentration profiles obtained at high superficial velocities. Mele also tested the time step effect on the simulation accuracy. Small time steps can reduce numerical errors on the MEG concentration predictions, at the cost of increasing the computational effort, as well as the frequency and magnitude of oscillations from the response.

CHAPTER 3: EXPERIMENTAL FACILITY AND PROGRAM

The studies performed for this project rely on experimental work. This chapter introduces the TUHFP (Tulsa University Hydrates Formation Project) jumper facility for thermodynamic inhibitor displacement tests and cyclopentane hydrate experiments. The TU jumper facility was designed and constructed in 2008 during a project partially funded by RPSEA (RFP2007DW1603) to assess hydrate plugging risks in low spot configurations. The experimental facilities are located at the University's north campus. Further detailed descriptions of the test setups as well as operational procedures and test matrixes are discussed in this chapter.

3.1 Experimental jumper facility

3.1.1 Jumper facility description

The jumper system was designed to mimic typical spool geometries encountered in the Gulf of Mexico. Dimensions from a field flowline jumper, as well as a wellhead/manifold jumper, were considered in the selection of the geometry. Additionally, the size criterion (diameter vs. length) was taken into account in order to make this project feasible at the University of Tulsa. The test section is open to the atmosphere and consists of a 3-inch diameter polycarbonate pipe with a total length of about 100 feet, as shown in Figure 3-1. The length of riser section situated downstream of the first low spot is approximately twice the distance of the upstream horizontal pipe, whereas the second low spot is followed by a vertical pipe with half the length of the horizontal section. Figure 3-1 shows a schematic of the test facility with the dimensions associated to each individual line. Two thermocouples were installed into the jumper pipe sections to measure temperature in the low spots as shown in Figure 3.1.

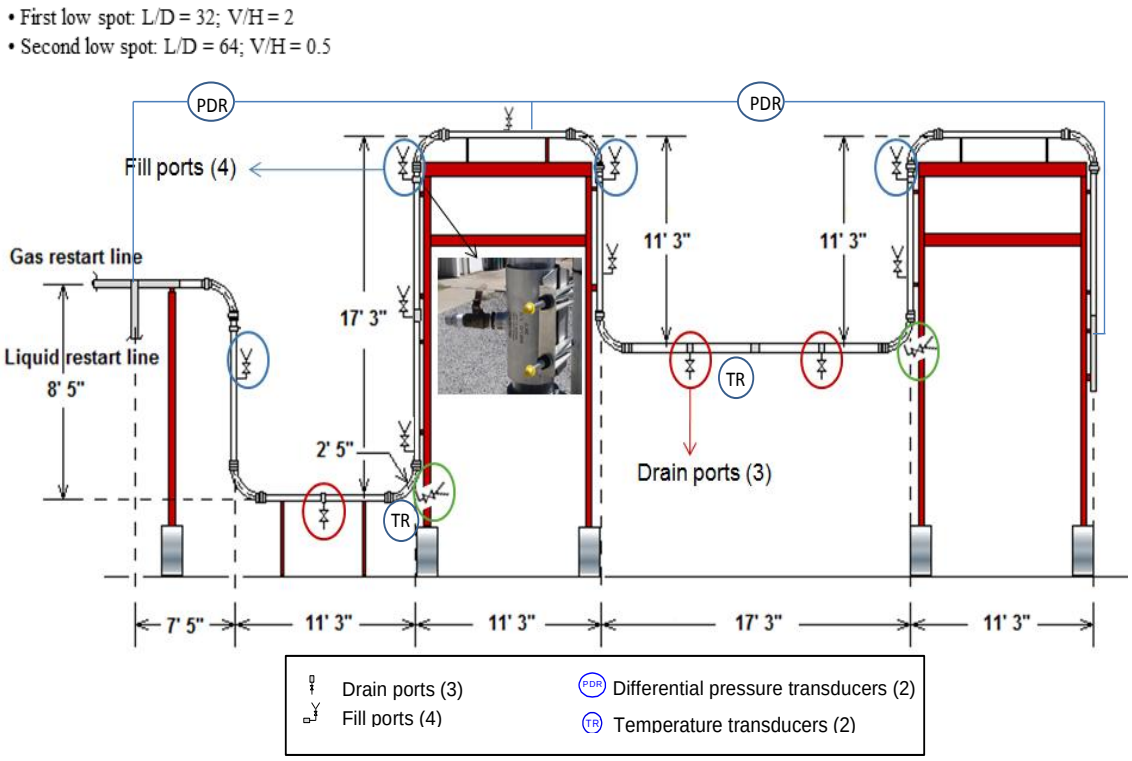

FIGURE 3 - 1: JUMPER TEST SECTION LAYOUT

- Sampling ports

For the purpose of this project thirteen sampling ports were installed along the experimental facility to measure the inhibitor concentration gradient in the jumper system, with a particular emphasis on the low spots sections (horizontal lines and elbows) (see Figure 3-2). The existing polycarbonate sampling ports were replaced with stainless steel clamp saddles to prevent cracking due to temperature change as shown from the picture in Figure 3-1.

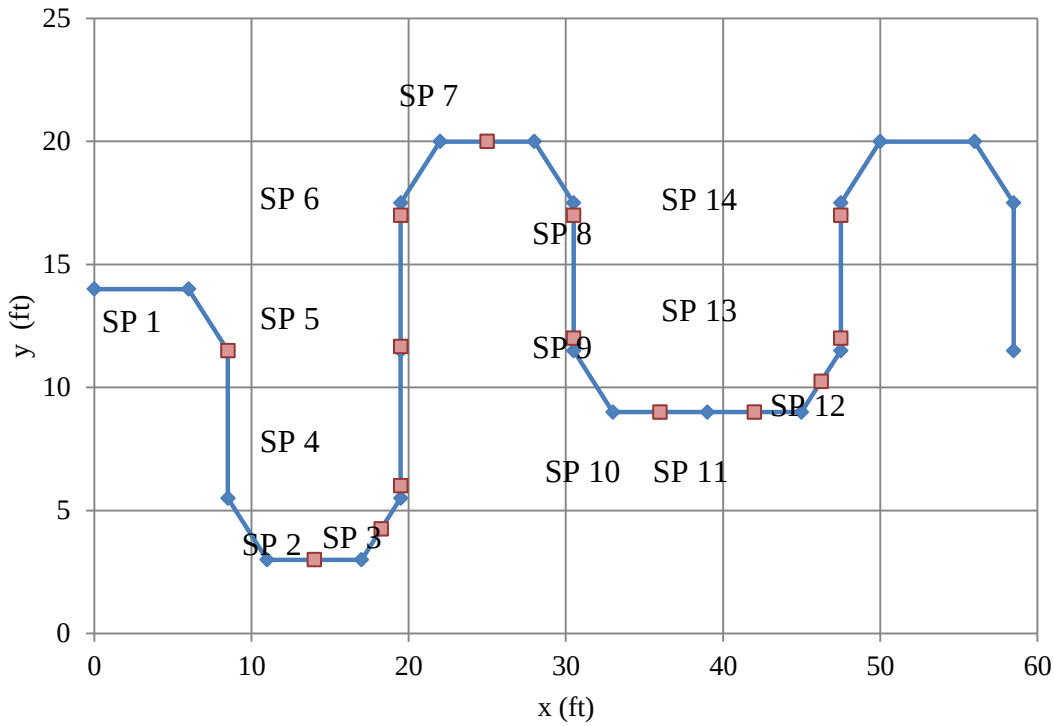

FIGURE 3 - 2: LOCATION OF SAMPLING PORTS ALONG THE JUMPER TEST SECTION

- Liquid Restart System/Air injection

The thermodynamic inhibitor (MEG/methanol) is stored in a 700-gallon supply tank as shown in Figure 3-3. The fluid is circulated through a coriolis flow meter and a bypass line until the desired flow rate is reached. A 1-½ inch three-way valve directs the flow to the test section or returns it to the supply tank. The inhibitor is circulated using a Chemsteel Oberdorfer® gear magnetic drive pump. Performance characteristics of the selected pump are specified in Table 3-1. The circulation lines consist of galvanized steel pipes to prevent corrosion and rusting of the material exposed to the outdoor environment. A 1 ½-inch, Micro Motion flow meter, model CMF100M, was utilized to measure the inhibitor mass flow rate and density during the experimental tests.

Given the high volatility of methanol at the average environmental conditions, a three-phase, 5-HP/1740 RPM Leeson explosion proof motor (Class I, Group D) was coupled to the

aforementioned inhibitor gear pump in order to prevent the hazards associated to the transfer of flammable liquids. A motor frequency drive was also incorporated into the pumping system to provide better control of the inhibitor flow rate and reduce the amount of heat generated.

- Recycling system/Brine supply system

Figure 3-4 shows the tanks used to collect the fluids displaced and flushed from the jumper during the tests as well as to store the brine solution to be used in some tests. The tanks are polyethylene cone bottom tanks, with a capacity of 285 gallons each. All tanks are fitted with a 3-inch ball valve at the bottom outlet, which allows connecting flexible hoses to either drain the collected liquids or to connect to the brine transfer pump. This pump is installed to transfer the brine solution to the test section through a 2-inch stainless steel line. A positive displacement Liquid Controls® meter, model M-15-1, is used to measure the mass and volumetric flow rates of the salt-water mixture during the transfer process to the jumper. The three-way valve installed downstream of the pump discharge enables directing the flow to the jumper inlet or recirculating the liquid through the bypass line.

TABLE 3 - 1: CHARACTERISTICS OF THE INHIBITOR INJECTION PUMP

Parameter	Value	Units
Maximum flow @ 1750 RPM	30	gpm
Theoretical displacement	76.9	cc/revolution
Maximum differential pressure	110	psi
Maximum system pressure	225	psig
Maximum speed	1800	RPM
Maximum fluid temperature	450	F
Minimum fluid temperature	-50	F
NPSHR @ 1750 RPM	10	ft

FIGURE 3 - 3: INHIBITOR INJECTION SYSTEM

FIGURE 3 - 4: COLLECTING TANKS AND BRINE TRANSFER PUMP

- Instrumentation

The facility operates at ambient conditions with two temperature transducers located on each low spot section. The measurements are used to take into account ambient temperature changes into the test analysis and to adjust the temperature in the simulations. Differential pressures are measured for each low spot by two differential pressure transducers. Figure 3-5 shows a picture

of the test section instrumentation. There is also a pressure transducer at the inlet of the jumper test section. All the instruments were connected to a LabView data historian system. Figure 3-6 shows the interface for the jumper LabView interface system in its 2011 version. The data that is monitored and recorded is listed in Table 3-2.

FIGURE 3 - 5: DIFFERENTIAL PRESSURE TRANSMITTERS AND THERMOCOUPLE

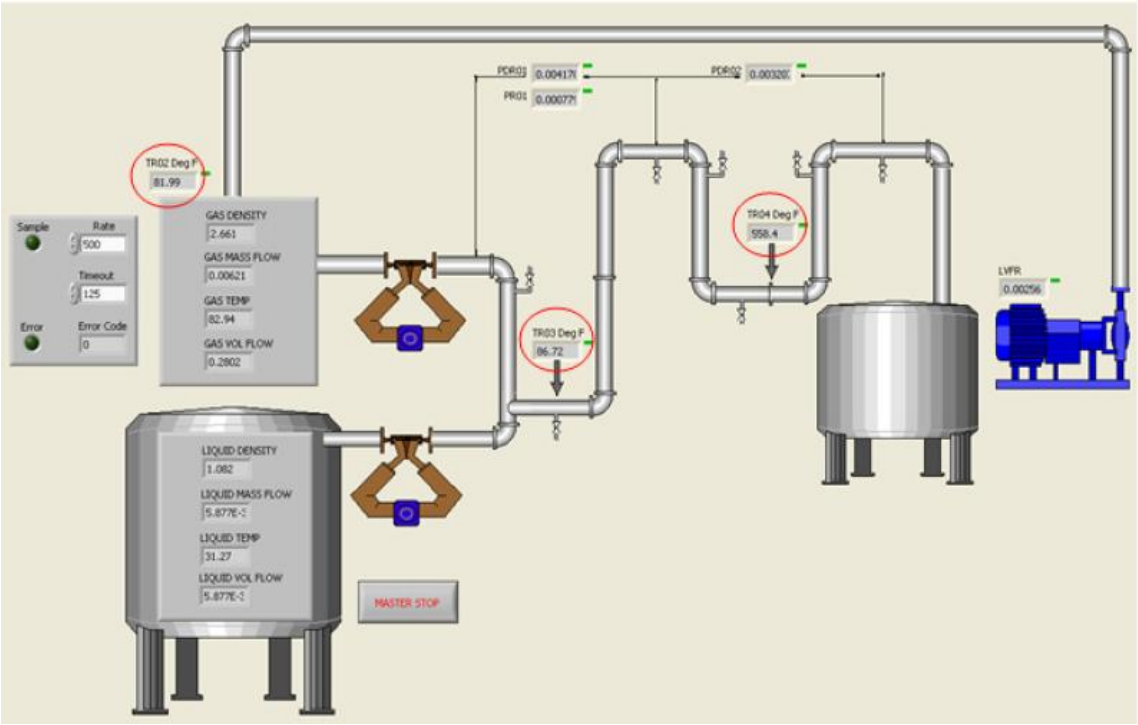

FIGURE 3 - 6: LABVIEW INTERFACE FOR THE JUMPER FACILITY

TABLE 3 - 2: PARAMETERS OF JUMPER LABVIEW HISTORIAN SYSTEM

MicroMotion Liquid (Connected to the storage tank)	
Liquid density	g/cm^3
Liquid mass flow rate	lb/min
Liquid volume flow rate	gpm
Liquid temperature (MicroMotion inside temperature)	$^{\circ}F$
MicroMotion Gas (Connected to the air line)	
Gas density	g/cm^3
Gas mass flow rate	lb/min
Gas volume flow rate	gpm
Gas temperature (MicroMotion inside temperature)	$^{\circ}F$
Temperature ($^{\circ}F$)	
TR02 Liquid temp. @ inlet	
TR03 Liquid temp. @ 1st low spot	
TR04 Liquid temp. @ 2nd low spot	
Differential pressure (psia)	
DPR01 Differential pressure between inlet and 1st high spot	
DPR02 Differential pressure between 1st high spot and 2nd high spot	

- Video Capabilities

Two Sony high resolution digital HD video cameras (model HDR-SR10) were used to record the experiments. All of the videos were converted into MPEG files so that they can be played using a computer's media player. A high speed video camera was also used to record the mixing phenomena at selected locations.

- Experimental apparatus to determine the concentration of inhibitor

A density meter manufactured by Mettler Toledo (model DE40) with an accuracy of ± 0.0001 g/cm^3, is utilized to determine the density of MEG and methanol mixtures in the aqueous samples taken from the jumper system upon each experimental run (Figure 3-7). The measured densities of MEG or methanol solutions can be converted to the corresponding inhibitor concentration in the samples (% wt. or vol.) by means of a regression analysis conducted by the DE40 unit.

FIGURE 3 - 7: METTLER-TOLEDO DE40 DENSITY METER

3.1.2 Special provisions for MeOH tests

Methanol is a colorless liquid, completely miscible with water and organic solvents. It forms explosive mixtures with air and burns with an invisible flame. Safety issues were the biggest concern for the methanol tests. To address these, improvements to the jumper facility were made prior to performing the displacement tests with methanol. Pressure tests were conducted with the jumper pipe section to identify any small leaks. The leaking pipe collars were replaced with new pipe sections and collars. A nitrogen blanketing system was installed to provide an inert environment in the methanol storage tank as shown in Figure 3-8. Industrial liquid nitrogen tanks

(180 liter 22 psi) were connected to the supply tank to provide nitrogen purge flow. A pressure regulator and vent valve were installed to control the tank pressure.

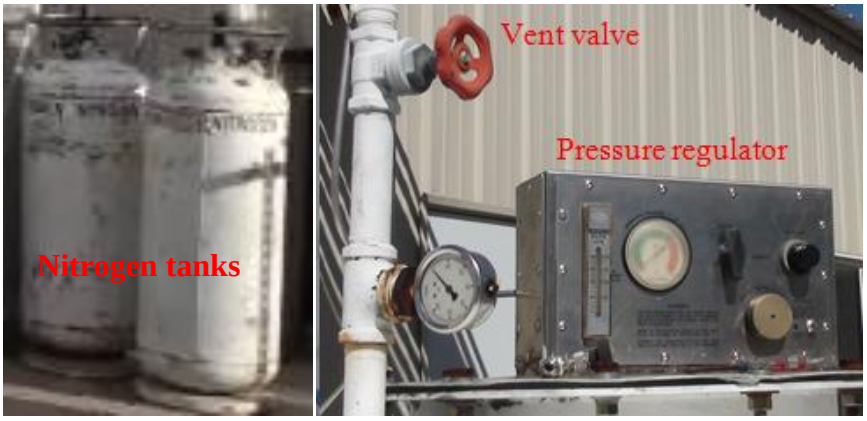

FIGURE 3 - 8: NITROGEN PURGING SYSTEM FOR METHANOL STORAGE TANK

3.2 Experimental program

3.2.1 THI operating procedure

The test procedure used for the displacement tests was implemented by a former student, Susana Mele, for her experimental study. In this thesis, consistent operational protocol was followed for repeated MEG tests. The P&ID of the jumper facility is attached in Appendix B. Some adjustments to the test procedure for the methanol displacement tests were made to meet the safety requirements. Several things listed below needed to be checked and verified before conducting the methanol tests:

1) Ground drums, fire extinguisher on standby
2) Check that the nitrogen purge is set properly
3) Nearby boiler turned off and boiler room doors closed
4) Restrict access to the facility before starting the test
5) Pay attention to all valves being lined up properly before injection methanol
6) Transfer methanol out of the collection tanks after each experiment for proper disposal.

Procedure followed for Water displacement tests

1. Preparation of the inhibitor supply
   a) Align valves of the feed system to the circulation mode
   b) Turn on the chemical injection pump and set the velocity of the drive to 10 gpm
   c) Recirculate the inhibitor in the feed tank for 25 minutes to guarantee homogenization of the mixture
   d) Sample the feed tank through the valve V-3 to verify the initial concentration of inhibitor to be injected
2. Load facility with water
   a) Verify that all the valves of the sampling ports are closed
   b) Start the LabView data historian system
   c) Fill the jumper with water through the inlet port. The total volume of liquid injected depends on the type of experiment to be conducted (full or half jumper volume)
3. Displacement experiment
   a) Set the revolutions of the feed pump to the desired fluid flow rate
   b) Change the alignment of the three-way valve of the feed system (open to the test section) to allow the inhibitor to flow through the jumper and start timer
   c) Video record the displacement phenomena throughout the experiment
   d) Close the three-way valve once the pre-determined volume of inhibitor is injected and stop timer
   e) Turn off the feed pump
4. Sampling Procedure
   a) Samples are collected from the jumper in inverse order (sampling port 13 to 1) to minimize the errors associated to uncontrolled diffusion of inhibitor due to high concentration gradients
   b) Open the sampling valve and introduce a needle coupled to a syringe through the septum installed in the valve fitting

c) Collect 8 cc of sample at each sampling port

d) Close sampling valve and repeat steps (a) - (c) for each sampling port

5. Flushing and drainage of the facility

a) Verify that all the sampling valves are closed

b) Verify that the caps installed on top of the storage tanks are open

c) Turn on the air compressor

d) Open the needle and ball valves located downstream of the compressor to allow the air flow to displace the MEG/Water mixture to the storage tank during 5 minutes

e) Open the purge valves coupled to the sampling ports 2, 10, and 11

f) Collect the displaced liquids through the open sampling ports in buckets

g) Turn off the compressor and close the valves of the air injection system

h) Close the valves installed in the sampling ports 2, 10 and 11

3.2.2 THI displacement experiments

Table 3-3 summarizes the MEG and methanol displacement test conditions. Parameters in the test matrix include different liquid loadings, inhibitor injection rates, water salinity, and amount of MEG or methanol to be added in terms of jumper volumes displaced.

Figure 3-9 illustrates the distribution of the water phase for each of the liquid loadings considered in the experimental test program. Full liquid loading conditions indicate that a volume of water equivalent to almost the total capacity of the jumper system (~ 34 gallons) will be used as the phase to be displaced and inhibited by MEG or methanol. For half liquid loading tests only the first and second low spots of the jumper facility are filled with water; the corresponding volume of the water phase is approximately 17 gallons (half the capacity of the test section).

TABLE 3 - 3: TEST PARAMETERS FOR INHIBITOR DISPLACEMENT TESTS

Parameter	Value
Fluid	Water
Liquid loading	Half full (~ 17 gal), Full (~ 34 gal)
Water salinity	Fresh water, high salinity (12%)
Inhibitor concentration	80% wt
Inhibitor volumetric flow rate (GPM)	1, 5, 10, 20
Inhibitor superficial velocity (ft/s)	0.05, 0.2, 0.5, 0.9
Volumes of jumper displaced	½, 1

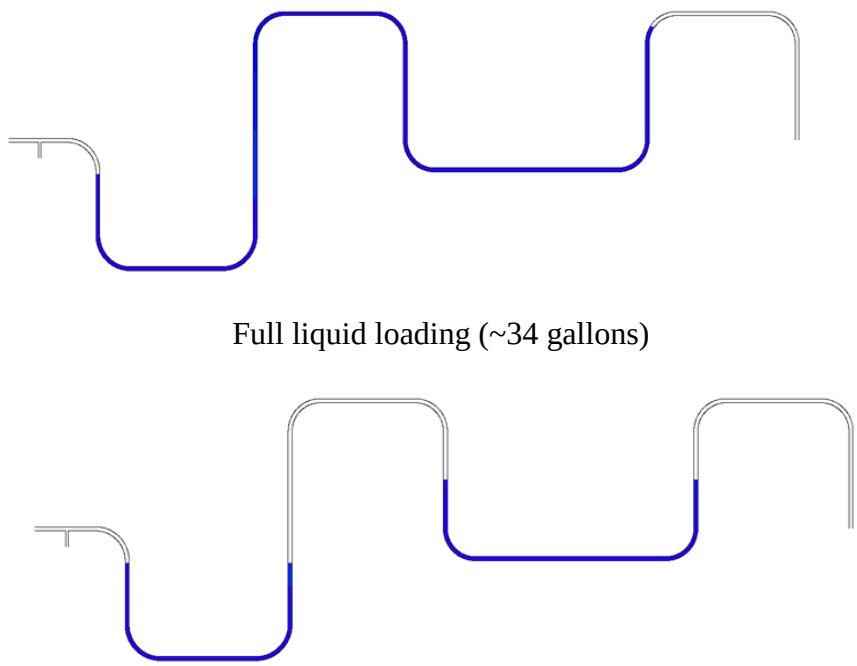

FIGURE 3 - 9: REPRESENTATION OF INITIAL LIQUID LOADINGS

3.2.3 Cyclopentane hydrate experiments

To understand the conditions leading to hydrate plugging in jumper-type configurations and to verify the hypothesis related to higher hydrate risk at certain locations in the jumper facility, hydrate formation experiments were conducted on very cold days in February 2012. Cyclopentane

(c-C_5) was chosen as the hydrate former because of its ability to form hydrates at atmospheric conditions, and tests were conducted by injecting air in the facility to create mixing and simulate the gas restart in actual wells.

- Test matrix

Table 3-4 lists the test conditions. A preliminary experiment with water bridging the first low spot to test the feasibility of forming hydrates in low pressure jumper configurations was conducted by Susana Mele in 2009. Two sets of additional experiments were conducted in 2012 using the same configuration, one with 3.5 percent brine and one with 12 percent MEG. These tests were low superficial velocity tests where less water was removed and inhibited against hydrate. The intent was to determine if restarts could be successfully attempted under these conditions. The third run was conducted in which both low spots were bridged with liquid and cyclopentane using fresh water.

- Test procedure

To perform the experimental runs, the same test procedure was followed as stated below. Figure 3-10 shows a schematic of the initial liquid loading for the four runs. Runs 1 to 3 were conducted with only the first low spot filled, while run 4 had liquid in both low spots initially as shown in Figure 3-10.

1) The first low spot of the jumper was bridged with 4 gallons of fresh water; and afterwards 2 gallons of cyclopentane were loaded into the left leg, on top of the water, to simulate the segregation process of hydrocarbons and aqueous phase accumulated during shut-in operations. Fluids are below the hydrate formation temperature.
2) Subsequently, air at velocities that varied from 1 to 4 ft/s was injected into the system to mix the fluids. Air flow was maintained for 10 minutes after hydrate formation started.

3) After 10 minutes, the system was shut-in for approximately an hour and then a restart was attempted.

4) The air flow rate was resumed and progressively increased to 30 ft/s.

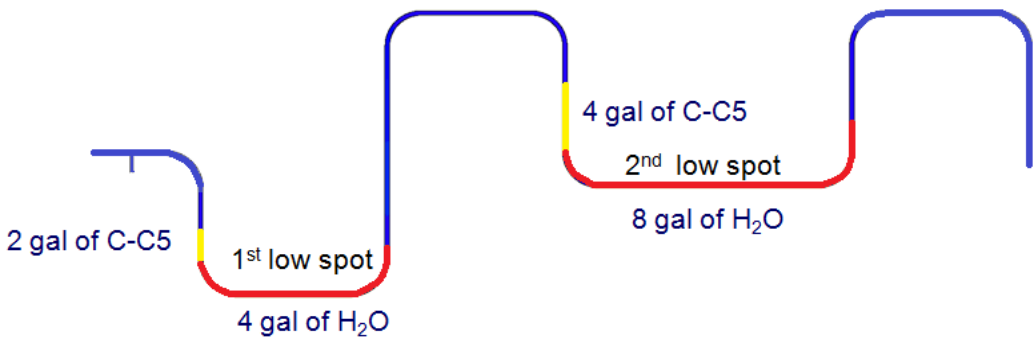

FIGURE 3 - 10: LIQUID LOADING FOR HYDRATES FORMATION TESTS

TABLE 3 - 4: TEST MATRIX FOR CYCLOPENTANE HYDRATE EXPERIMENTS

Run No. (year)	Test Condition	Bridged Low Spot	Ambient Temp. (˚F)	Initial Temp. of Liquid (˚F)	Initial Temp. of c-C5 (˚F)
1 (2009)	Fresh water+ c-C_5	1st	30	~30	~30
2 (2012)	3.5% Brine + c-C_5	1st	18	32	13
3 (2012)	12% MEG+ c-C_5	1st	26	32	25
4 (2012)	Fresh water+ c-C_5	1st 2nd	37	38	20

CHAPTER 4: EXPERIMENTAL RESULTS

In this chapter, the experimental results obtained from the experimental tests performed under the operational conditions specified in Chapter 3 are thoroughly presented. Observations and effect of mixing mechanisms are discussed in detail. For the MEG tests, experimental data obtained in this study as well as prior results by Susana Mele (2010) are presented and compared in this chapter. The methanol injection test results are also summarized. Comparisons between the physical phenomena and mixing mechanisms for MEG and methanol tests have been made. Lastly, observations and conclusions recorded from cyclopentane hydrates experiments in the jumper are discussed.

4.1 MEG displacement tests results

4.1.1 Comparison with Mele's results

Mele (2010) conducted 31 experiments using MEG with fresh water and different liquid loading conditions. In this work, one repeat test for each injection rate was performed after the facility was improved. Moreover, with the help of newly updated Labview system, actual inhibitor injection rates were conducted, so the data quality was improved. The liquid temperature in the system was also monitored. The initial liquid loadings for these tests were 34 and 17 gal of fresh water, which corresponds to a full and half jumper volume. Inhibitor velocities varied from 0.05 ft/s (1 gpm) to 0.9 ft/s (20 gpm) and an equivalent volume of one jumper was injected for each case.

Figures 4-1, 4-2, and 4-3 show the comparisons of dimensionless concentration profiles of MEG with full water loading, 1 jumper volume displaced between this work and Mele's results. The dimensionless concentration is the ratio of the measured inhibitor concentration at a given location to the concentration of inhibitor injected into the jumper (about 80 %wt.). Two repeat tests

were conducted to achieve the injection velocity of 0.05 ft/s. One was at 1.11 gpm and the second repeated test was at 0.74 gpm flow rate. It can be noticed from the plot, the MEG dimensionless concentration profile obtained from Mele's 1 gpm rate test is closer to the results of the test result at the 0.74 gpm injection rate. A similar conclusion was drawn from the repeated test at 0.2 ft/s target flow rate (5 gpm). The MEG dimensionless concentration profile obtained from Mele's 0.45 ft/s flow velocity test is closer to the results from the test result at the 4.84 gpm injection rate. From the high injection velocity repeated test (0.45 ft/s), the same MEG dimensionless concentration profiles were measured as Mele's experimental results. The differences of the results only range from 0 to 0.048 percent. A repeated test wasn't conducted for the 0.91 ft/s target flow velocity test, since a very well inhibited environment (dimensionless concentrations were all close to 1 from the samples taken from all the sampling ports) is obtained from the previous 0.91 ft/s injection velocity tests by Mele (2010).

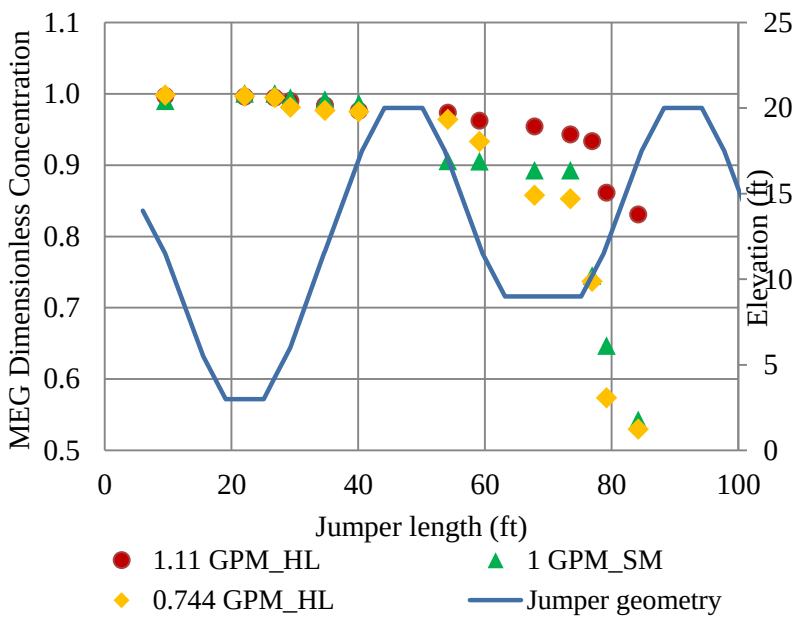

FIGURE 4 - 1: COMPARISONS OF CONCENTRATION PROFILES OF MEG

Comparisons of dimensionless concentration profiles of MEG
(Full water loading - 1 Jumper volume displaced) between this work and Mele's result

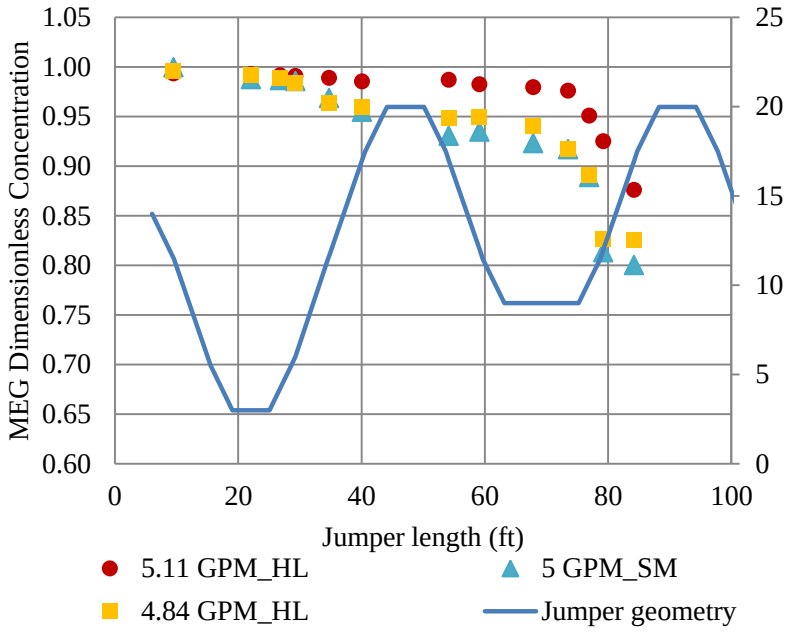

FIGURE 4 - 2: COMPARISONS OF CONCENTRATION PROFILES OF MEG

COMPARISONS OF DIMENSIONLESS CONCENTRATION PROFILES OF MEG
(FULL WATER LOADING - 1 JUMPER VOLUME DISPLACED) BETWEEN THIS WORK AND MELE'S RESULT

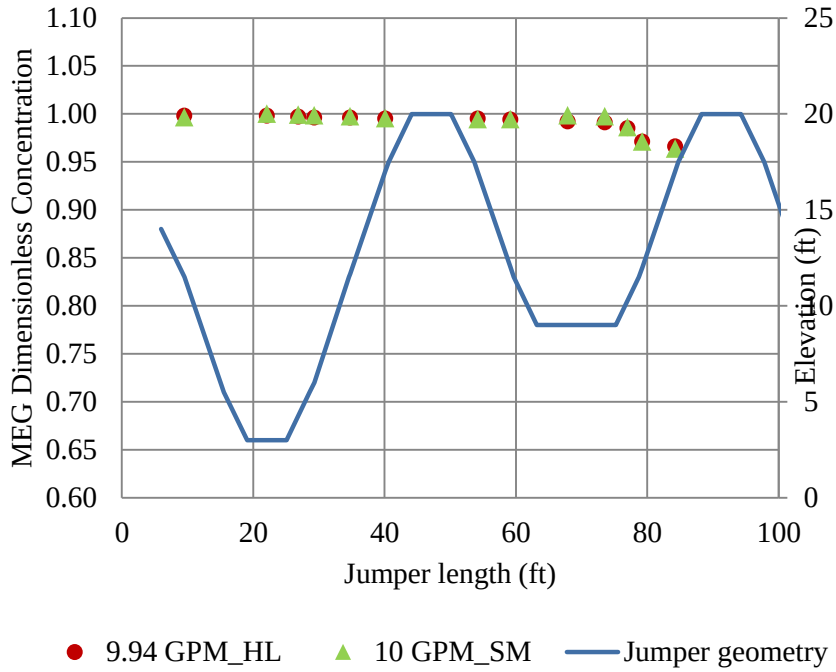

FIGURE 4 - 3: COMPARISONS OF CONCENTRATION PROFILES OF MEG

Comparisons of dimensionless concentration profiles of MEG
(Full water loading - 1 Jumper volume displaced) between this work and Mele's results

4.1.2 Displacement tests with MEG and fresh water

Figure 4-4 shows the MEG concentration profile as a function of the jumper length for all the cases studied. The actual injection rate of MEG was obtained by the averaging the values recorded by the LabView® logging system. At low velocities, a slow diffusion mechanism takes place and a mixing front is observed as MEG is injected into the system. In this case, a concentration gradient was obtained upon analysis of the samples and MEG fractions under 80 percent were measured in the second low spot. Figure 4-4 shows that uniform MEG volume fractions along the system were obtained at high inhibitor velocities (> 0.22 ft/s). Under these flow conditions, the water is displaced as a slug and only the inhibitor remains in the jumper after flushing. Increasing the injection rate above 0.2 ft/s does not improve the inhibition level in the jumper significantly. Designing systems to operate at high velocities will result in increased cost for little benefit.

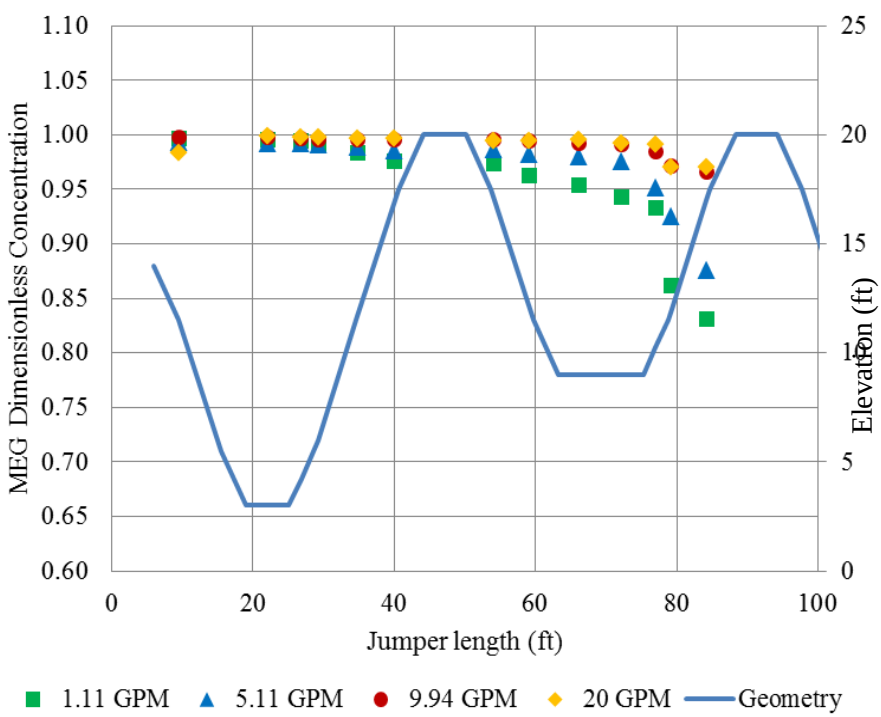

FIGURE 4 - 4: DIMENSIONLESS CONCENTRATION PROFILES OF MEG

Full liquid loading - 1 Jumper volume displaced - Fresh water

Figure 4-5 shows the dimensionless MEG fraction gradients obtained at different injection rates tests conducted by Mele (2010) when approximately 17 gallons (½ jumper volume) of inhibitor were injected. From the plot, similar concentration trends were measured from the tests for all range of glycol injection velocities. In this case, the MEG concentration in the second low spot varies from nearly 30 to 50 percent of the initial volume fraction injected during the jumper flushing procedure, whereas the last riser section remains uninhibited. With regard to the first low spot, the concentration of glycol measured in this section was over 90 percent for all the superficial velocities tested.

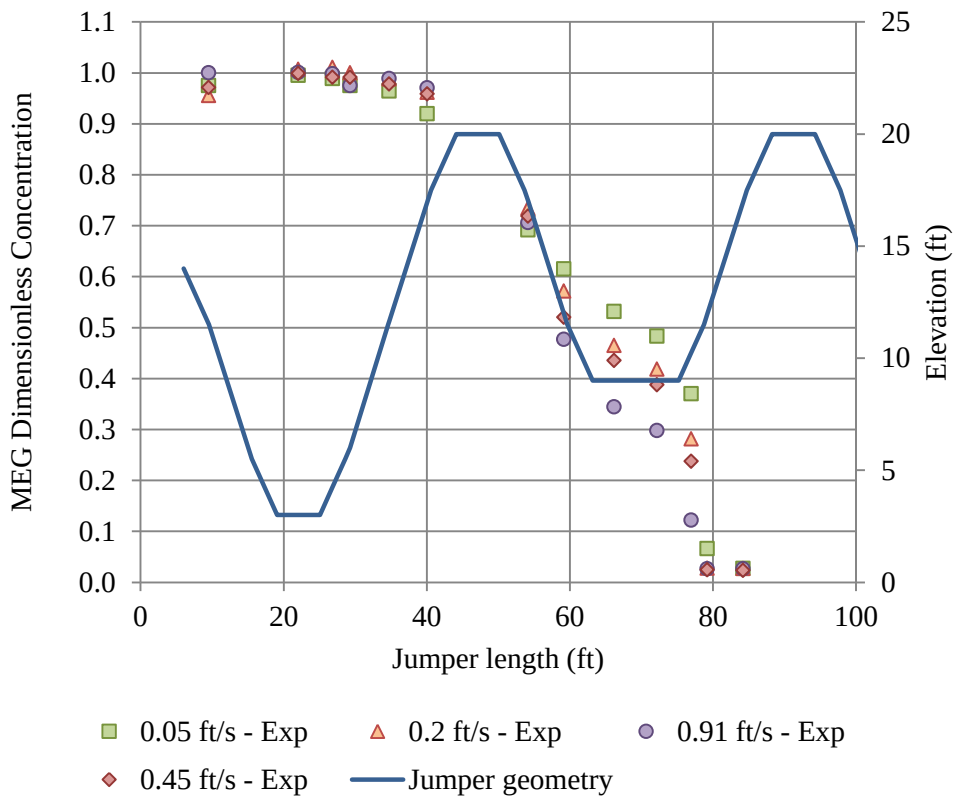

FIGURE 4 - 5: DIMENSIONLESS CONCENTRATION PROFILES OF MEG

Full liquid loading; ½ Jumper volume of MEG displaced; Fresh water from Mele (2010)

Figure 4-6 shows the dimensionless MEG fraction profiles measured from the tests after injecting half jumper volume of inhibitor into a jumper initially loaded with an amount of water equivalent to half the capacity of the system. Results from these tests prove the fact that more water remains in the low spot upon flushing if the initial liquid loading is higher for the same superficial velocity. Low concentrations of less than 10 percent were measured in the second low spot.

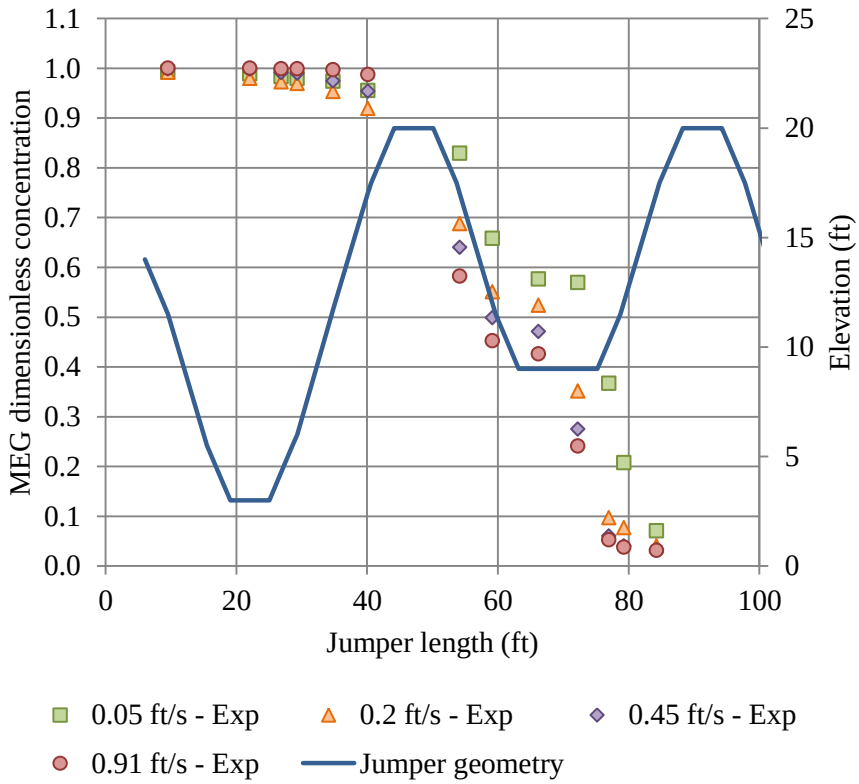

FIGURE 4 - 6: DIMENSIONLESS CONCENTRATION PROFILES OF MEG

Half liquid loading; ½ Jumper volume of MEG displaced; Fresh water from Mele (2010)

4.1.3 Displacement tests with MEG and 12 percent brine

Four experiments were conducted with MEG and 12 percent brine. A full jumper volume was used to displace the contents. As the experimental results show in Figure 4-7, 12 percent brine is more difficult to be displaced out of the jumper compared with fresh water tests. Even higher MEG injection rates resulted in lower MEG concentrations than for fresh water. Density differences

between the displacing and the displaced fluids play an important role on the overall inhibitor dispersion mechanism. As the buoyancy force decreases, gravity-driven convection is reduced and a less efficient spreading process of the glycol solution takes place. Due to relatively small density differences between the MEG solution and the 12 percent brine solution (1,102 and 1,082 kg/m^3, respectively), the transport of species and segregation due to buoyancy forces and gravity are expected to be almost negligible. The dispersion process of MEG into the brine phase is depressed as the contribution associated to gravity-driven convection is reduced. However, even though the final MEG concentration was reduced compared to the fresh water cases, salts also exert an inhibition effect against hydrate formation. In practice the inhibition effect provided by both salt and MEG may be sufficient to prevent hydrate formation. The hydrate stability curve needs to be plotted for each specific inhibited condition to analyze the hydrate formation risk.

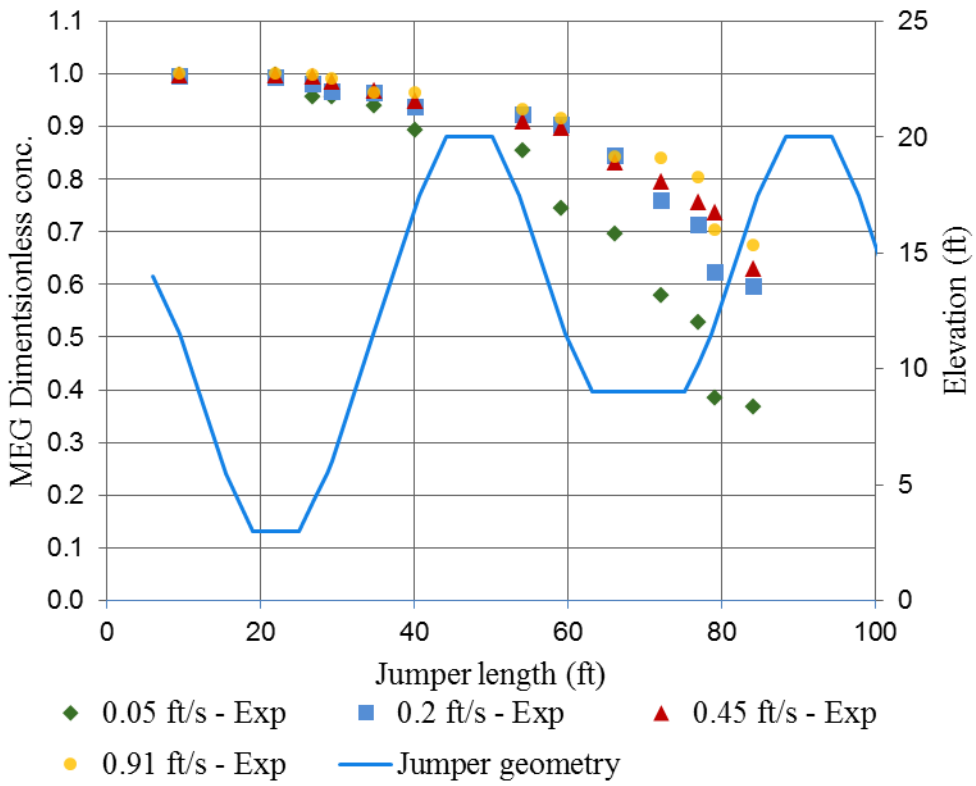

FIGURE 4 - 7: DIMENSIONLESS CONCENTRATION PROFILES OF MEG

Full liquid loading - 1 Jumper volume displaced - 12% wt brine

4.1.4 Visual observations

To better understand the physical phenomena taking place during the displacement tests high speed videos were taken. Figure 4-8 shows the sections where the videos were taken. Videos were taken for different MEG injection flow rates under full and half liquid loading for both fresh water and saline brines.

Observations made from these video clips show that the interface front attains a quasi-sharp shape as the inhibitor is injected into the experimental section, with a remaining thin water layer near the upper wall. This means that the flow behaves like a piston and a significant amount of the aqueous phase is removed from the system. As shown in Figure 4-9 (b) the piston-like mechanism dominates during high velocity displacements. On the other hand, the dispersion process of the THI into the water phase takes place at low injection rates. A longer mixing zone was observed at 0.05 ft/s; however, at elevated superficial velocities the mixing front was sharper while the MEG solution tries to push the water column upward to the next section of the jumper. More mixing of MEG with water was observed in the riser sections at high velocity. When the half liquid loading experiments were run, the local MEG fractions along the axial position were approximately two times greater than those at full liquid loading conditions. Because of the gas presence, some slugging occurred while the fluid moved up the riser and the inhibitor fell directly into the low spot, promoting mixing. Figure 4-9 (a) shows the mixing of MEG and water in the upward vertical section. MEG solution went both upward and downward to disperse into the water phase and gradually mix with water until completely dispersed.

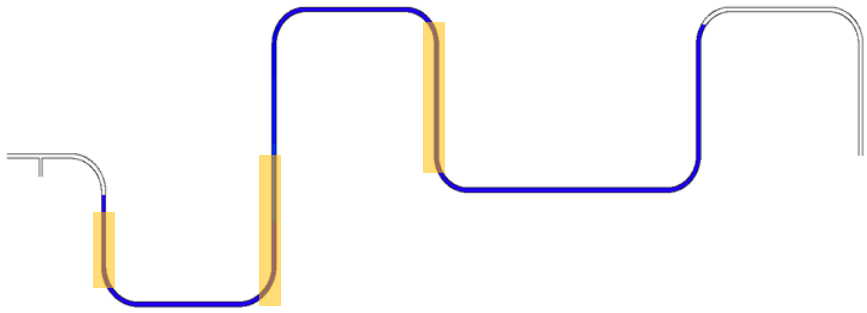

FIGURE 4 - 8: SECTIONS OF JUMPER FOR OBSERVATION STUDY

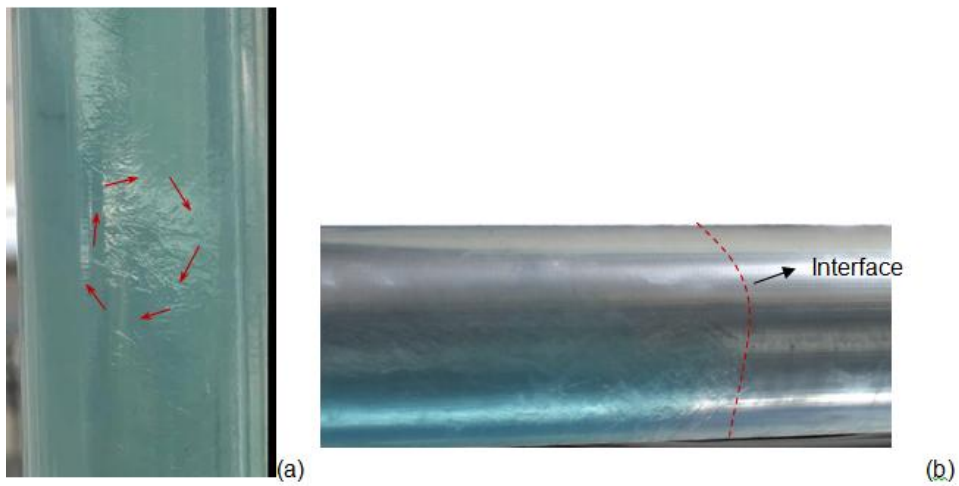

FIGURE 4 - 9: DISPERSION AND DISPLACEMENT

(a) Dispersion between MEG and water
(b) Piston behavior displacement at 0.2 ft/s MEG injection velocity into fresh water

4.2 Methanol displacement tests results

Twelve displacement tests were conducted to investigate mixing and displacement mechanisms using methanol as the THI for displacing water. Experimental parameters include different combinations of inhibitor injection flow rates, liquid loadings and water salinities, as listed in Table 4-1. The following two sections summarize the experimental results and observations from these tests.

4.2.1 Displacement tests with methanol and fresh water

Eight experiments using 80 wt percent methanol with fresh water were conducted. Six experiments were conducted with a full jumper and two with half liquid loading. Inhibitor velocities

varied from 0.05 ft/s (1 gpm) to 0.9 ft/s (20 gpm) and an equivalent volume of one jumper was injected for each case. Samples were taken right after stopping methanol injection to minimize the effect of diffusivity. At both low spots, samples were collected from the top and bottom location inside the pipe sections to examine the expected segregation of two phases.

- Full liquid loading, one jumper volume displacement tests

Table 4-1 gives the actual total volume of injected methanol for each full liquid loading fresh water test calculated from the data recorded using the Labview® logging data. Methanol overriding the water phase and long mixing fronts were observed at both low spots. Figure 4-10 shows the MeOH dimensionless concentration profile as a function of the jumper length for all the cases studied. As it is possible to observe from the plot, methanol concentration above 90 percent can be achieved in the vertical sections at all velocities. The volume percent of water left in the second elbow was decreased from 30 percent to 8 percent while increasing injection velocity from 0.05 to 0.91 ft/s. At low injection velocities (below 0.45 ft/s), the water cuts after displacement at both low spots were higher than 40 percent. The amount of water left in these low spots is higher with methanol than MEG, leaving the former more likely to form hydrates.

TABLE 4 - 1: METHANOL DISPLACEMENT TESTS WITH FRESH WATER - FULL LIQUID LOADING

Test No.	Target flow rate	Actual flow rate	Actual injection velocity	Total injection time	Total MeOH injection volume *
	GPM	GPM	ft/s	min	gal
1	1	1.22	0.046	28.5	34.7
2	5	5.38	0.24	6.4	34.4
3	5	5.32	0.23	6.4	34.2
4	10	10.21	0.46	3.3	33.4
5	20	20.49	0.93	1.9	38.6
6	10	10.21	0.46	3.5	35.9

*Target MeOH injection volume is 34 gallons

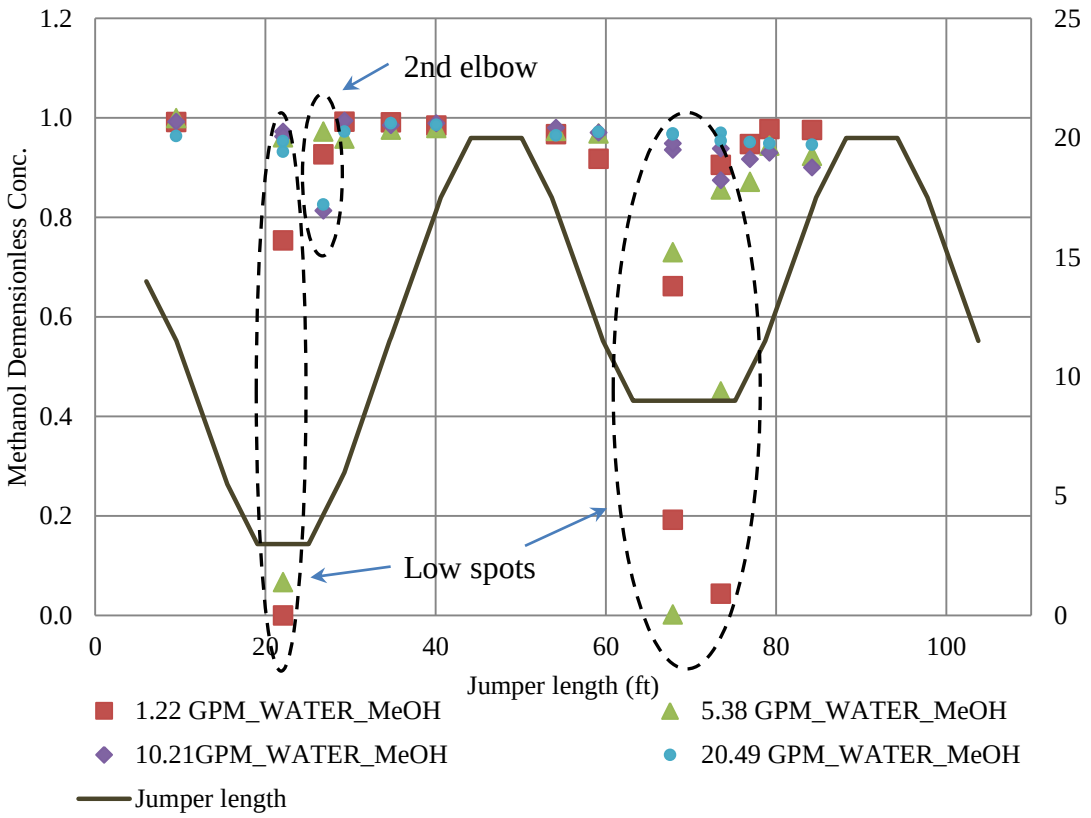

FIGURE 4 - 10: EXPERIMENTAL MEOH CONCENTRATION PROFILES

Experimental MeOH concentration profiles along the jumper length-
(full liquid loading-1 jumper volume displaced-fresh water)

- Half liquid loading, one volume and half volume displacement tests

For half liquid loading cases, Figure 4-11 shows the methanol concentration distributions along the jumper at injection velocity of 0.2 ft/s. It is clear to see that the amount of water left in the jumper was determined by the volume of methanol injected. Injection of a half jumper volume only was not enough to displace most of the water out of the jumper, especially in the second low spots. The same conclusion was drawn from the MEG displacement experiments. Injection of half volume will result in an under inhibited environment.

Methanol over-riding of the water phase was observed for the half liquid loading methanol tests as well. These tests showed a final water cut of around 80 percent in the first low spot and 50

percent in the second low spot. However, injecting more methanol to the jumper didn't improve water removal from horizontal sections of either low spot. Once the stable methanol and water interface was established, additional methanol injection only resulted in pushing methanol out of the jumper. Figure 4-10 shows more methanol remaining in the second low spot with one full jumper volume injected compared to half jumper volume injected. A test of more than one injected jumper volume methanol is suggested to run in the future to see if additional methanol can be dispersed in the second low spot.

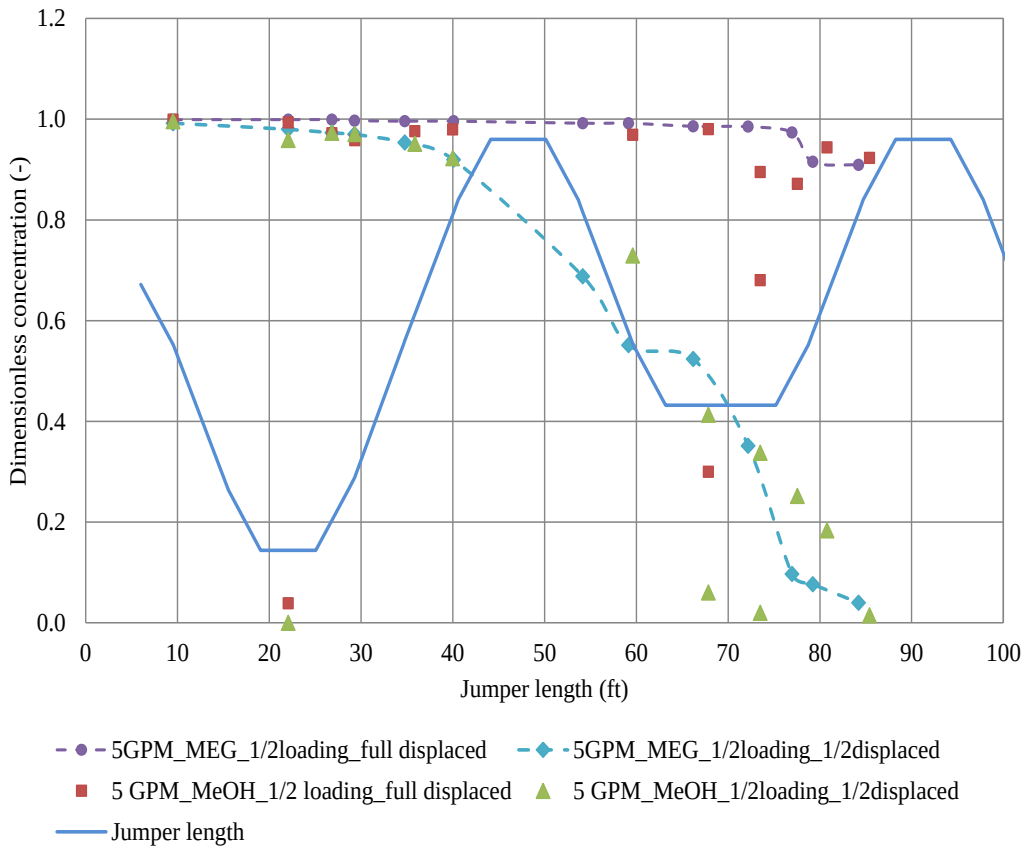

FIGURE 4 - 11: COMPARISON OF MEG AND METHANOL CONCENTRATION PROFILES

Comparison of MEG and methanol concentration profiles-fresh water tests-half loading cases

4.2.2 Displacement tests with methanol and 12 percent brine

Four (4) additional experiments were carried out with methanol and 12 percent brine as the fluid to be contacted and displaced. The operating conditions associated to each of the tests are specified in Table 2-1. A similar test procedure was followed for the methanol and fresh water tests. In this case, density differences between the methanol solution and the brine are relatively large (1102 and 790 kg/m^3, respectively).

Based on the results and trends depicted in Figure 4-12, methanol concentrations above 85 percent can be achieved in the jumper, except for the low spots, after flushing for all cases. The injection velocity did not affect the methanol concentration distribution significantly. In both low spots, the separation between brine phase and methanol solution was observed and also measured for the four different injection rate tests except the 20 gpm case.

Adding salt can increase the diffusivity of methanol since the diffusivity coefficient of salt is much higher than methanol (Herrmann at al., 2004). Compared to the fresh water/methanol displacement tests, a higher methanol concentration was measured for the 12 percent brine left at the low spots and measured methanol concentrations of samples taken from the top of the pipe are above 80 percent for both low spots. Moreover, at the second elbow the concentration differences are negligible for the four brine cases. It is possible to conclude that due to increased buoyancy force, the dispersion process of methanol into the brine initially contained in the system is stimulated as the contribution associated to gravity-driven convection is increased. Considering the fact that salt plays a role as an inhibitor against hydrate formation, the combination of both inhibition effects may overweigh the high level of free water remaining in the low spot.

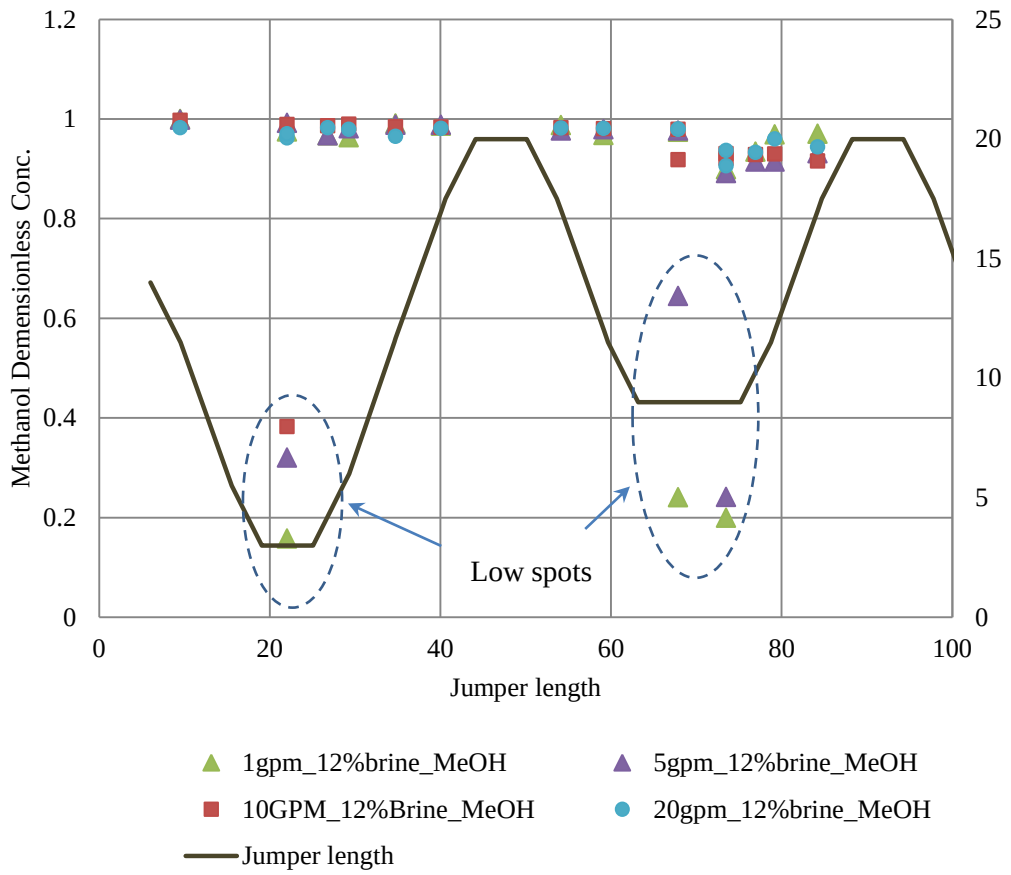

FIGURE 4 - 12: EXPERIMENTAL MEOH CONCENTRATION PROFILES

Experimental MeOH concentration profiles along the jumper length from 12% brine tests

4.2.3 Visual observations

From the methanol jumper displacement tests, a fair amount of the water was displaced from the jumper by the methanol solution. However, a stratified layer of water remained on the bottom of the horizontal low spots. As shown in Figure 4-13 (a), methanol overrides water at the second low spot at 0.2 ft/s injection velocity. The methanol (darker phase) was observed flowing on top of the water during the methanol injection. The water layer did not mix with methanol in an obvious way leaving the water uninhibited. At both low spots the diffusion of methanol into the water was very slow at low injection rates. By increasing the methanol injection rate, more water was removed and less water was observed in both low spots and a more homogenous methanol concentration was measured at different radial locations as shown in Figure 4-13 (b). Even though

small traces of water still remained at the bottom of the horizontal sections, enough methanol was present in the jumper to provide a well inhibited environment from hydrate formation. Figure 4-14 shows the final methanol distribution at the second elbow downstream of the first low spot at a 0.45 ft/s. Methanol flowed through on the top side of the elbow section and barely mixed with the water when the methanol started to reach to the elbow. Over time, more and more methanol built up in the elbow and mixed with the water below the methanol column. The interface of methanol and water was pushed back to the first low spot, and a certain amount of water remained at the end of the injection.

When the methanol displaced the water column in the risers, long mixing fronts were observed and buoyant forces dominated the methanol distribution in the upward flow as the methanol tended to reach the upside of the riser, as shown in Figure 4-15. More effective mixing between methanol and water was observed at both risers of the jumper. Meanwhile, the mixing front of methanol was piston-like in the downcomers. In order to remove most of the water from the jumper, especially the water remaining at low spots, higher methanol injection rates will be required. These findings can help with designing jumper configurations as well as selecting inhibitor injection points and rates.

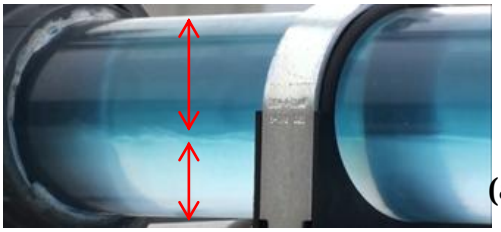

(a)

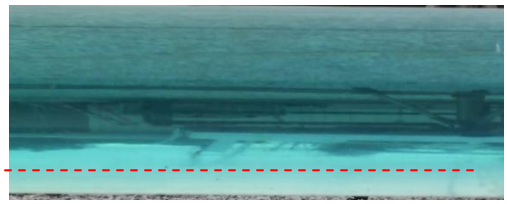

(b)

FIGURE 4 - 13: METHANOL OVERRIDING WATER PHASE

(a) Methanol overriding water phase at 2nd low spot at 0.2 ft/s at injection velocity
(b) Methanol overriding water phase at 1st low spot at 0.45 ft/s injection velocity

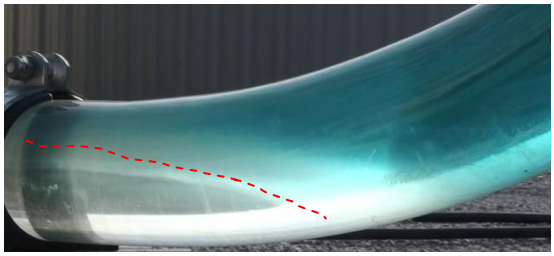

FIGURE 4 - 14: METHANOL DISTRIBUTION

Methanol distribution at 2nd elbow at downstream of the 1st low spot at 0.2 ft/s injection velocity

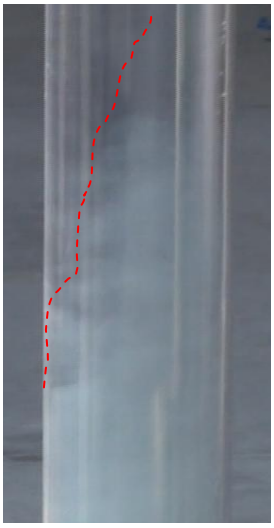

FIGURE 4 - 15: METHANOL MIXING

Methanol mixing front at 1st riser at 0.05 ft/s injection velocity

4.3 Comparison between methanol and MEG tests

The methanol and MEG concentration profiles for the tests that were displace with one jumper volume of fluid are summarized in Table 4-2 and 4-3. A comparison of between the methanol and MEG tests are discussed in the following paragraphs.

Density difference was considered as the main factor to cause different mixing mechanisms and flow behavior for the methanol and MEG tests. The methanol injection flow rate did not affect the inhibitor concentration in the vertical sections significantly. However, water cut levels in the low spots were fairly high and these conditions could pose hydrate plugging risks under certain

circumstances. For the high salinity (12 percent) methanol tests more mixing was measured for all injection rates and the methanol displaced more water from the low spots compared to the results from the fresh water tests. Long mixing fronts were also observed for the methanol tests. The MEG tests showed that the glycol concentration profile depends on the MEG injection velocity, that is, higher injection velocity (>0.45 ft/s) yields higher (90 percent) MEG concentration distribution along the jumper. A piston-like displacement mechanism was also observed in the MEG tests.

Based on the extensive experimental data collected for the methanol and MEG tests as the thermodynamic inhibitor displacing water in the jumper configuration to avoid hydrates formation, comparisons between methanol and MEG tests were made for the following. The experimental data from MEG and methanol for full fresh water loading, one jumper volume displacement tests are presented in Appendix A. The experimental data from MEG and methanol for full 12 percent brine loading, one jumper volume displacement tests are presented in Appendix B.

- Fresh water – Full liquid loading – One jumper volume displaced

Methanol concentrations above 90 percent were achieved in the vertical sections at all injection rates. The volume percent of water left in the second elbow was decreased from 30 percent to 8 percent by increasing injection velocity from 0.05 to 0.91 ft/s. Methanol overriding the water phase was observed in both low spots. At low injection velocity (<0.2 ft/s) the water cuts after displacement at both low spots were higher than 40 percent. Under the wrong conditions there could be hydrate forming risks at those locations. A long mixing zone was also observed.

For the MEG tests, the MEG injection rate significantly affects the glycol concentration profile after the first high spot. Velocities above 0.5 ft/s yielded a more uniform profile. Glycol mixed with water more evenly in the radial direction. Most water was displaced out of the low spot with every MEG injection rates. Potential hydrate formation risk is minimal at the first low spot. Generally, a piston-like mixing front was observed.

- Fresh water – Half liquid loading – One jumper volume displaced

For the methanol tests injection of a half jumper volume of methanol was not enough to displace most of the water at 0.2 ft/s. Methanol overriding water was observed and 90 percent water cut was measured in the first low spot after injection for both full and half injection volumes. More attention is needed for the low spots to minimize hydrate formation risks.

Similar results were obtained for the MEG displacement tests. The injection of one jumper volume of MEG displaced more than 90 percent of water from the low spots and left those sections well inhibited, but the second part of the jumper was at risk when only half volume was injected.

- 12 percent brine – Full liquid loading – One volume displaced

For the methanol with brine tests, more mixing was obtained for the 12 percent brine case in the low spots, and the injection velocity did not significantly affect methanol concentrations' distribution. Methanol concentration reached above 90 percent at the second elbow for all injection rates used. The risk of hydrate plugging was low at this location.

The mixing process between the MEG and the 12 percent salinity brine was found to increase with the flow velocity increase. Density differences between the displacing and the displaced fluids play an important role on the overall inhibitor dispersion mechanism. A less efficient spreading process of the glycol solution in 12 percent brine was measured.

TABLE 4 - 2: METHANOL AND MEG RADIAL CONCENTRATION PROFILE AT THE 1ST LOW SPOT FRESH WATER (FULL LIQUID LOAD – ONE JUMPER VOLUME DISPLACED)

1st low spot	Dimensionless Conc. of MeOH			Dimensionless Conc. of MEG		
Injection velocity (ft/s)	Top	Bottom	Average	Top	Bottom	Average
0.05	0.75	0.00	0.21	0.94	0.78	0.86
0.20	0.96	0.07	0.74	0.94	0.86	0.90
0.45	0.97	0.96	0.96	0.94	0.93	0.94
0.91	0.95	0.93	0.92	0.94	0.94	0.94

TABLE 4 - 3: METHANOL AND MEG RADIAL CONCENTRATION PROFILE AT THE 2ND LOW SPOT (FRESH WATER – FULL LIQUID LOAD – ONE JUMPER VOLUME DISPLACED)

2nd low spot	Dimensionless Conc. of MeOH			Dimensionless Conc. of MEG		
Injection velocity (ft/s)	Top	Bottom	Average	Top	Bottom	Average
0.05	0.66	0.19	0.43	0.91	0.91	0.91
0.20	0.73	0.02	0.71	0.92	0.92	0.92
0.45	0.95	0.94	0.93	0.93	0.92	0.93
0.91	0.97	0.97	0.95	0.94	0.94	0.94

4.4 Cyclopentane hydrates experiments

Previous studies with a subsea jumper configuration showed that liquid accumulation zones represent the critical locations in jumper configurations where the risk of hydrate formation increases significantly (Coletta, 2009). Figure 4-16 illustrates the sections of the experimental facility that exhibited the largest liquid holdups upon restart with gas. In order to understand the conditions leading to hydrate plugging in jumper geometries, as well as to validate the hypothesis on unsafe locations in this type of configuration, hydrate formation feasibility tests were conducted in the low pressure facility. Cyclopentane was used as a hydrate former due to its ability to form hydrates at atmospheric pressure. Figure 4-17 shows the cyclopentane hydrate equilibrium curves for fresh water, 3.5 percent brine, and 12 percent MEG solution. This study began by demonstrating the feasibility of generating hydrates in a clear jumper at atmospheric conditions with fresh water. Studies with brine and MEG were conducted to determine whether the presence of inhibitor present in the system would change the hydrate formation behavior in this type of configuration.

A preliminary experiment with water bridging the first low spot to test the feasibility of forming hydrates in the low pressure jumper was conducted by Susana Mele in 2009. Two sets of additional experiments were conducted in 2012 using the same configuration. These tests were low

superficial velocity tests in which less water was removed and inhibited against hydrate. The intent was to determine if hydrate plugs would form under these conditions. The third run was conducted with both low spots bridged with liquid and cyclopentane. Table 4-4 shows the test matrix for the cyclopentane hydrate formation tests.

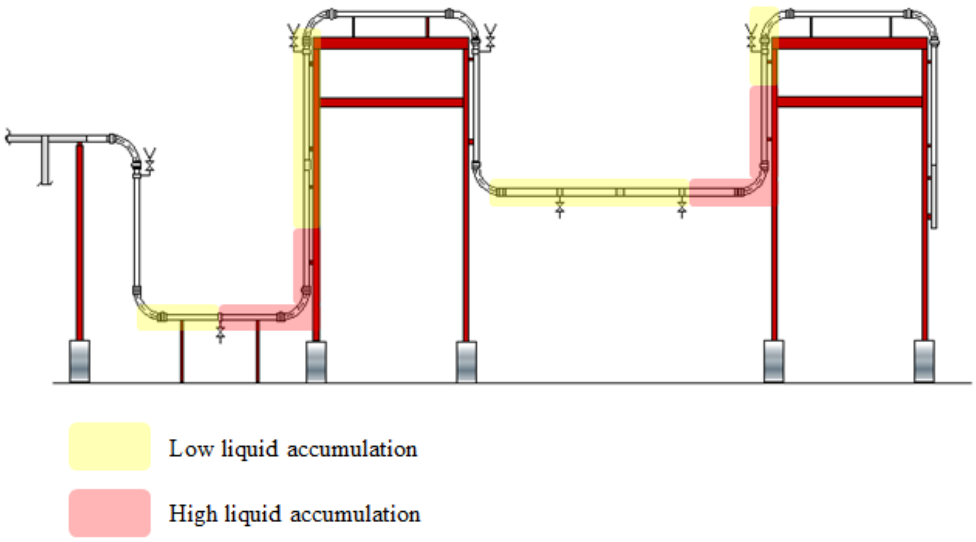

FIGURE 4 - 16: LIQUID ACCUMULATION ZONES DURING GAS RESTART (COLETTA, 2009)

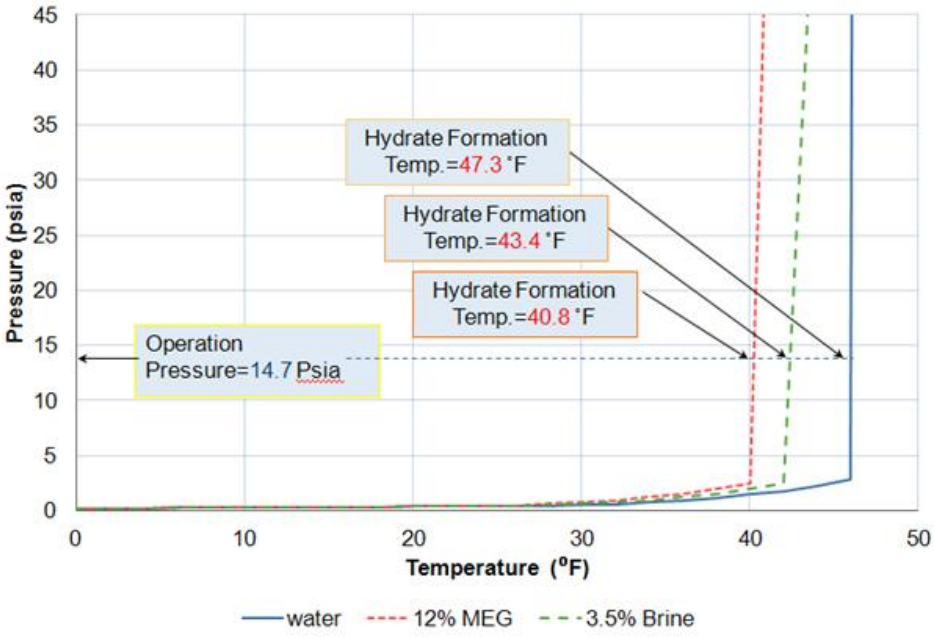

FIGURE 4 - 17: CYCLOPENTANE HYDRATE EQUILIBRIUM CURVES

TABLE 4-4: TEST MATRIX FOR CYCLOPENTANE HYDRATE EXPERIMENTS

Run No. (year)	Test Condition	Bridged Low Spot	Ambient Temp. (˚F)	Initial Temp. of Liquid (˚F)	Initial Temp. of c-C5 (˚F)
1 (2009)	Fresh water+ c-C_5	1st	30	~30	~30
2 (2012)	3.5% Brine + c-C_5	1st	18	32	13
3 (2012)	12% MEG+ c-C_5	1st	26	32	25
4 (2012)	Fresh water+ c-C_5	1st 2nd	37	38	20

4.4.1 Run No.1: Fresh water and cyclopentane

In January 2009, a preliminary experiment to test the feasibility of forming hydrates in the low pressure jumper was conducted (Mele, 2010). Cyclopentane was chosen as the hydrate former because of its ability to form hydrates at atmospheric conditions. The first low spot of the jumper was bridged with four gallons of fresh water, and afterwards two gallons of cyclopentane were loaded into the left leg, on top of the water. Air at velocities that varied from 1 to 4 ft/s was injected into the system to mix the fluids. Little liquid carryover was observed during this operation. Approximately ten minutes was required to form the hydrates. The development of a permeable hydrate plug was observed in the lower elbow while the walls of the 14-foot long vertical pipe were coated with hydrate crystals. The system was then shut in for about an hour and then a restart was attempted. The plug was still permeable to gas at flow rates up to 4 ft/s. The air flow rate was then increased to 30 ft/s without experiencing any rise in the operating pressure. At this superficial velocity the hydrate plug was eventually displaced and hydrate chunks were carried over to the second low spot. Figure 4-18 illustrates the test procedure used for this experiment. The same procedure applies to run Nos. 2 and 3 as well.

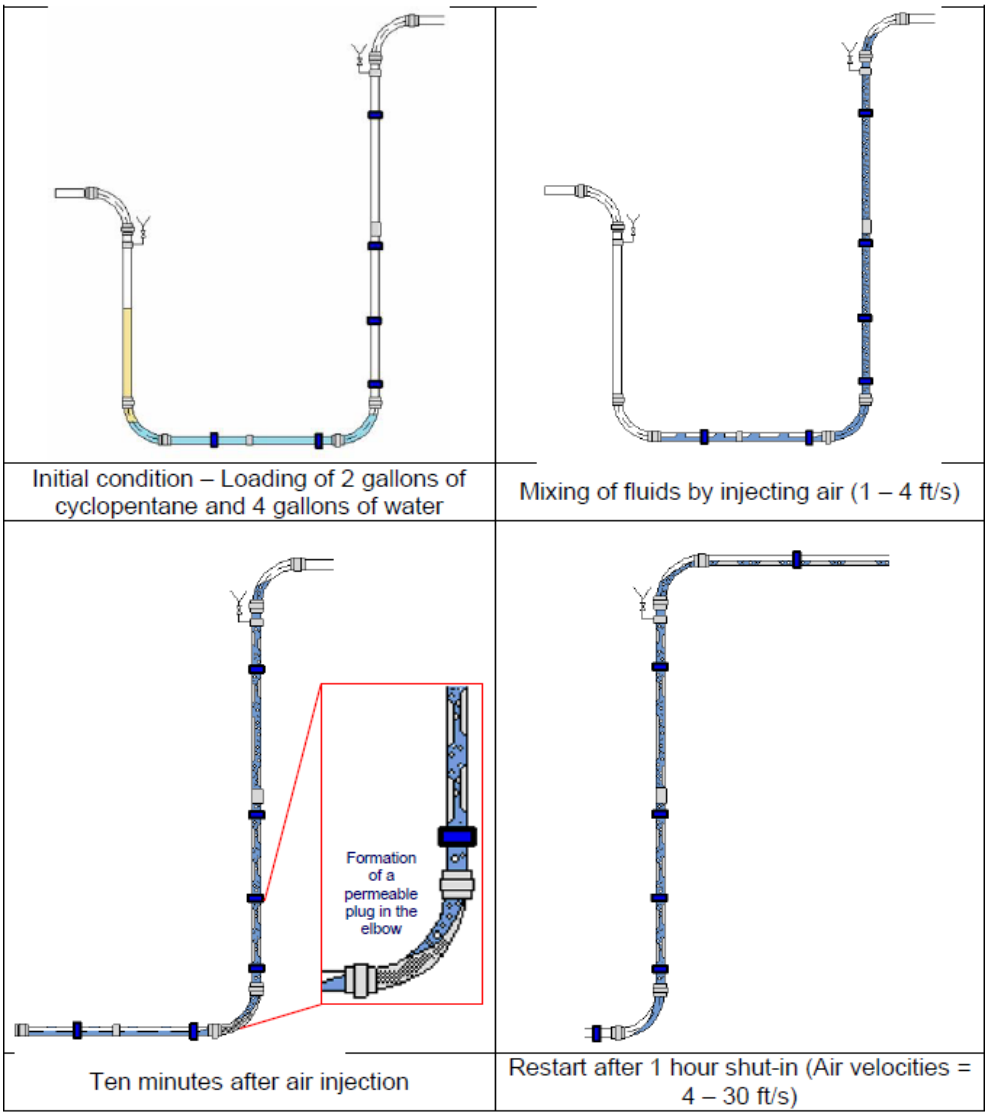

FIGURE 4 - 18: TEST PROCEDURE AND JUMPER OBSERVATIONS

Test procedure and observations for hydrate formation experiments in the jumper (Mele, 2010)

4.4.2 Run No.2: 3.5 percent Brine and cyclopentane

For this test, four gallons of 3.5 percent brine was first poured into the first low spot, and then 2 gallons of cyclopentane were poured on top of the brine phase. Ambient temperature during this test was 18 °F; the initial temperature of the brine was 32°F and the initial temperature of cyclopentane was 13°F. The temperature of the injected air flow and temperature of liquid in the first low spot were recorded by LabView. Figure 4-19 demonstrates the temperature change during the test.

Hydrates formed in less than five minutes. The sub-cooling was about 15°F. Ice was observed accumulating on the pipe wall while charging the liquid, and ice chips were present in the liquid in the first low spot. Ice is known to be a nucleating agent and may have helped hydrates form. During the first air flow period a permeable hydrate plug formed in the second elbow and part of the first low spot. When hydrates started to form, they evenly coated the wall in the first riser and remained attached to the wall during the test. Upon restart at higher velocity some of the hydrates were displaced: some of them deposited at the first high spot and some carried over to the second low spot. Eventually high velocity air passed through the pipe without displacing any more hydrates. MEG was used to dissociate the hydrates after the experiment was complete. Only part of the hydrate mass was dissociated when a 75 percent MEG solution was flushed through the jumper. When the MEG solution was displaced with a high rate of air most of the hydrates remaining were carried to the MEG storage tank.

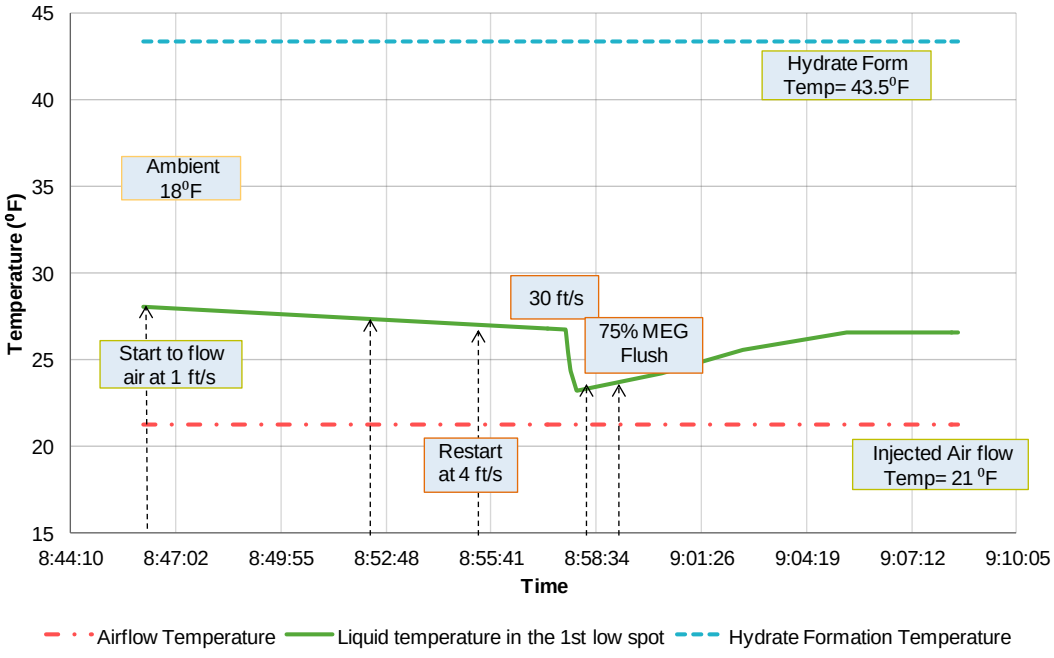

FIGURE 4 - 19: TEMPERATURE TRACE FOR RUN NO.2

Temperature trace for run No.2: 3.5% Brine +cyclopentane

4.4.3 Run No.3: 12 percent MEG and cyclopentane

Four gallons of 12 percent MEG solution were first poured into the first low spot; then two gallons of cyclopentane were poured on top of the MEG phase. The ambient temperature was 26°F; the initial temperature of the brine was 32°F and the initial temperature of cyclopentane was 25 °F. The sub cooling during the injection was between 8 and 10°F as shown in Figure 4-20.

Hydrates formed in the 12 percent MEG environment under the experimental conditions noted above. The hydrates that formed were slushy in nature rather than the typical gas permeable plug that was formed in the other two tests with brine and fresh water. When the hydrates started to form, a fairly evenly coated wall was observed at the first riser. As the test progressed, some hydrates above began to melt, possibly caused by the increasing temperature inside the pipe. After the test, almost all of the hydrates were dissociated when the 75 percent MEG solution was used to flush the jumper.

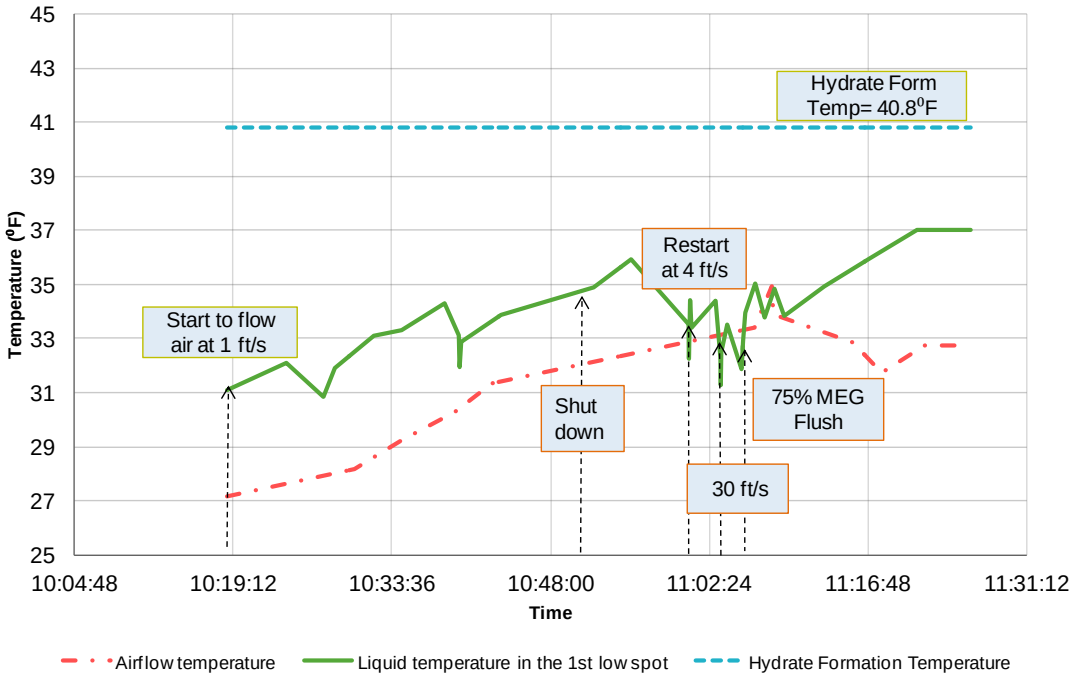

FIGURE 4 - 20: TEMPERATURE TRACE FOR RUN NO.3

Temperature trace for run No.3: 12% MEG + cyclopentane

4.4.4 Run No.4: Fresh water and cyclopentane in both low spots

Figure 4-21 shows the liquid loading locations for Run No. 4. Four gallons of water were first poured into the first low spot, and then two gallons of cyclopentane were poured on top of the water phase from the inlet. Meanwhile, eight gallons of water was poured into the second low spot, followed by four gallons of cyclopentane. The ambient temperature was 26°F, the initial temperature of the brine was 32°F and the initial temperature of cyclopentane was 25°F. The temperature of the injected air flow and temperature of the liquid in first low spot was shown in Figure 4-21. The sub-cooling for this test was about 8 to 10°F.

After hydrates nucleated at the cyclopentane-water interface, they grew rapidly, formed a hydrate slurry, and eventually accumulated to form a permeable plug. The second elbow and first low spot were plugged by hydrates. The first riser was coated with a hydrate layer. During shut in, hydrates started to melt because of the increasing ambient temperature. A significant mass of hydrates was observed in the second low spot, but no hydrate plug seemed to form in the second low spot. The hydrate phase was observed floating on top of the water and small hydrate particles kept falling off the hydrate bed. Upon restart these floating chunks were easily carried out by air flow. Some hydrates from the first low spot were transported to the first high spot and second low spot, and accumulated during restart. Potential plugging risk at the second elbow was significant because no inhibitor reached this location. This test demonstrated that hydrates that form upstream in a jumper may be carried towards downstream equipment and jam as velocities are increased during the restart process.

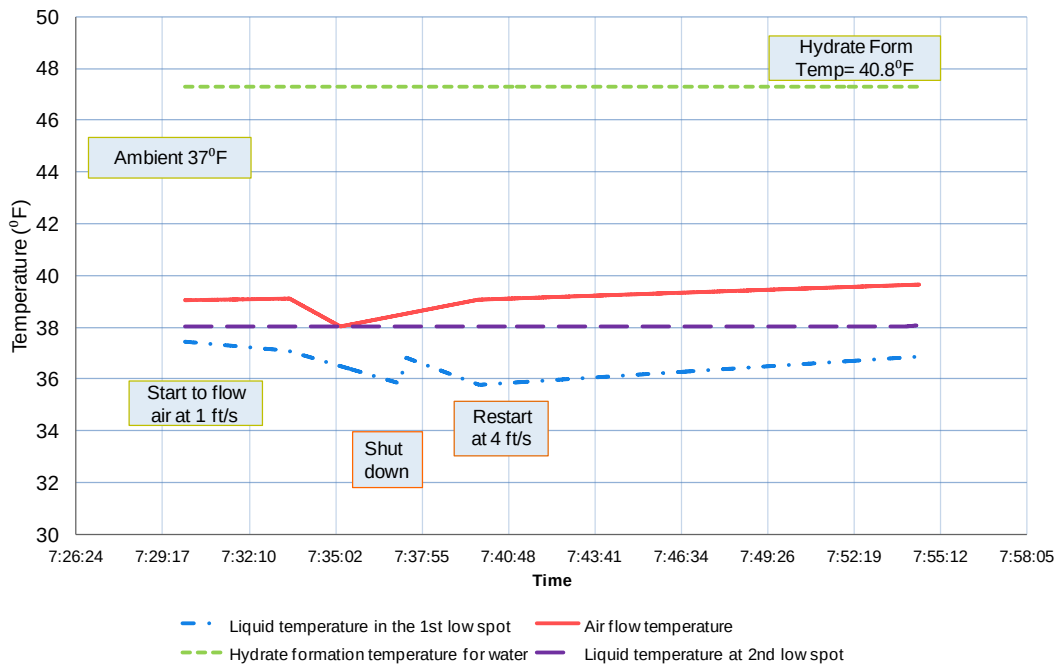

FIGURE 4 - 21: TEMPERATURE TRACE FOR RUN NO.4

Temperature trace for run No.4 with both low spots

CHAPTER 5: SIMULATION RESULTS

OLGA one dimensional (1D) transient simulations were conducted to evaluate the software's capacity to predict the thermodynamic inhibitor injection by using the Inhibitor Tracking Module. In addition, assessments were conducted with regard to the modeling assumptions and considerations that are required to reproduce with reasonable discrepancies the experimental distribution of THI along the jumper system. Secondly, simulation results from the commercial software FLUENT® will be analyzed and compared with experimental data to appraise the capabilities of a two dimensional (2D) CFD model to estimate the displacement and dispersion mechanisms that take place during jumper bull-heading operations with glycol acting as a hydrate inhibitor. Thirdly, three dimensional (3D) simulation results performed by CD-Adapco using STAR-CCM+® CFD code will be presented in this chapter. Lastly, comparisons among 1D, 2D and 3D simulation results are made.

5.1 OLGA simulations

One dimensional transient model simulations were performed using the commercial software package OLGA® 7 to assess the capabilities of a 1D transient model to estimate the displacement and dispersion mechanisms that take place during jumper flushing operations with methanol and MEG as thermodynamic inhibitors. The "Inhibitor Tracking Module" was employed for this study.

5.1.1 OLGA inhibitor tracking module

The OLGA Inhibitor Tracking Module is often utilized in flow assurance studies to ensure that the amount of hydrate inhibitor injected throughout the pipelines is sufficient to prevent the formation of hydrates. In the standard three-phase OLGA model, the pipeline may contain water

and inhibitor, but information regarding the inhibitor concentration along the line is not available. In order to estimate inhibitor concentrations along the flowline, the Inhibitor Tracking Option must be employed through the COMPOSITIONAL keyword and cannot be used in combination with the other modules available through this keyword (e.g., Black oil or Compositional Tracking). The following assumptions are made for inhibitor tracking:

- The only properties of the aqueous phase affected by the inhibitor are the viscosity, density and the density's derivatives.
- The water vapor content in the gas phase is adjusted by the mole fraction of inhibitor in the aqueous phase.
- The mole fraction of inhibitor in the gas phase is equal to the vapor pressure divided by the system pressure.
- There is no diffusion of MEG in the aqueous phase.
- The inhibitors do not affect flashing between gas and oil. This flash is calculated based upon the gas mass fraction from the PVT table.
- There is no hydrocarbon component dissolved in the water.
- The Inhibitor Tracking Module must be used with either a two-phase fluid table or three-phase fluid table that has only H_2O in the water phase (i.e., a pure water phase without inhibitors or contaminants).
- Active coefficients from UNIFAC correlations are used to calculate the chemical potentials of inhibitor and water in the aqueous phase.

At each time step the properties of the aqueous phase are calculated from the local pressure and temperature, and also from the fluid composition in each section of the pipeline. The effects of the inhibitor are included in the calculation of the density and viscosity of the aqueous phase. The method of Grunberg and Nissan is used to calculate the viscosity of the inhibitor-water mixture, and

the Hankinson-Brobst-Thomson (HBT) technique yields an estimate of the liquid density. The effect of inhibitor is also included in the calculation of the hydrate formation temperature. The user can either specify a hydrate curve for each inhibitor concentration and let OLGA interpolate between the values, or the Hammerschmidt formula for hydrate depression can be used (The equation is valid for inhibitor concentrations between 0 and 70 percent.):

$$T_{MEGCONC} = T_{MEGCONC=O} - \Delta T \qquad (5.\ 1)$$

$$\Delta T = \frac{H * W}{100 * M - M * W} \qquad (5.\ 2)$$

ΔT = Hydrate depression, ^{o}F

M = Molecular weight of inhibitor (MEG: 62.069 g/mol, MEOH: 32.042 g/mol)

H = Hammerschmidt constant, default value is 2335 delta F

W = Weight per cent of the inhibitor in the liquid

$T_{MEGCONC}$ = Calculated hydrate temperature with inhibitor

$T_{MEGCONC=0}$ = Hydrate temperature without inhibitor

For the other properties of the aqueous phase, the effects of the inhibitor are neglected and pure water properties from the three-phase fluid table or from OLGA are adopted. (OLGA User's manual, 2008)

5.1.2 OLGA simulation setup

With the Inhibitor tracking module, one can specify a hydrate inhibitor (MEG, methanol, or ethanol) to see the effect this will have on the formation of hydrates in the pipeline. The following keyword must be specified to use the inhibitor tracking option:

- OPTIONS to set COMPOSITIONAL = MEG/MEOH/ETOH
- SOURCE to specify INHIBFRACTION in the mass source

- INITIALCONDITIONS to specify INHIBFRACTION at initial time
- NODE to specify INHIBFRACTION at the boundary
- TRENDDATA/PROFILEDATA/OUTPUTDATA to print compositional variables for given components
- HYDRATECURVE and HYDRATECHECK to calculate the effect on the hydrate formation temperature

In this study, the INHIBFRACTION was defined for both MEG and methanol simulations. The former is the mass fraction of the inhibitor in the total aqueous phase; the latter is the mass fraction of the inhibitor in relation to the total aqueous phase plus water vapor.

Figure 5-1 shows a schematic of the jumper facility with the approximate geometry constructed using OLGA® flow path editor. Figure 5-2 is the jumper system layout with OLGA® 7.

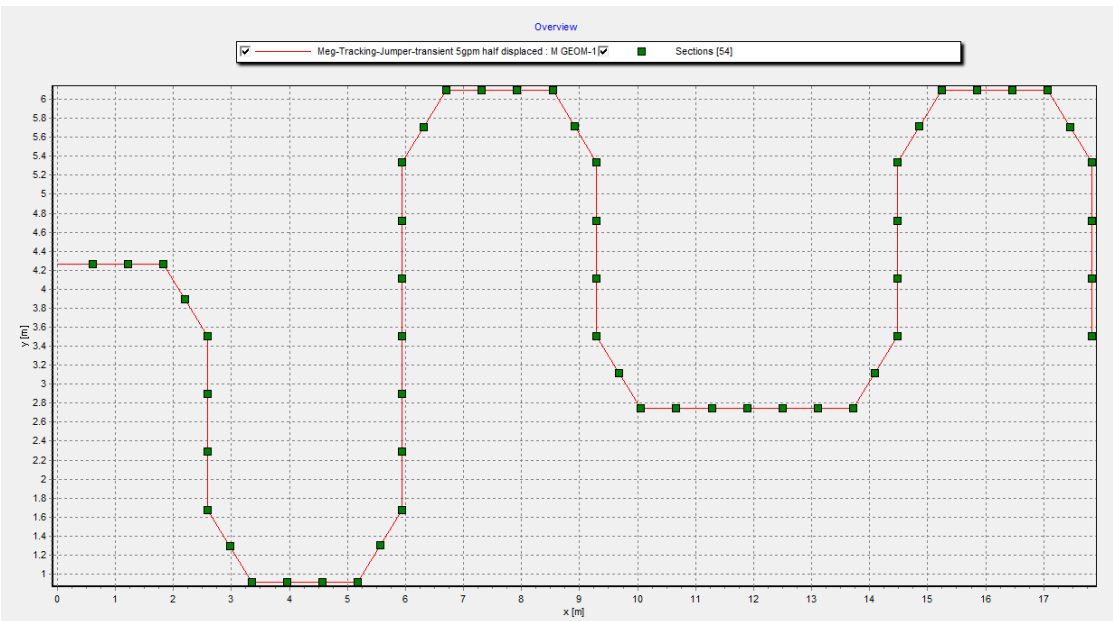

FIGURE 5 - 1: JUMPER GEOMETRY BUILT IN OLGA

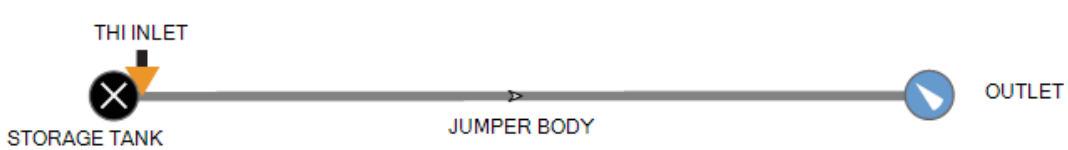

FIGURE 5 - 2: OLGA 7 JUMPER SYSTEM LAYOUT

This section describes the parameter settings for the OLGA simulations. Parameter settings in OLGA 7 for THI displacement with Jumper:

- Integration

  MAXDT = 0.1s, MAXTIME = 0s, MINDT = 1e-006s, DTSTART = 0.1s

  MAXLAGFACT = 0.3

- Insulation and walls

  Pipe material: Polycarbonate, density = 7850 g/cm^3, Heat capacity = 500 J/kg-ºC

  Conductivity = 50 W/m-ºC, wall thickness = 0.009m

- Boundary conditions

  Inlet with closed node: Gas mass fraction = -1

  Outlet with pressure node: Pressure = 14.7 psia, Temperature = 25°F,

  Gas mass fraction = 0, Water mass fraction = 1

- Heat transfer for the BRANCH

  HAMBIENT (mean heat transfer coefficient on outer wall surface) = 250 W/m^2-ºC

  HMININNERWALL (minimum inner heat transfer coefficient on inner wall surface) = 10 W/m^2-ºC

- Initial conditions

  Mass flow = 0 gpm at inlet and branch

  Void fraction = 0

- Sources

  Mass flow at the inlet node: Pressure = 11.4 psia, Temperature = 25°F, Gas mass fraction = 0, Water fraction = 1

  Compositional =MEOH, INHIBFRACT = 0.8

  A similar OLGA setup was made for the MEG 1D simulation as the methanol case, except the keyword for “COMPOSITIONAL” was changed from “MEOH” to “MEG”.

5.1.3 OLGA 1D simulations for results

5.1.3.1 OLGA 1D simulations for MEG displacement tests

The four MEG experiments with a full jumper loading and one volume displacement were simulated. Figure 5-3 compares the predicted MEG concentration profiles to the experimental MEG mass fractions measured. Even though the OLGA simulations reflect the overall structures in the developing mixing fronts, differences still exist for all four cases. Due to the lack of the mass transfer effect, the calculated MEG mass fractions in the test section are smaller than in reality for low injection velocity case (0.03 ft/s). For relatively high injection velocity cases, a fairly good agreement was made from OLGA simulation compared to the experimental data. Improvement has been achieved by making sure the same injection rates were used as in the tests.

Susanna Mele (2010) had also performed OLGA 1-D simulations for MEG for all range of injection velocities with full fresh water loading and one jumper volume of MEG displaced. Figure 5-4 shows the comparison between experimental data (Mele, 2010) and OLGA simulated concentration profiles of MEG. Mele's simulations also reflect the overall experimental trends. However, in all cases OLGA underestimated the amount of glycol dispersed along the jumper system significantly. At low injection rates, deviations (average deviations around -10 percent) on the simulation results may be related to the fact that the contribution of diffusion into the mixing process is ignored by the tracking module. At high MEG injection flow rates, it seems that the equations of transport associated to this commercial package may not take into account the physics behind the plug displacement phenomenon perceived. The differences are also introduced by the nominal flow rates inputs for the simulations rather than the corresponding actual flow rates from Mele (2010) MEG displacement test.

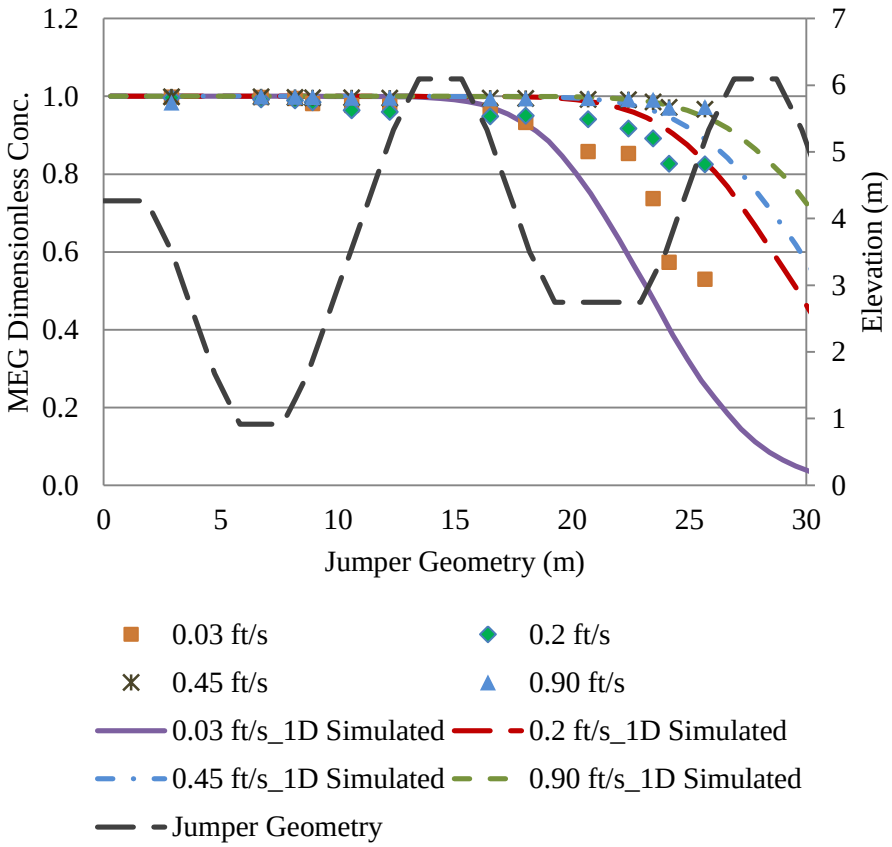

FIGURE 5 - 3: REPEATED EXPERIMENTAL VS. OLGA SIMULATED

Repeated experimental vs. OLGA simulated concentration profiles of MEG in the jumper facility (Full liquid loading; 1 jumper volume displaced; Fresh water)

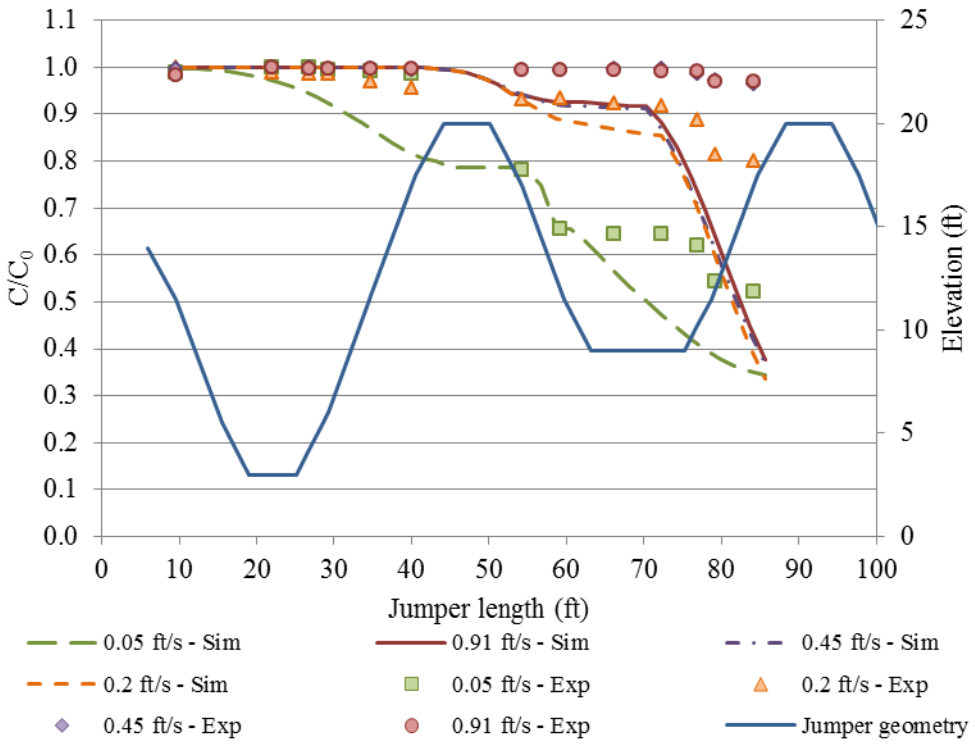

FIGURE 5 - 4: EXPERIMENTAL VS. OLGA SIMULATED

Experimental vs. OLGA simulated concentration profiles of MEG in the jumper facility (Full liquid loading; 1 jumper volume displaced; Fresh water) (Mele, 2010)

Figure 5-5 depicts the relative differences linked to the predictions carried out by the OLGA MEG Tracking module for all the operational conditions specified above by Mele (2010). Figure 5-6 plots the relative differences between the predicted and experimental MEG dimensionless concentration profiles for all the MEG tests repeated in this work. The Mele simulation outcomes that were produced showed that the OLGA model yields a relatively good agreement with the experimental data in those situations in which transport constitutes the prevailing mechanism of the dispersion process (Average deviations around -10 percent are obtained as shown in Figure 5-6.). However, for those areas in which high concentration differences between the glycol solution and

the aqueous phase exist (i.e., where mixing is still taking place), larger differences are obtained (down to about -60 percent).

From Figure 5-6, we can see that a better agreement between the OLGA simulations and experiments is obtained for the repeated MEG tests. All tests fall within ± 5 percent for all injection rates at the sections before the first high spot. The improvements may come from the fact that actual measured flow rates were used in the simulation inputs. The predicted results by OLGA were all within ± 10 percent, except for the low velocity of 0.05 ft/s in which a difference of about 50 percent still remains.

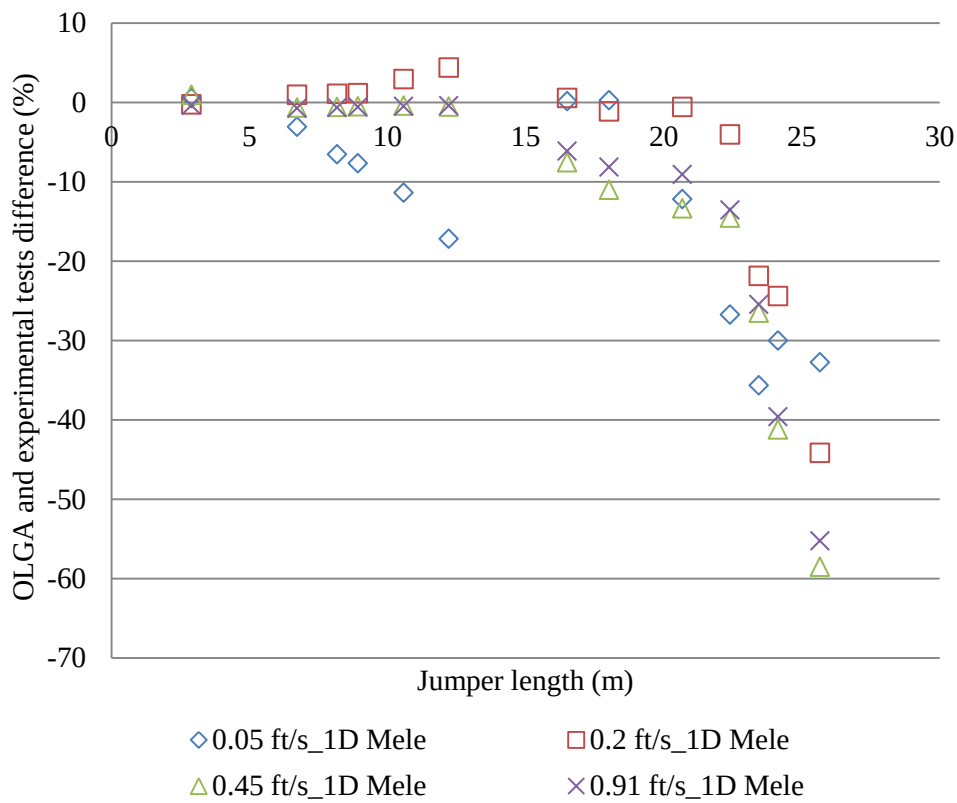

FIGURE 5 - 5: OLGA MEG TRACKING MODULE PERFORMANCE, MELE (2010)

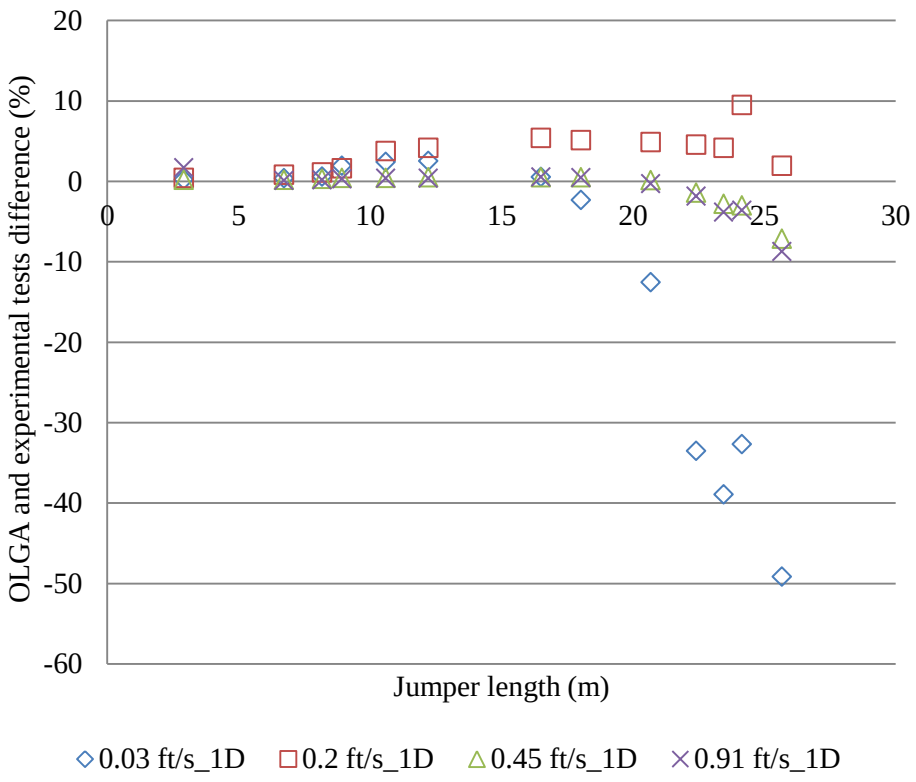

FIGURE 5 - 6: OLGA MEG TRACKING MODULE PERFORMANCE FOR REPEATED MEG TESTS

5.1.3.2 OLGA 1D simulations for methanol displacement tests

OLGA 1D model simulations were made for the four different methanol injection rates. Figure 5-7 compares the simulation results with the measured methanol concentrations. The solid lines represent OLGA results. From the graph, it can be noticed that the OLGA simulations captured the overall trends in the developing mixing fronts. The results in the vertical sections of the simulation deviated from the experiments with methanol dimensionless concentrations only ranging from 0 to 0.56. However, in all cases predictions that were performed using OLGA failed to simulate methanol overriding the water phase at either low spot. Due to the lack of mass transfer effect, the predicted methanol mass fractions in the last riser were lower than experimentally

measured. The overall results showed that the 1D transient model was unable to predict mixing effects in the horizontal sections.

The OLGA inhibitor tracking module assumes that the inhibitor is completely miscible (and will always be evenly mixed) throughout the aqueous phase at each local numerical section in each time step. OLGA also assumes negligible diffusion of the inhibitor into the water phase, and the inhibitor does not affect the flow behavior. However, observations made during the tests indicated that the process of distributing an inhibitor solution into a jumper configuration certainly generated different flow mechanisms according to the superficial velocity of the displacing fluid. Due to extreme amounts of multiphase chaos associated with instantaneous change from initial condition (zero flow rate) to the specified mass flow source boundary condition, OLGA's semi-implicit numerical solver is required to set a small time step for inhibiter injection cases when transient multiphase chaos is present. A relatively long time step promotes loss of mass/volume conversation.

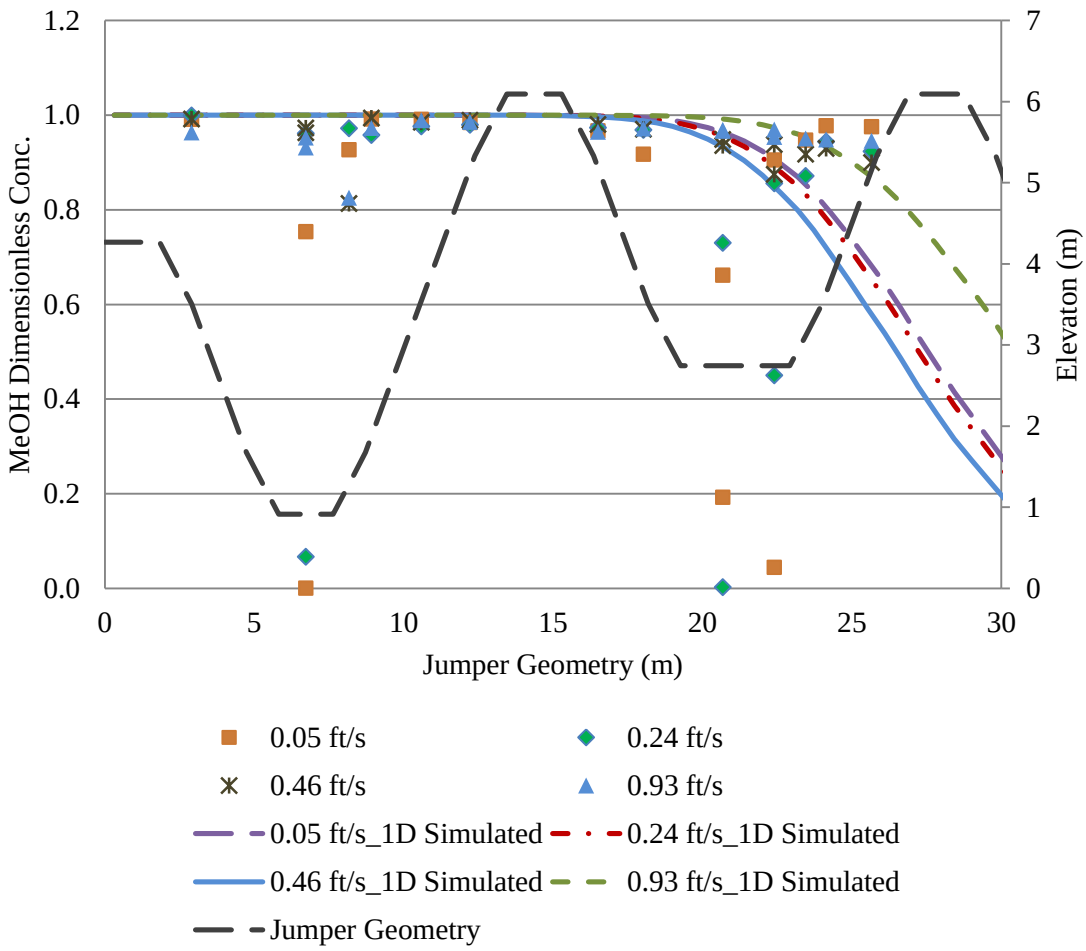

FIGURE 5 - 7: EXPERIMENTAL VS. OLGA® SIMULATED

Experimental vs. OLGA® simulated concentration profiles of methanol in the jumper facility (full liquid loading; 1 jumper volume displaced; fresh water; all range of velocities)

5.2 CFD (FLUENT®) simulations

5.2.1 CFD model description

5.2.1.1 CFD 2D computational mesh

The jumper 2D computational mesh was constructed using GAMBIT® version 2.3.16, as shown in Figure 5-8. The geometry is modeled as two-dimensional axisymmetric with quadrilateral cells. The diameter of the entire flow region is 3 inch and total length is about 100 feet, which is the same as the jumper apparatus. In the flow region, the grid is finer near the pipe wall and at the inlet T-section, with five prism layers to better capture boundary layer effects in the near-wall regions. In the rest of the geometry the grid is coarser, as shown in Figure 5-8 (a). The total number of cells used for this geometry is 289,200.

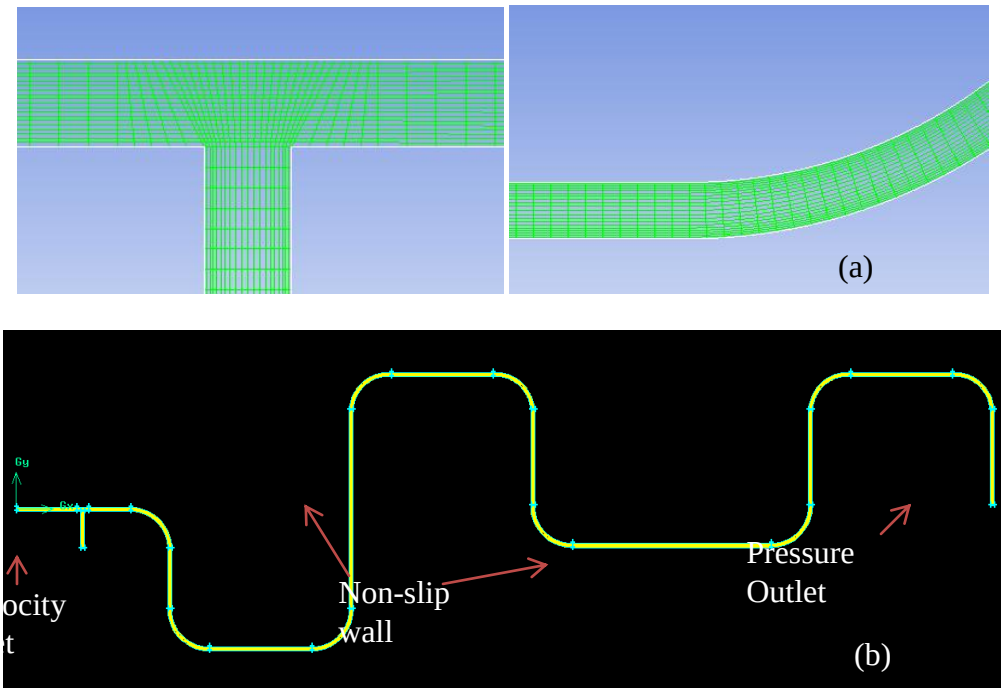

FIGURE 5 - 8: GRID STRUCTURE AND JUMPER 2D GEOMETRY

(a) Grid structure of the face mesh with near-wall prisms layers
(b) Jumper 2D geometry mesh with GAMBIT

5.2.1.2 Fluid materials

To simulate the jumper displacement tests with methanol, density and viscosity correlations as a function of methanol mass fraction were also included in the CFD model to estimate transport effect on the predicted concentration profiles of methanol along the jumper system. The methanol-water mixture physical properties were defined by user defined functions (UDF) and the correlations used for the solution properties that were found in the CRC Handbook of Chemistry and Physics. Equations 5.3, 5.4, and 5.5 are the correlations for density, viscosity and diffusion coefficient at 25ºC of the methanol - water solutions, respectively, where x represents the mass fraction of methanol. Equations 5.6, 5.7, and 5.8 are the correlations for density, viscosity, and diffusion coefficient at 25ºC of the methanol - water solutions, respectively, where x represents the mass fraction of methanol.

$$\rho_{MeOH} = 0.109x^4 - 0.25x^3 + 0.106x^2 - 0.17x^2 + 0.998 \quad (5.\ 3)$$

$$\nu_{MeOH} = -11x^5 + 30.83x^4 - 28.1x^3 + 4.908x^2 + 2.92x + 1.008 \quad (5.\ 4)$$

$$Diff_{MeOH} = -8.28x^5 + 21.6x^4 - 17.6x^3 + 7.666x^2 - 2.79x + 1.563 \quad (5.\ 5)$$

$$\rho_{MEG} = 1\times10^{-8}x^3 - 3\times10^{-6}x^2 + 0.0015x^2 + 0.9976 \quad (5.\ 6)$$

$$\nu_{MEG} = 3.238\times10^{-2}x^4 - 3.39\times10^{-2}x^3 + 1.85\times10^{-2}x^2 - 1.5\times10^{-4}x + 9.67\times10^{-4} \quad (5.\ 7)$$

$$Diff_{MEG} = 4.908\times10^{-10}x^2 - 1.249\times10^{-9}x + 1.197\times10^{-9}x \quad (5.\ 8)$$

5.2.1.3 Initial conditions and boundary conditions

The initial fluid velocity (in both x and y directions) and the methanol concentration is zero corresponding to t = 0 sec, which are patched into all the cells in the jumper 2D computational grid for full liquid loading situations. The initial value for gauge pressure is 0 Pascal and the temperature is 300 K. The values for turbulent kinetic energy and turbulent dissipation rate are set as default.

Figure 5-8 (b) illustrates the faces for velocity inlet and pressure outlet. The velocity at the velocity-inlet boundary is set to the experimental methanol injection velocity. Gauge pressure at the pressure-outlet is set to 101,325 Pascal. The species mass fraction of methanol for both boundaries is 0.8, corresponding to the bulk concentration of injected methanol from the storage tank. The jumper body is modeled as a no-slip stationary wall with constant roughness 0.5 (default value from FLUENT).

5.2.1.4 Operating conditions

The operating pressure is 101,325 Pascal and the reference pressure location is at the start point (0, 0) for adjusting the gauge pressure filed for incompressible flows. Gravity is included to simulate the buoyancy effect on methanol diffusion into water for all injection velocity cases. The gravitational acceleration is set as -9.81 m/s^2 at y direction and 0 m/s^2 at x direction.

5.2.1.5 Turbulence model

The Navier-Stokes equations describing the process of momentum, heat, and mass transfer can be discretized and solved numerically. Equations 5.9 and 5.10 describe the conservation of mass, which are also called continuity equations. Equation 5.11 is the Navier-Stokes equation (conservation of momentum), and Equation 5.12 is the energy equation.

$$\frac{\partial \rho}{\partial t} + \nabla \cdot (\rho \vec{u}) = 0 \tag{5. 9}$$

$$\frac{D\rho}{Dr} = 0 \tag{5. 10}$$

$$\rho \frac{\partial \vec{u}}{\partial t} + \rho \vec{u} \nabla \vec{u} = -\nabla P + \rho f_b + \nabla \cdot \mu \left(\nabla \vec{u} + \nabla^T \vec{u} \right) \tag{5. 11}$$

$$\frac{\partial \rho (e + \mathbf{V}^2/2)}{\partial t} + \frac{\partial \rho u_i (e + \mathbf{V}^2/2)}{\partial x_i} = -\frac{\partial q_i}{\partial x_i} + \frac{\partial u_i \sigma_{ji}}{\partial x_j} + \rho u_i B_i \tag{5. 12}$$

Reynolds Averaged Navier-Stokes (RANS) equations with time-averages can be used to solve turbulent flow. Equations 5.13 and 5.14 are the continuity and momentum equations for the RANS model (Okita, 2010). The term $-\rho\overline{u'_\iota u'_J}$ represents Reynolds stresses and needs to be modeled to close the RANS equations. There are two particular two-equation turbulence models that can provide a good compromise between numerical effort and computational accuracy, namely the k-Ω and k-ε models.

$$\frac{\partial \rho}{\partial t} + \frac{\partial}{\partial x_i}(\rho u_i) = 0 \tag{5.13}$$

$$\frac{\partial \rho u_i}{\partial t} + \frac{\partial \rho u_i u_j}{\partial x_j} = -\frac{\partial p}{\partial x_j} + \frac{\partial}{\partial x_j}\left[\mu\left(\frac{\partial u_i}{\partial x_j} + \frac{\partial u_j}{\partial x_i} - \frac{2}{3}\delta_{ij}\frac{\partial u_j}{\partial x_j}\right)\right] + \frac{\partial}{\partial x_j}(-\rho\overline{u_i^{'}u_j^{'}}) \tag{5.14}$$

The k-Ω and the k-ε two-equation models use the gradient diffusion assumptions to relate the Reynolds stresses to the mean velocity gradients and the turbulent viscosity. The turbulent viscosity is modeled as the product of a turbulent velocity and turbulent length scale. In two-equation models, the turbulence velocity scale is computed from the turbulent kinetic energy, which is provided from the solution of its transport equation. The turbulent length scale is estimated from two properties of the turbulence field, usually the turbulent kinetic energy and its dissipation rate. The dissipation rate of the turbulent kinetic energy is provided from the solution of its transport equation.

The Standard k-ε model was proposed by Launder and Spalding (1972). It is a semi-empirical model based on k and ε equations. The k-ε model assumes that the flow is fully turbulent and that the effects of molecular viscosity are negligible. Equations 5.15 and 5.16 are the transport equations for kinetic energy, k, and rate of dissipation, ε.

$$\frac{\partial(\rho k)}{\partial t} + \frac{\partial(\rho u_i k)}{\partial x_i} = \frac{\partial}{\partial x_j}\left[\left(\mu + \frac{\mu_t}{\sigma_k}\right)\frac{\partial k}{\partial x_j}\right] + G_k - \rho\varepsilon \tag{5.15}$$

$$\frac{\partial(\rho\varepsilon)}{\partial t}+\frac{\partial(\rho u_i\varepsilon)}{\partial x_i}=\frac{\partial}{\partial x_j}\left[\left(\mu+\frac{\mu_t}{\sigma_\varepsilon}\right)\frac{\partial\varepsilon}{\partial x_j}\right]+C_{1\varepsilon}\frac{\varepsilon}{k}(G_k)-C_{2\varepsilon}\rho\frac{\varepsilon^2}{k} \tag{5.16}$$

G_k is the production of turbulence kinetic energy due to the gradients of mean velocity and calculated in Equation 5.17.

$$G_k=-\rho\overline{u_I^{'}u_j^{'}}\frac{\partial u_j}{\partial x_i} \tag{5. 17}$$

Turbulent viscosity, μ_t, is calculated using Equation 5.16. The model constants are $C_{1\varepsilon}$=1.44, $C_{2\varepsilon}$=1.92, C_μ=0.09, σ_k=1.0, and σ_ε=1.3.

For the k-Ω turbulent model, one of the advantages is the near wall treatment for low-Reynolds number computations. A low-Reynolds k-ε model would typically require a near wall resolution of $y^+<0.2$, while a low-Reynolds number k-Ω model would require at least $y^+<2$. In industrial flows, even $y^+<2$ cannot be guaranteed in most applications and, for this reason, a new near wall treatment was developed for the k-Ω models. It allows for a smooth shift from a low-Reynolds number form to a wall function formulation. The k-Ω models assume that the turbulence viscosity is linked to the turbulence kinetic energy and turbulent frequency via the relation Equation 5.18:

$$\mu_t=\rho\frac{k}{\omega} \tag{5. 18}$$

where μ_t is the kinematic eddy viscosity, k is the turbulent kinetic energy, and ω is the specific dissipation rate.

$$\frac{\partial k}{\partial t}+U_j\frac{\partial k}{\partial x_j}=\tau_{i,j}\frac{\partial U_i}{\partial x_j}-\beta^*k\omega+\frac{\partial}{\partial x_j}\left[(\nu+\sigma^*\nu_T)\frac{\partial k}{\partial x_j}\right] \tag{5. 19}$$

$$\frac{\partial\omega}{\partial t}+U_j\frac{\partial\omega}{\partial x_j}=\alpha\frac{\omega}{k}\tau_{ij}\frac{\partial U_i}{\partial x_j}-\beta\omega^2+\frac{\partial}{\partial x_j}\left[(\nu+\sigma\sigma_T)\frac{\partial\omega}{\partial x_j}\right] \tag{5. 20}$$

The closure coefficients and auxiliary relations are given by:

$$\alpha = \frac{5}{9}, \beta = \frac{3}{40}, \beta^* = \frac{9}{100}, \sigma = \frac{1}{2}, \sigma^* = \frac{1}{2}, \varepsilon = \beta^* \omega k \quad (5.\ 21)$$

5.2.1.6 Solver control and discretization schemes

The pressure based first-order implicit unsteady solver was selected. Other settings to define the solver in FLUENT remain at default parameters. The fractional step algorithm is applied for the pressure-velocity coupling to enhance the convergence of non-iterative calculations for unsteady incompressible flow. A second-order upwind scheme is used to discretize the governing transport equation of convection-diffusion of inhibitor. The PRESTO! (Pressure Staggering Option) scheme is chosen to compute pressure, which is suggested for situations entailing significant body forces. The QUICK scheme (Quadratic Upstream Interpolation for Convective Kinetics), which is typically more accurate on structured grids aligned with the flow direction, is selected for momentum.

5.2.1.7 Time stepping and convergence

Time steps are defined to track the real time progress during the transient simulations. The proper time step size is important to obtain good convergence within reasonable amount of CPU usage. Within a given time step the transport equations are solved during an iterative process until the convergence criteria is met for all equations. For the low methanol injection rate cases (0.05, 0.2 ft/s), the time step was set to 0.1s. For high methanol injection rate cases (0.45, 0.91 ft/s), it was set to 0.05s. Each time step was considered to be converged when the maximum residual value was no higher than 1×10^{-3}.

5.2.2 FLUENT® simulation results with MEG

Four 2D FLUENT® simulations were conducted for repeated MEG full water loading and one jumper volume displacement tests. The same simulation setups were followed as Mele (2010)'s CFD study except for the inlet boundary condition, which was set to the actual recorded experimental injection velocities. More details of the simulation setups can be found in her thesis. Figure 5-9 shows the contour of MEG mass fraction at time = 1.06 minute predicted by FLUENT® for 0.45 ft/s injection velocity. It is clear to see that the heavier MEG phase flows at the bottom of the horizontal section. This concentration difference in the radial direction vanishes as the simulation runs for longer time, as observed from the corresponding jumper experiment.

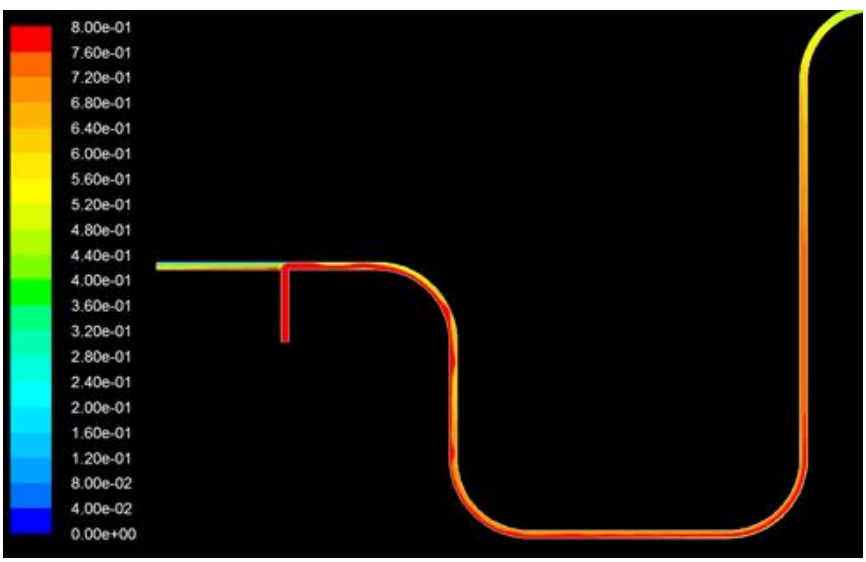

FIGURE 5 - 9: CONTOUR OF MEG MASS FRACTION

Contour of MEG mass fraction at time = 1.06 min predicted by FLUENT® for 0.45 ft/s injection velocity

Figure 5-10 shows the comparison between the repeated experimental and CFD 2D simulation profiles of MEG in the jumper facility for all the injection velocities studied. From the plot, good agreement was obtained between the 2D simulation results and the experimental data,

even though an under-predicted MEG concentration profile was shown for low injection rate case, especially after the first high spot. The difference ranges from -6 percent to -26 percent. For the higher injection rate, a better match was found as shown in Figure 5-9. The discrepancy decreased to the range from +3 to -9 percent.

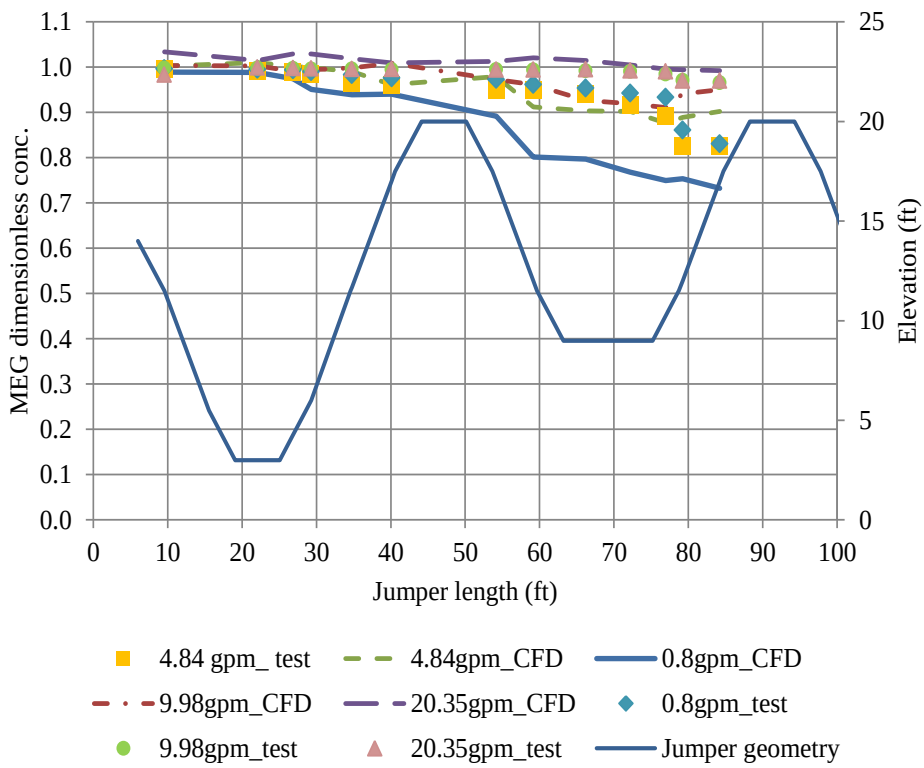

FIGURE 5 - 10: EXPERIMENTAL AND CFD 2D SIMULATIONS COMPARISON

Comparison between the repeated experimental and CFD 2D simulation profiles of MEG in the jumper facility

Figure 5-11 shows Mele's experimental and FLUENT® simulated concentration profiles of MEG in the jumper facility. The simulations were able to reproduce the physical phenomenon observations from the jumper experiments, like the long mixing front under low injection rates and piston-like mixing front under relatively high injection rates. However, under-predicted MEG concentration profiles were also obtained for all range of velocities cases, especially after the first

high spot. The differences between the simulated results and experimental data ranged from -7 to about -28 percent. These uncertainties are in the same range as obtained for this work.

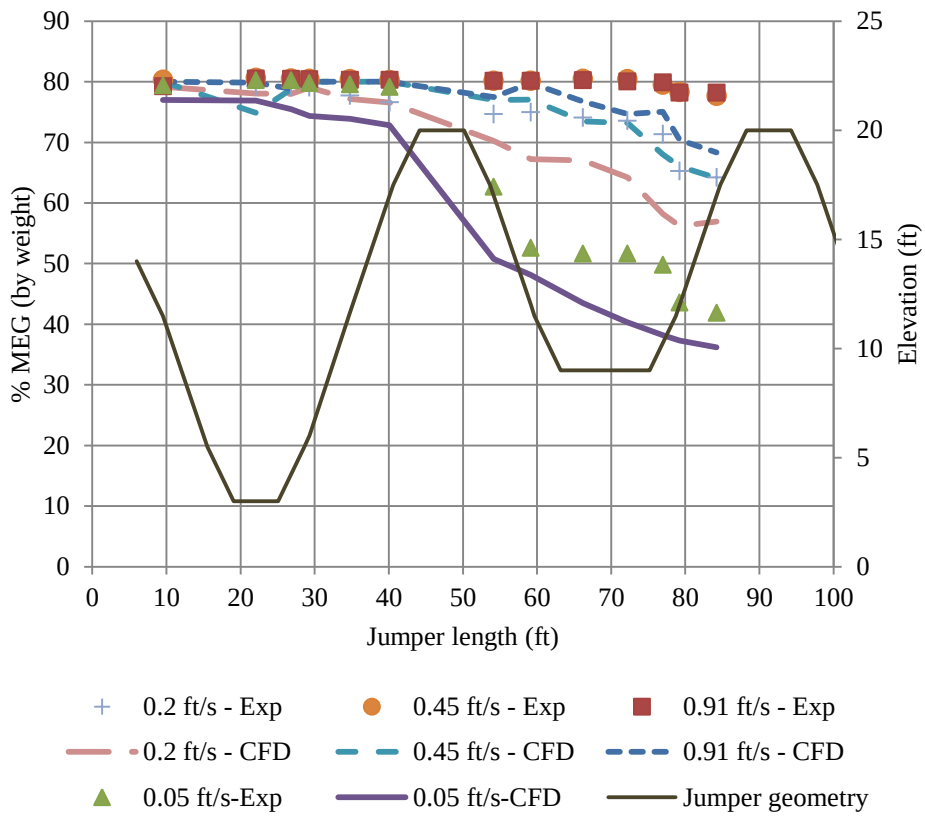

FIGURE 5 - 11: EXPERIMENTAL VS. FLUENT® SIMULATED CONCENTRATION PROFILES

Experimental vs. FLUENT® simulated concentration profiles of MEG in the jumper facility (full liquid loading; 1 jumper volume displaced; fresh water) (Mele, 2010)

5.2.3 FLUENT® simulation results with methanol

The full jumper fresh water loading with one jumper volume methanol displacement simulations were run at flow rates of 1.22, 5.35, 10.21, and 20.49 gpm. Two turbulent models, k-ε and k-Ω, were applied for the simulations, and the simulation results are presented in the following sections.

- k-ε turbulent model simulation results

Figure 5-12 compares the concentration profiles predicted by the CFD model and experimental results at low injection rates (1.22 and 5.35 gpm), and Figure 5-13 shows the comparison between the concentration profiles predicted by the CFD model and experimental results at high injection rates (10.21 and 20.49 gpm). The overall methanol concentration distribution along the jumper predicted by FLUENT reflects the experimental results. For the first three vertical sections, a good agreement with the empirical concentration gradients is obtained from simulations at four injection rates shown from both Figure 5-12 and Figure 5-13. The maximum difference observed is about 3 percent at these vertical sections. For the low injection rate runs, the simulations tend to under-predict the methanol concentrations in the last riser with nearly 34 percent difference. Meanwhile, over-predicted methanol concentrations were given by the simulations at higher injection rates as shown in Figure 5-13. However, as can be noticed from the plot, the simulated trends were not able to reproduce the methanol overriding water phase at both horizontal low spots as was observed in all the tests. Especially for the low injection rate cases, the methanol segregation at the low spots was not properly simulated by the 2D simulations (Figure 5-12).

Figure 5-14 shows the contour of methanol mass fraction at different times that was predicted with the k-ε model at 1.22 gpm injection rate with full liquid loading and one jumper volume injected. At the beginning of the simulation (t=0.53 min), methanol rose from inlet to the top of the T-section caused by the buoyancy force and a strong dispersion of methanol into the water phase that was simulated at this point. When methanol reached the first horizontal low spot, the simulation did capture methanol flowing on top of the water phase, and the long mixing front was also simulated for the first few minutes; however, as the simulation kept running, the horizontal section eventually filled up with methanol until the water layer disappeared by the end of the

simulation. It seems that the gravitational force may have affected methanol dispersion into the water phase more than experimental results showed. Moreover, the turbulent model may not have been the best model for the horizontal sections, since a stratified laminar flow dominated at both low spots and more diffusion could be introduced by the turbulent model. For the vertical up comers, a long methanol mixing front was reproduced as shown in Figure 5-14 when t = 5.78 min. As soon as methanol channeled through the elbow section and reached the riser, a methanol column built up on top of the water phase at the bottom of the riser. At the downcomers the methanol front was piston-like and pushed the water out of the jumper. These details, shown in the methanol mass fraction contours, matched the observation made from the jumper experiments, as shown in Figures 4-9 and 4-11. At the end of the simulation (t = 28.5 min), most of the water was displaced from the jumper, as shown in the last contour in Figure 5-14. However, as stated above, even the water layers in the low spots disappeared, which was not observed in the experiments.

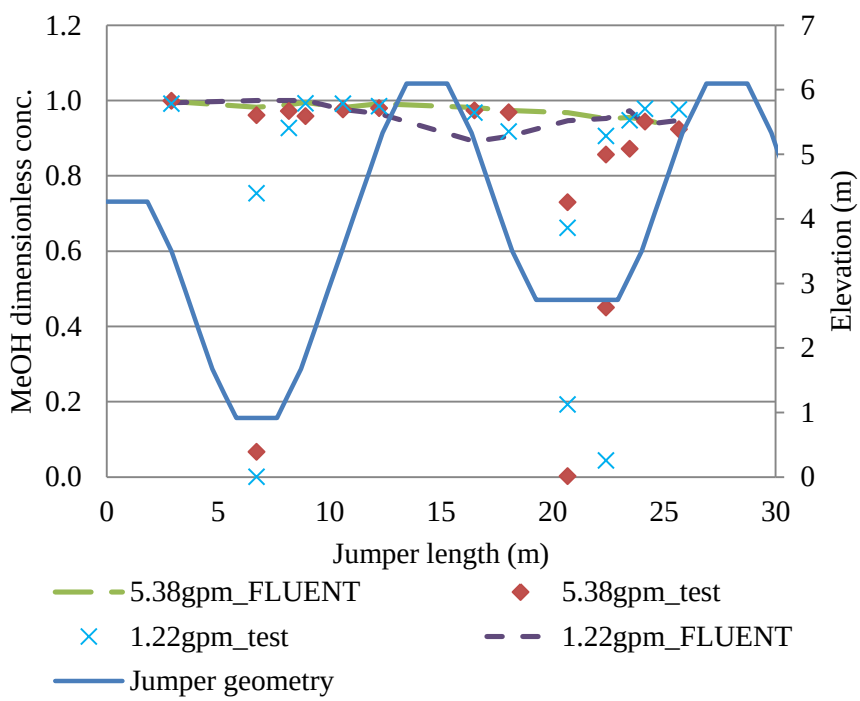

FIGURE 5 - 12: EXPERIMENTAL VS. CFD PREDICTIONS

Comparison between the concentration profiles predicted by the CFD model and experimental results at low injection rates

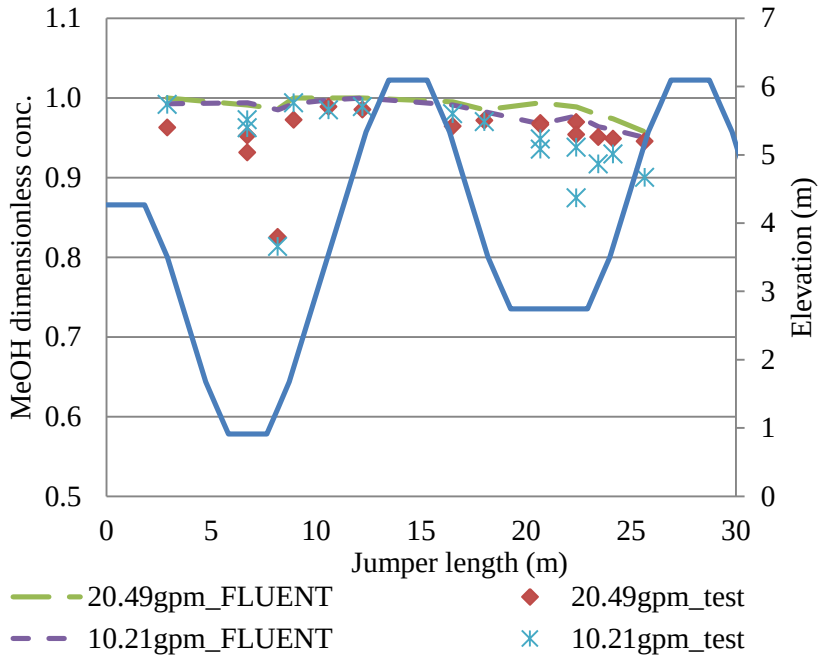

FIGURE 5 - 13: EXPERIMENTAL VS. CFD PREDICTIONS

Comparison between the concentration profiles predicted by the CFD model and experimental results at high injection rates

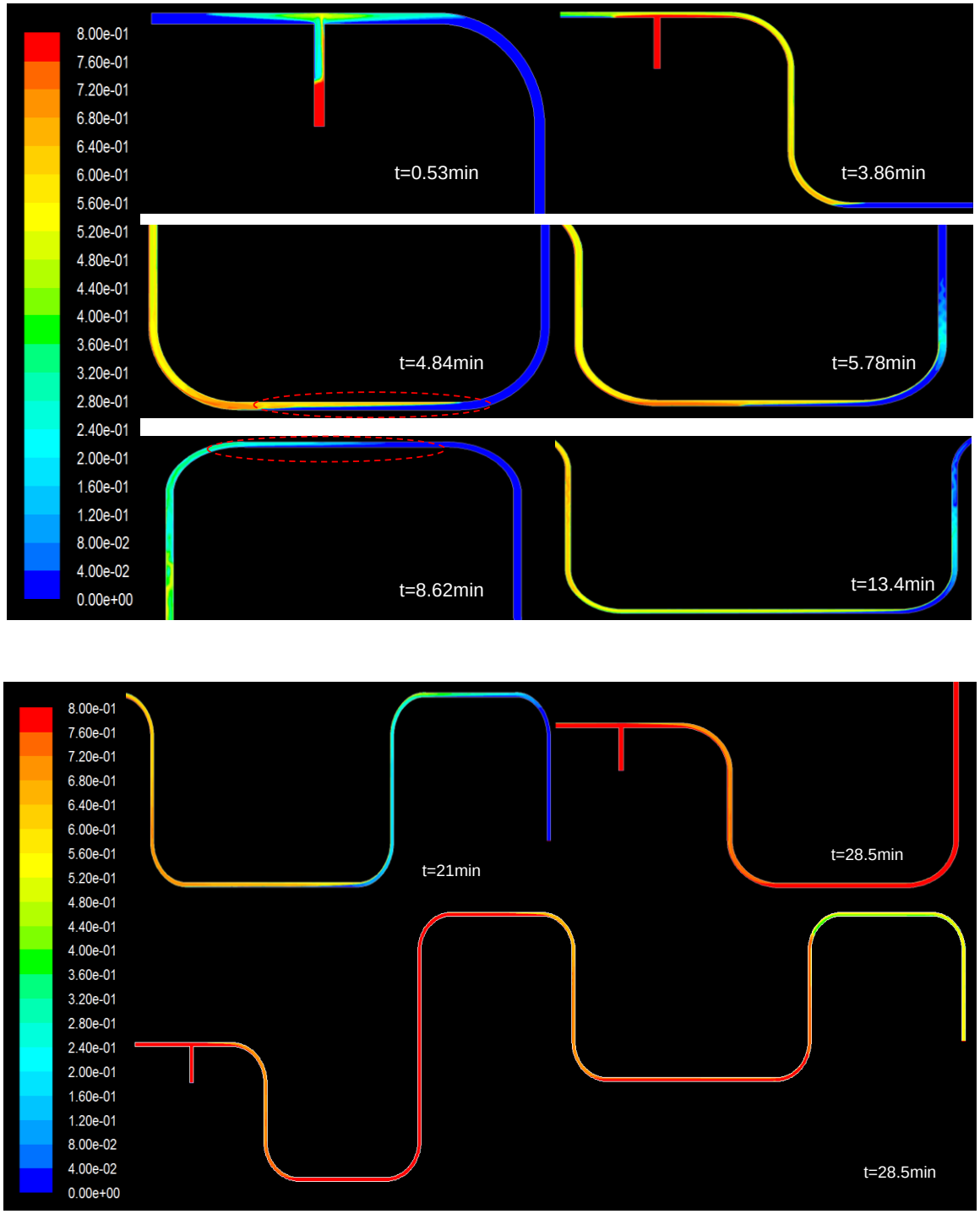

FIGURE 5 - 14: CONTOUR OF METHANOL MASS FRACTION

Contour of methanol mass fraction at different running periods predicted by 2D CFD with k-ε model at 1.22 gpm injection rate (full liquid loading and one jumper volume injected)

Figure 5-15 shows the contour of methanol mass fraction at different times as predicted by 2D CFD with the k-ε model for the 10.22 gpm injection rate with full liquid loading and one jumper volume injected. At high injection rate, a shorter mixing front was present at the horizontal section (t = 0.51 min), matching with the observations made from the experiments. At the end of simulation (t = 3.27 min), the jumper was full with methanol, and most of the water was flushed out of the jumper. The methanol mass fraction calculated at the both low spots was evenly distributed and well mixed with the water phase.

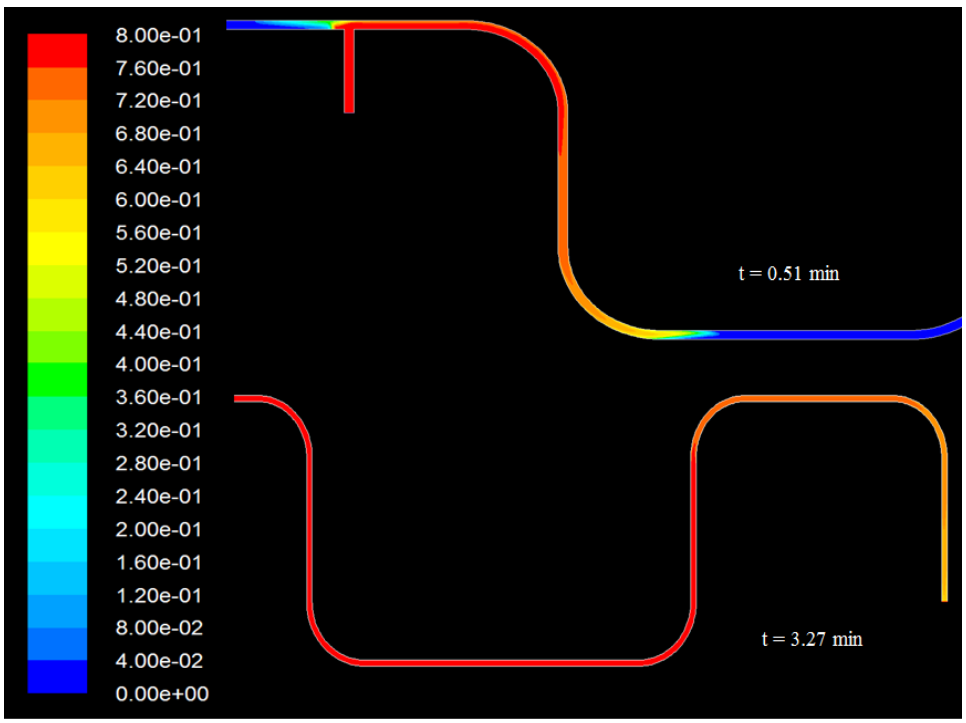

FIGURE 5 - 15: CONTOUR OF METHANOL MASS FRACTION

Contour of methanol mass fraction at different running periods predicted by 2D CFD with k-ε model at 10.21 gpm injection rate (full liquid loading and one jumper volume injected)

- k-Ω turbulent model simulated results

A different turbulent model was evaluated for simulating the methanol injection tests. Figure 5-16 shows the comparison between the concentration profiles predicted by the CFD Species

Transport model coupled with k-Ω turbulent model and experimental results at low injection rates (1.22 and 5.35 gpm), and Figure 5-17 shows the comparison between the concentration profiles predicted by the CFD Species Transport model coupled with k-Ω turbulent model and experimental results at high injection rates (10.21 and 20.49 gpm).

From the plot, it is easy to see that the k-Ω model predicts the methanol concentration profile along the jumper conservatively for all injection rates. It particularly under-predicted the mass fraction for the low injection rate case (1.22 gpm). It also has been noticed that the calculated methanol mass fraction right after the first high spot from four runs are all below the corresponding experimental data collected from tests. Insufficient methanol diffusion introduced by gravitational force was shown from the simulation. As shown in Figure 5-17, the high injection rate simulations give better predictions of the methanol mass fractions than the low injection rate simulation results. For the k-ε model simulations, methanol flowing on top of the water phase at both horizontal sections was not captured by the simulations, even though it appeared during the first few minutes after methanol reaches the horizontal sections. The buoyancy effect for methanol rising at the up comers was simulated for all the cases. The k-Ω model captures more mixing in the vertical downcomers as compared to the k-ε results.

Figure 5-18 shows the contour of methanol mass fraction at different times calculated by the k-Ω model at a 5.35 gpm injection rate with a full liquid loading and one jumper volume injected. At higher injection rate, the methanol mixing front is shorter and piston-like. A more uniform methanol distribution was predicted at both horizontal low spots. The diffusion of methanol in the vertical sections was significantly affected by the buoyancy force. A piston-like pushing front of methanol at the downcomers was clearly illustrated in Figure 5-18 at t = 0.59 min.

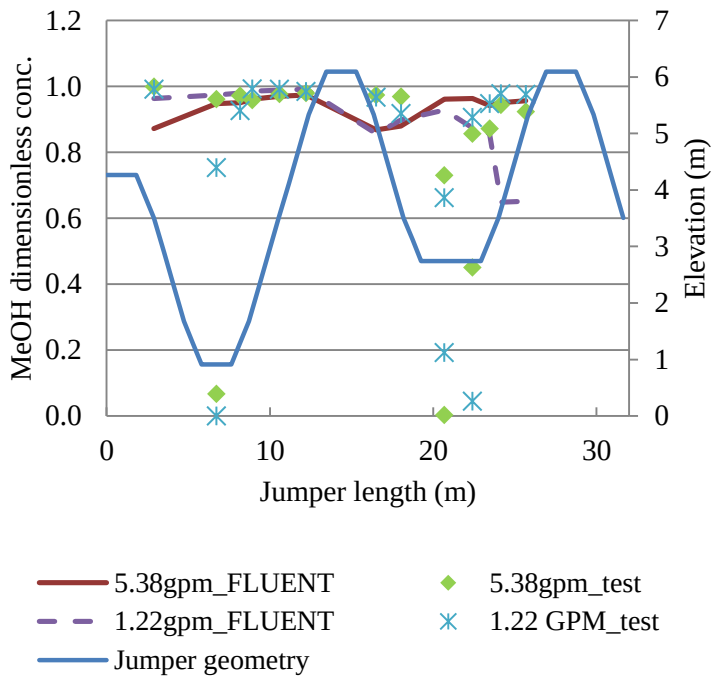

FIGURE 5 - 16: EXPERIMENTAL RESULTS VS. PROFILES PREDICTED BY THE CFD MODEL

Comparison between the concentration profiles predicted by the CFD model and experimental results at low injection rates

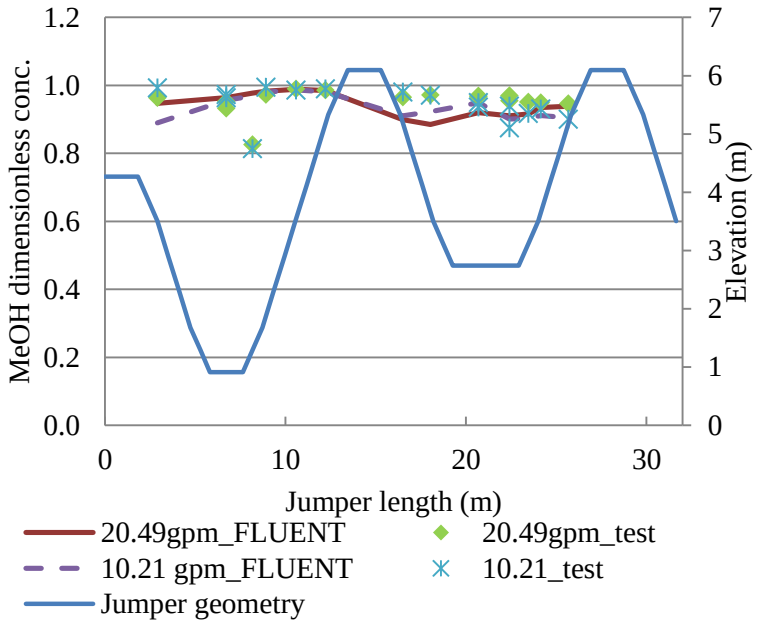

FIGURE 5 - 17: EXPERIMENTAL RESULTS VS. PROFILES PREDICTED BY THE CFD MODEL

Comparison between the concentration profiles predicted by the CFD model and experimental results at high injection rates

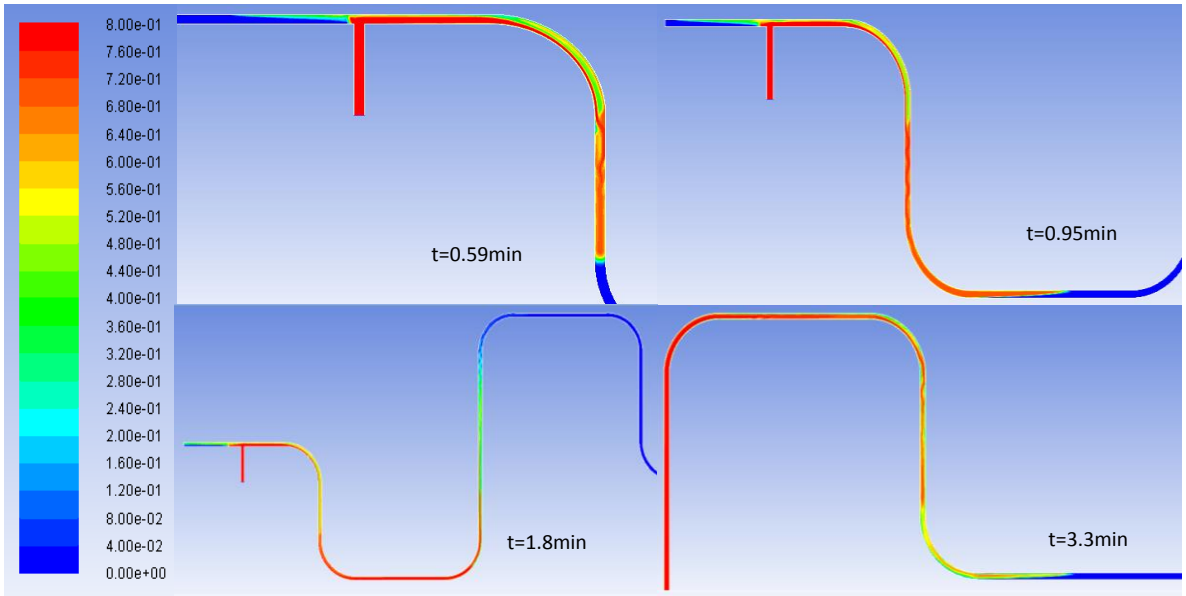

FIGURE 5 - 18: CONTOUR OF METHANOL MASS FRACTION

Contour of methanol mass fraction at different times predicted by the k-Ω model at 5.35 gpm injection rate (full liquid loading and one jumper volume injected)

5.3 3D CFD (STAR-CCM+®) simulations by CD-Adapco

CD-Adapco performed a numerical study of a water filled jumper being displaced tests with one jumper volume of THI (MEG and methanol) at four different rates using the CFD commercial software STAR-CCM+® (the results of this study are presented in appendix E). The results were compared to the outputs from 1D OLGA and 2D FLUENT simulation runs. The THI mixing process with water during injection was modeled with the transport species two-fluid model and the k-Ω two-equation turbulent model.The simulations were performed using STAR-CCM+ version 7.02.011. The 3D mesh was built with a collection of polyhedral cells. Gravity was included in the model because the density differences between the water and the two THIs of interest suggested that buoyancy would play a role in flow patterns, particularly at lower flow rates. Consider that the buoyancy effects in the jumper risers and downcomers could manifest as a waving, swirling, turbulent flow, so the model setup used Reynolds-Averaged Navier-Stokes equations with the SST k-Ω turbulence model and an all y+ wall treatment.

5.3.1 CFD 3D (STAR-CCM+) simulations for MEG

The nominal flow rates were 1, 5, 10, and 20 gpm. The actual flow rates from the experiments were 0.8, 4.84, 9.97, and 20.35 gpm, respectively. The test matrix projected respective experiment run times of 2,280, 454, 227, and 114 s for the 1, 5, 10, and 20 gpm flow rates. Figure 5-19 shows all the MEG simulations by Star-CCM+ and experiments on a single plot.

The simulation predicted the 0.8 gpm experiment well through sampling port 8, but then sampling ports 11 and 12 were off by around -28 percent and point 14 was off by -21 percent. The MEG simulations and experiments at 5 gpm compare well both qualitatively and quantitatively. The 4.84 gpm MEG/water simulation shows the same behavior in the low horizontal sections as seen in the experiment. In the first section, a heavy MEG layer extends along the bottom with a water layer above and then soon develops into a plug-like flow. The MEG experiments and simulations at 9.97 gpm and 20.35 gpm matched very well.

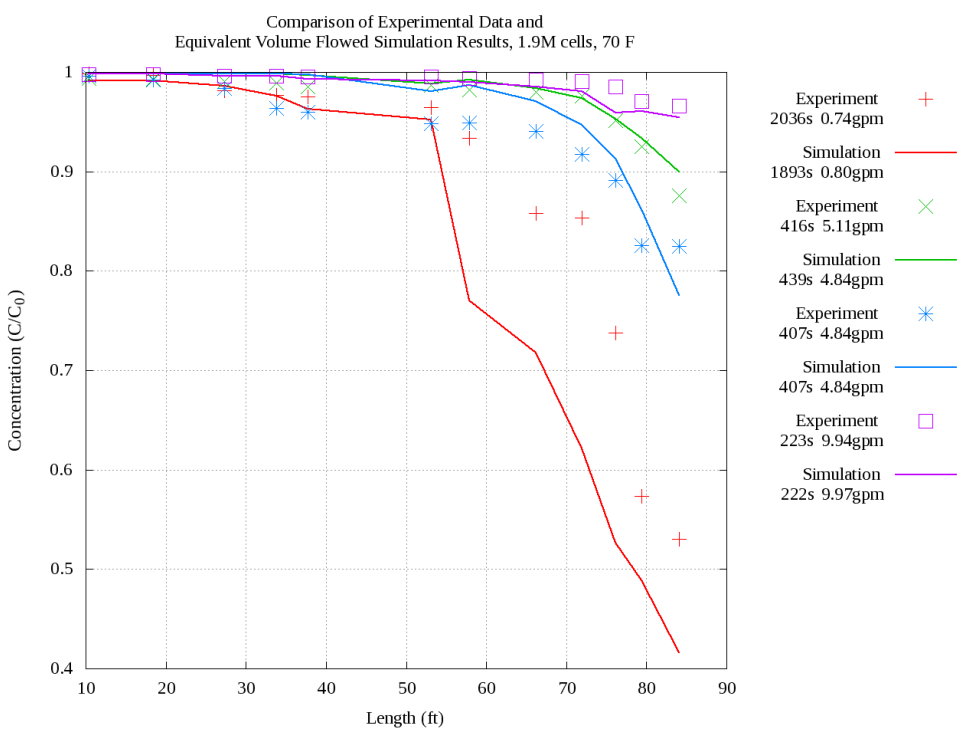

FIGURE 5 - 19: MEG CONCENTRATION PROFILES VS. EXPERIMENTAL RESULTS

Comparison between the MEG concentration profiles predicted by the Star-CCM+ CFD model and experimental results (CD-Adapco)

5.3.2 CFD 3D (STAR-CCM+) simulations for methanol

Figure 5-20 shows all the methanol simulations by Star-CCM+ and experiments on a single plot. The methanol simulations did not match the experiments, especially in the horizontal section where the segregation of methanol was not captured. As with the 2D model, the simulations did show two layers in the horizontal sections early in the run, but the layers disappeared prematurely. Aside from the horizontal sections and the last two sample points at 1 gpm, the simulations and experiments were within 10 percent of one another.

The effect of alternate turbulence models was tested by CD-Adapco on a reduced physical domain to shorten the computation time. The reduced domain stopped at the top of the first riser. A detached eddy simulation (DES) was used to try to improve on the turbulence modeling. The DES results still had two distinct layers at the end of the simulation, an improvement over the k- Ω results. However, the lower layer in the DES results had far too much methanol relative to the experiment. The experimental measurement was 0 methanol, while the dimensionless methanol content of the DES simulation ranged from 0.3 to 0.65, depending on the location within the lower layer. A laminar simulation was also run to eliminate the turbulence model completely along with any effects it may have had on the simulation. 3D CFD simulation did not achieve significant improvement in predicting the methanol concentration profile as compared to 1D and 2D simulations.

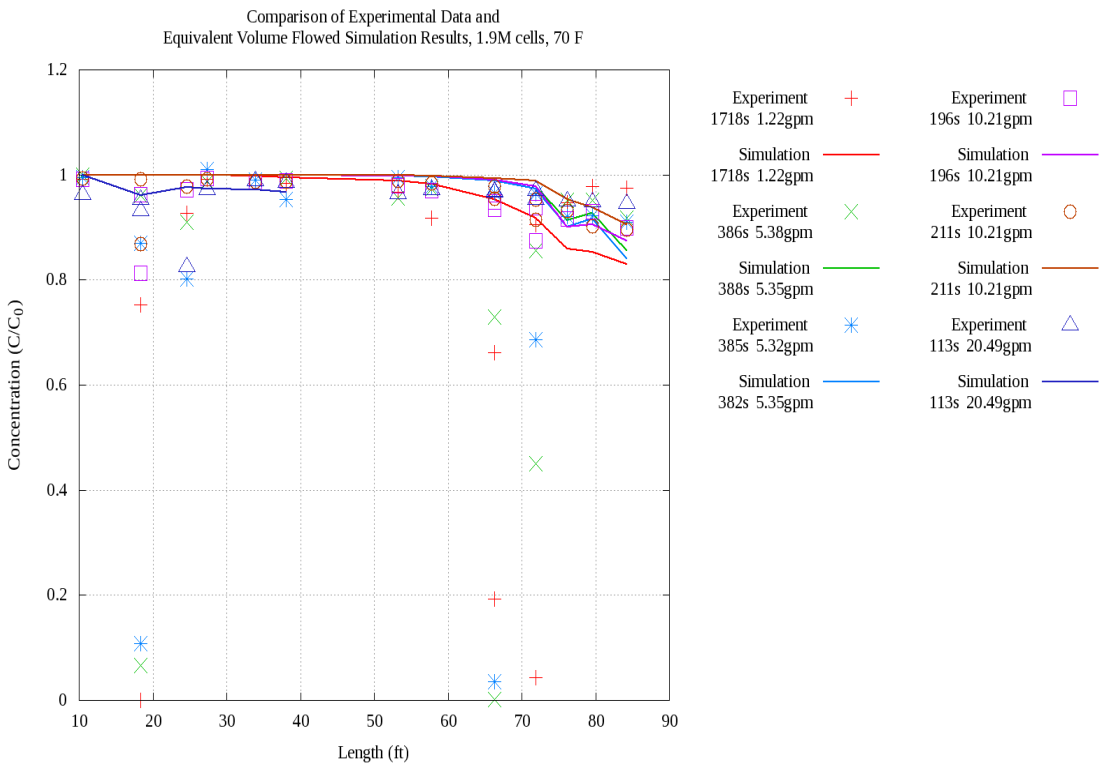

FIGURE 5 -20: MEG CONCENTRATION PROFILES VS. EXPERIMENTAL RESULTS

Comparison between the methanol concentration profiles predicted by the Star-CCM+ CFD model and experimental results (CD-Adapco)

5.4 Comparisons among 1D, 2D and 3D simulations for THI displacement tests

The performance of the CFD model was evaluated against the performance attained by the OLGA 1D transient model. For this purpose, simulation differences (%) were calculated for the predictions associated to each experimental point along the jumper. Positive values indicate an overestimation of the THI concentration, while negative values underestimate the inhibitor mass factions.

5.4.1 *Comparison among 1D, 2D, 3D simulations for MEG displacement tests*

As can be noticed from Figure 5-21, a large discrepancy exists for the OLGA low injection flow rate case (0.74 gpm simulation is off by up to -49 percent). As shown in Figure 5-21, even though there still remain moderate discrepancies between CFD simulation outcomes and

experimental measurements, numerical results obtained by means of the Species Transport model in 2D FLUENT® provide better accuracy and outperform the OLGA predictions for the low injection rate cases. The overall discrepancies linked to CFD 2D estimations are lower than those related to OLGA simulations, particularly in the jumper areas where convection and diffusion effects are still important. For example, for the same location in the jumper facility (sampling port 12), predicted MEG mass fractions by CFD 2D at all ranges of velocities have associated errors about -6 to -23 percent, whereas relative errors of OLGA estimations vary more widely. However, the errors associated with the 2D simulations are higher for the higher injection rates, especially after the first high spots. Insufficient diffusivity of MEG into water phase was exhibited from the under-predicted MEG concentration after the first high spot.

The 3D STAR-CCM+ MEG simulations and experiments show qualitatively similar behavior as shown in Figure 5-21. The low flow rate case was simulated with an expected flow rate of 0.8 gpm, but the experimental flow rate was off by 7.5 percent and was 0.74 gpm, as shown in Figure 5-21. The 5 gpm nominal flow rate case was simulated with an expected flow rate of 4.84 gpm. The simulation predicted the experiment well as the discrepancy between the simulation and experiment ranged from -6 to 4.3 percent. The experimental flow rate was very near the expected value of 9.94 gpm, off by only 0.3 percent. The simulation predicted the experiment well, as the discrepancy between the simulation and experiment ranged from -2.6 to 0.1 percent. Figure 5-24 shows that the 3D model simulations yielded the most accurate prediction for the MEG concentration distribution along the jumper. But for the high injection velocity case, all three simulation approaches were able to obtain fairly good agreement with experimental data.

OLGA can predict the overall trend of the MEG concentration profile; however, it failed to calculate the more commonly used in offshore THI injection MEG concentrations with small discrepancies for low injection rate cases (0.05 ft/s). Although there is still some work required to

refine the accuracy of the model predictions (modification of grid size, sensitivity to time steps, etc.), it is possible that CFD simulations are able to capture the flow and mass transfer phenomena encountered in jumper configurations with more detail during flushing procedures with thermodynamic inhibitors. However, 3D simulations require significant CPU capacity and increase the simulation run time.

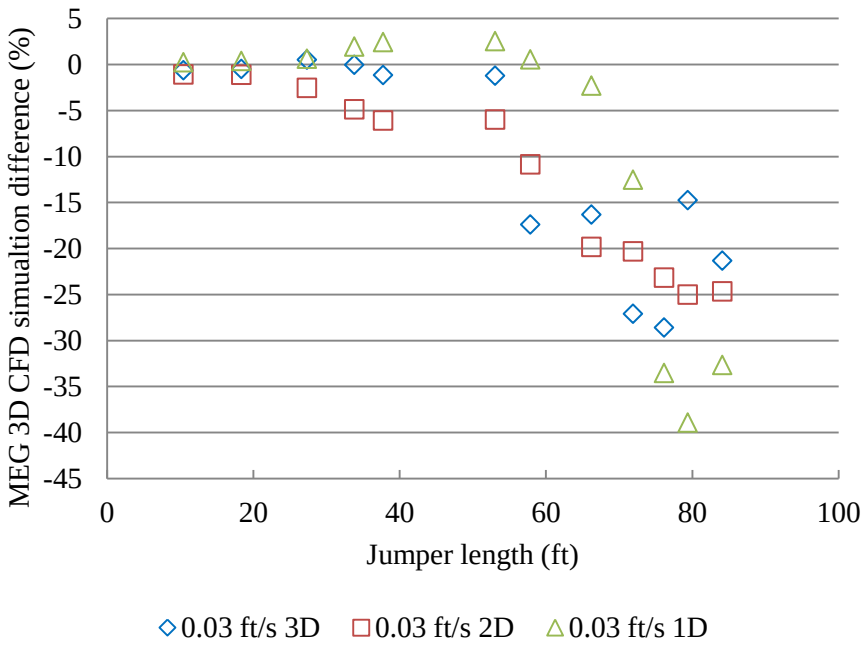

FIGURE 5 -21: DIFFERENCE IN INJECTION VELOCITY

Difference (%) associated to MEG 1D, 2D and 3D predictions
for 0.03 ft/s injection velocity (full liquid loading; 1 jumper volume displaced)

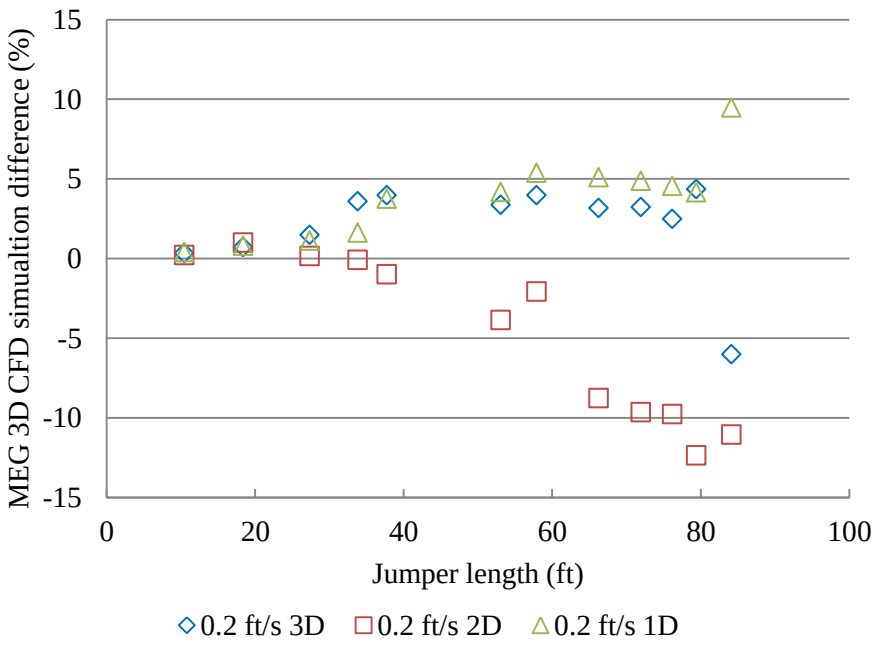

FIGURE 5 -22: DIFFERENCE IN INJECTION VELOCITY

Difference (%) associated to MEG 1D, 2D and 3D predictions for 0.2 ft/s injection velocity (full liquid loading; 1 jumper volume displaced)

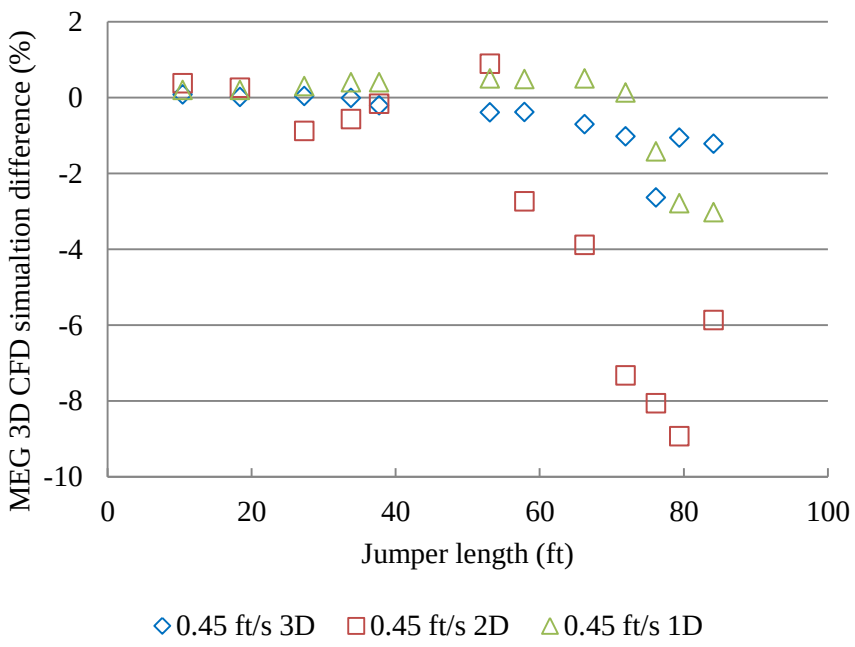

FIGURE 5 -23: DIFFERENCE IN INJECTION VELOCITY

Difference (%) associated to MEG 1D, 2D and 3D predictions for 0.45 ft/s injection velocity (full liquid loading; 1 jumper volume displaced)

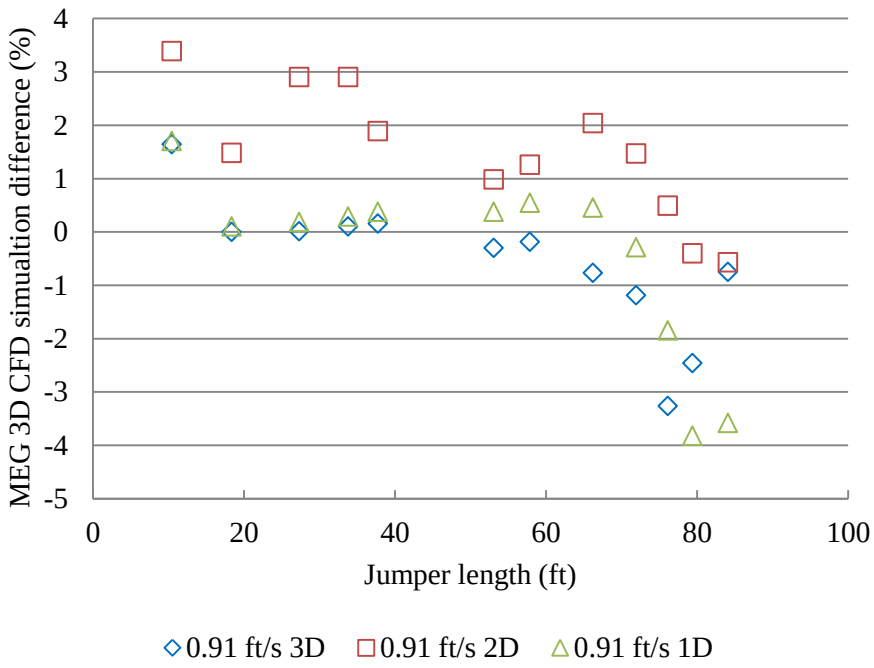

FIGURE 5 -24: DIFFERENCE IN INJECTION VELOCITY

Difference (%) associated to MEG 1D, 2D and 3D predictions for 0.91 ft/s injection velocity (full liquid loading; 1 jumper volume displaced)

5.4.2 Comparison among 1D, 2D, 3D simulations for methanol displacement tests

Figure 5-25 summarizes the comparisons among1D, 2D, and 3D simulated data to methanol experimental results for four injection rates. As can be seen from these plots, none of the simulation codes was able to successfully simulate methanol overriding the water phase at both low spots. The early dissipation of the stratified flow in the horizontal sections of the MeOH simulations suggested that there was too much dispersion in the simulations, relative to what occurs physically in the experiments. The excessive dispersion probably arose from the k-Ω turbulence model or from limitations imposed by discretization. For higher injection rate cases, the 2D and 3D CFD simulations were capable of predicting a relatively accurate methanol concentration profile. However, 3D CFD simulation has high requirement on the computational cost and time. Compared to the 2D CFD simulation results, only a small improvement in accuracy was gained.

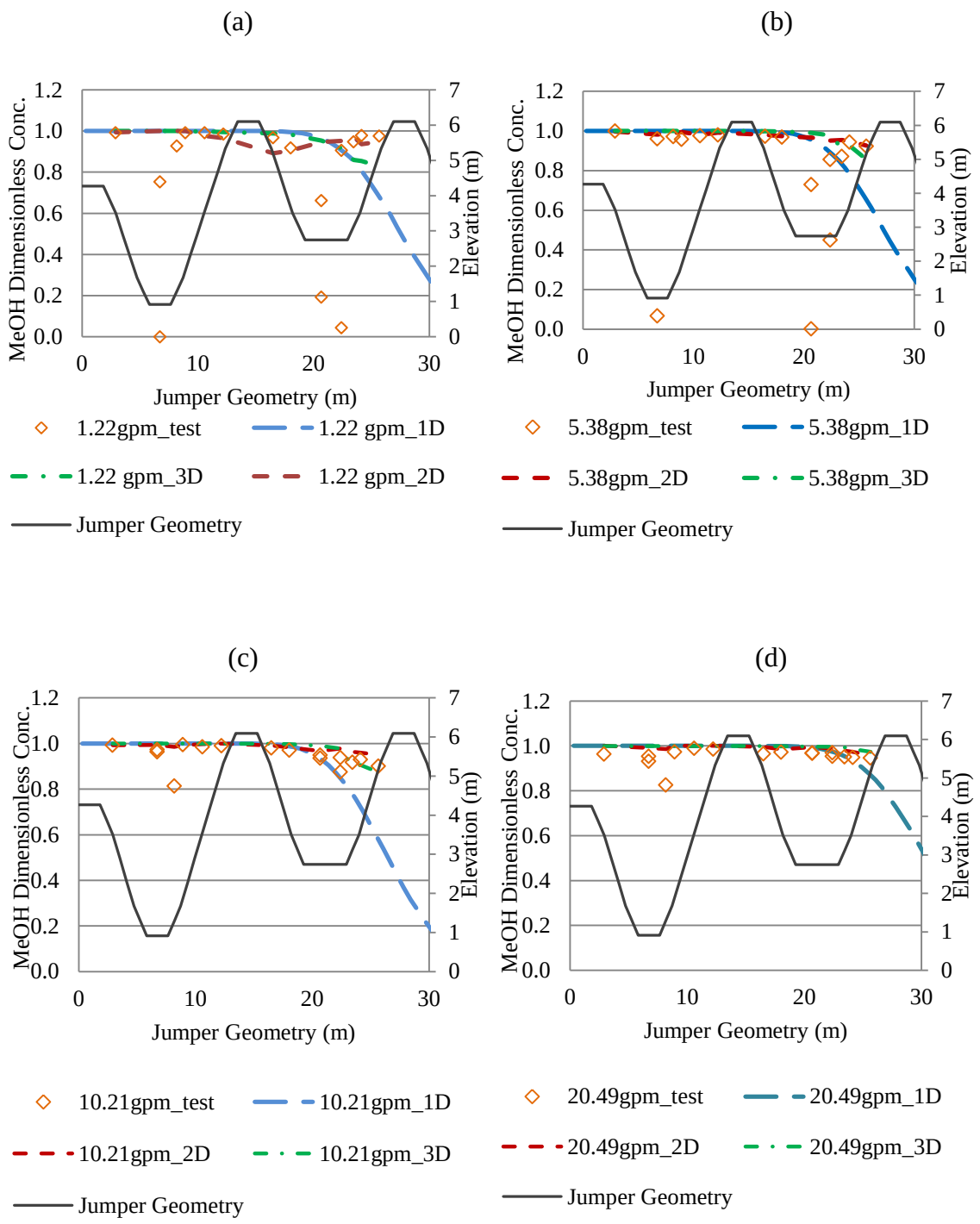

FIGURE 5 -25: COMPARISONS AMONG 1D, 2D AND 3D SIMULATIONS WITH METHANOL TESTS

CHAPTER 6: CONCLUSIONS AND RECOMMENDATIONS

6.1 Conclusions

Thermodynamic inhibitor (MEG or methanol) displacement tests in a three-inch jumper configuration to investigate the displacement and mixing patterns have been completed.

1) From the three-inch jumper tests, methanol was found to override the water phase in the horizontal low spots, leaving a large amount of water behind that could result in under-inhibited situations. Due to its lower density, methanol rises up the vertical sections faster than injected and provides effective inhibited results in the vertical sections even at low injection rates. By increasing the methanol injection rates, the mass fraction difference in the radial direction at horizontal low spots was significantly reduced and a nearly homogenous concentration was obtained in some cases. However, higher injection rates did not significantly improve the displaced water volume in the vertical sections of jumper.

2) For the 12 percent brine tests, less water was displaced for each MEG injection rate. Based on the knowledge gained from this study, the pump capacity is a critical variable that must be considered during the platform design. Since MEG has a greater viscosity than methanol, the frictional pressure loss in the jumper will be larger for MEG. However, MEG has greater density than methanol, and will thus have a larger static pressure contribution during the injection. For the 12 percent brine tests with methanol, a better mixing of methanol with brine was measured than in the MEG with 12 percent brine experiments; however, segregated methanol at the low spots was still observed during the experiments.

3) From the experimental studies on the three-inch jumper, it was shown that higher injection rates of MEG displace much more water from the jumper than the low injection rate tests. At low velocities (less than 0.15 m/s), MEG was observed to sink down the vertical sections faster

than it was injected because of its higher density. It also displaced the water from the bottom-up, out of the low spot. An inhibitor concentration profile was observed for injection velocities below 0.15 m/s; higher velocities were effective at displacing the water out of the jumper and resulted in more homogeneous concentrations throughout the jumper.

4) Conclusions can be drawn from the gas restart tests under different inhibited environments. Hydrates grow rapidly after nucleating at the cyclopentane - water interface. Slurry mass that formed in the elbow was permeable to gas, but not to liquid in the experiments. More hydrates formed in the elbow of first low spot. Cyclopentane hydrate formation experiments indicate that the prime location to form a plug was in the elbow right before (upstream of) the vertical riser section. The wall of the first riser was coated by a hydrate layer. Restarts at higher velocities displaced slush to the first high spot and second low spot. From the observation of the hydrates appearance, 12 percent MEG solution experiments had an ice-crystal appearance on top of the pipe wall, where the fresh water and 3.5 percent brine hydrate were slushy looking. Potential plugging risk at the second elbow was great because no inhibitor could reach it when both low spots were bridged with water upon restart.

5) The OLGA® 1D transient simulations for the methanol displacement tests show that the MEG tracking module is not capable of predicting methanol concentration profiles during THI injection operations for the jumper configuration system. Well displaced results given by OLGA simulations at both horizontal low spots in the radial direction are not consistent with the experimental measurements and observations. The assumption of methanol fully mixing with the water phase was proven not suitable for calculating light phase methanol displacing denser phase water scenarios. Lacking of a well-defined diffusion coefficient for the OLGA case setup may lead to failing to account for the physical mechanism effects on the methanol dispersing in the water phase. The mixing mechanism of methanol with water was not reflected by the 1D simulation,

which is more practical for long distance pipeline geometry in real offshore cases. The jumper facility is a more complicated configuration with two low spots and high spots, and it requires 2D or 3D finite element method based code to simulate desired situations.

6) Conclusions for the MEG OLGA simulations were drawn based on the comparison between experimental and simulated results. The performance of the OLGA MEG Tracking Module to estimate inhibitor concentration profiles along the jumper axial direction has been demonstrated to be unsatisfactory. Lack of proper determination of the physics for the plug flow mechanism at increasing injection rates, as well as the absence of diffusion on the dispersion process at low velocities, were the main reasons related to OLGA under-predictions for the MEG cases. Several OLGA simulations were conducted for repeated MEG displacement tests under the full water loading and one jumper volume injected condition. MEG dimensionless concentration profile predictions better matched: the main reason for the improved simulation results was attributed to the same injection flow rates input as the tests flow rates for these cases as the tests, as well as the same amount of running period corresponding to injection time during the jumper tests.

7) ANSYS FLUENT two-dimensional (2D) simulations were performed. The purpose of these simulations was to provide a comparison and clearer interpretation of the physics of methanol and MEG mixing with water. The results from the 2D simulations were compared with experimental results for the jumper with a full liquid loading and one jumper methanol injection displacement tests. Simulations were performed in the jumper configuration at the same test conditions in which the methanol was accounted for mixing, using the species transport model. The two most common two-equation turbulent models are the k-ε and k-Ω models, which were evaluated for the four methanol injection rates. The simulations using Star-CCM+ for purposes of a three-dimensional (3D) transient transport species two-fluid model was created in order to study the THI injection effectiveness in the jumper. The results from the two software programs were in

reasonable agreement, but neither could reproduce a consistent lasting stationary water phase in both low spots. Except in cases when the predicted methanol mass fraction at the horizontal low spots with methanol was injected, the results obtained by Star-CCM+ 3D were generally in better agreement with the results from the experiment. The difference in results between the solvers can be explained by different geometry, grid size, solver control, discretization techniques, and model set-up. In general, it is important to compare simulations between software packages to figure the best and also most economic numerical techniques to simulate the physics of the system.

6.2 Recommendations

For a future study of THI mixing and displacement mechanism in the subsea wellhead jumper configurations, displacement tests with low-viscosity oils should be performed with the objective of evaluating the effects of a non-polar / immiscible phase on the distribution of the THI on the aqueous phase. Due to the chemical structure of MEG and methanol, oil-THI emulsions might form causing under-inhibition of the system. In addition, if the selected oil is heavier than the THI (i.e., methanol) but lighter than the water, an interface of hydrocarbons might hinder the contact between the aqueous phase and the thermodynamic inhibitor. The configuration of the jumper design should be evaluated, and inclination angles of the low spots are highly suggested to be tested for this recommended future study. The methanol injection location is also one factor that can potentially be changed to improve the methanol injection effectiveness. For the future study, the amount of volatile methanol into the oil and gas phases should be considered. Methanol displacement tests involving live oil in the jumper under different water cuts should be conducted under both low and high pressure conditions.

For a future CFD simulation study, sensitivity analysis with respect to grid size should be conducted to evaluate the effect of the aspect ratio on the prediction of the concentration profile of the THI along the jumper. A finer mesh will allow capture of further interface details between the methanol and water during the displacement operations. A scale-up study of a jumper that includes different pipe diameters (e.g., 6, 8, and 10 inches), to determine the effects of jumper length versus diameter ratios, is suggested to be conducted. The purpose of this study will be to ensure that the models evaluated during the academic study behave realistically under the non-isothermal, high pressure conditions encountered in subsea environments.

REFERENCES

1. Balakin, B.V., Hoffmann, A.C., K. P., "Turbulent flow of hydrates in a pipeline of complex configuration," ***Chemical engineering science***, pp.5007-5017, 2010.
2. Brustad, S., Loken, K.-P.; Waalman, J. G., "Hydrate Prevention using MEG instead of MeOH: Impact of experience from major Norwegian developments on technology selection for injection and recovery of MEG,"," *Paper presented at the 2005 Offshore Technology Conference*, pp. 1-5, OTC 17355, 2005.
3. Cagney, T., Hare, S., "Hydrate Inhibition of Subsea During Shut-in,"," *Paper presented at the 2006 SPE Annual Technical Conference and Exhibition*, SPE 102330, pp. 1-11, 2006.
4. Cochran, S., "Hydrate control and remediation best practices in deepwater oil developments," *Paper presented at 2003 Offshore Technology Conference*, OTC 15255-MS, 2003.
5. Coletta, A., "Investigation of Flow Behavior in Well Head Jumpers during Restart with Gas and Liquid," *M.S.E Thesis, The University of Tulsa.* United States of America, 2009.
6. Desselles, R.P., Harper, J.D., "Offshore oil and gas supply," Offshore supply subgroup of the resource & supply task group, 2011.
7. Ellison, B.T., Gallagher, C.T., "The physical chemistry of wax, hydrates, and asphaltene," *Paper presented at the 2000 Offshore Technology Conference*, OTC 11963-MS, 2000.
8. Estanga, D., "Plugging Tendencies of Hydrate Forming Systems During Restart Operations," *M.S.E Thesis, The University of Tulsa.* United States of America, 2007.
9. Esaklul, K. A.; Fung, G., "Active heating for flow assurance control in deepwater flowlines," *Paper presented at the 2003 Offshore Technology Conference*, OTC 15188-MS, 2003.
10. Fatnes, E. D., "Numerical simulations of the flow and plugging behavior of hydrate particles," *M.Sc. Thesis, University of Bergen, Norway*, 2010.
11. Fluent Inc., "Tutorial 13. Modeling Species Transport and Gaseous Combustion," pp. 1-48, 2006. *Available at: my.fit.edu/itresources/manuals/fluent6.3/help/pdf/tg/tut13 .pdf.*

12. Hammerschmidt, E.G., *Ind. Eng. Chem.*, 1934.

13. Herrman, B., Bargas, C., Buckingham, J. C., "Hydrate Inhibition in Headers With No Production Flow," *Paper presented at the 2004 SPE Annual Technical Conference and Exhibition*, SPE 90127, pp. 1-9, 2004.

14. Hubbard, R.A., "Recent developments in gas dehydration and hydrate inhibition," John M. Campbell and Co., SPE 21507-MS, 1991.

15. Jassim, E., Abdi, M. A., Muzychka, Y., "A CFD-based model to locate flow restriction induced hydrate deposition in pipelines," *Paper presented at the 2008 Offshore Technology Conference*, OTC 19190, 2008.

16. Jassim, E., Abdi, M.A., Muzychka, Y., "A new approach to investigate hydrate deposition in gas-dominated flowlines," Journal of natural gas science and engineering, pp. 163-177, 2010.

17. Katz, D.L., Cornell, D., Kobayashi, R., Poettmann, F.H., Vary, J.A., Elenbaas, J.R., Weinaug, C.F., ***Handbook of Natural Gas Engineering***, McGraw-Hill, New York, pp. 802, 1959.

18. Kelland, M. A., Svartaas, T. M., "A new generation of gas hydrates inhibitors," *Paper presented at the SPE Annual Technical Conference and Exhibition*, SPE 30695-MS, 1995.

19. Leporcher, E.; Kinnari, K.; Labes-Carrier, C.; Maurel, P.; Vandersippe, W., "Multiphase Flow: Can we take advantage of hydrodynamic conditions to avoid hydrate plugging during deepwater restart operations," *Paper presented at the 2002 SPE Annual Technical Conference and Exhibition*, SPE 77647, pp. 1-9, 2002.

20. Lide, D.R., ***CRC Handbook of Chemistry and Physics***, 77th edition, CRC press, pp. 8-65, 1996.

21. Lovell, D.; Pakulski, M., "Hydrate inhibition in gas wells treated with two low dosage hydrate inhibitors," SPE Gas Technology Symposium, SPE 75668-MS, 2002.

22. Makogon, Y. F., ***Hydrates of Natural Gas***, *PennWell Books*, Tulsa, Oklahoma, United States of America, 1981.

23. Mehta, A., Walsh, J., Lorimer, S., "Hydrate Challenges in Deep Water Production and Operation," *Annals of the New York Academy of Sciences*, v 912, Gas Hydrates: Challenges for the Future, pp. 366-373, 2000.

24. Mele, S., "Experimental and computational investigation on the displacement and mixing mechanisms in well-head jumpers during restart with monoethylene glycol," *M.S.E Thesis, The University of Tulsa.* United States of America, 2009.

25. Mokhatab, S., Wilkens, R. J., Leontaritis, K. J., "A Review of Strategies for Solving Gas-Hydrate Problems in Subsea Pipelines,"," ***Energy Sources***, Part A, v 29, n 39-45, pp. 39-47, 2007.

26. Paez, J. E.; Block, R., "Problems in gas hydrates: practical guidelines for field remediation," *paper presented at SPE Latin American and Caribbean Petroleum Engineering Conference*, SPE 69424-MS, 2001.

27. Rensing, P. J., Koh, C. A., Sloan, E. D., "Simulation of hydrate aggregate structure via the discrete element method," *Paper presented at the 6th International Conference on Gas Hydrates*, Calgary, Alberta, Canada, 2008.

28. ScandPower Petroleum Technology, "OLGA User Manual Version 5". Norway, 2008.

29. Sean. W. Y., Sato, T., "CFD and experimental study on methane hydrate dissociation Part 1. Dissociation under water flow," American Institute of Chemical Engineers, Vol. 53, No.1, 2006.

30. Sloan, E. D., Bloys, J. B., "Hydrate Engineering," *SPE Monograph: Society of Petroleum Engineers Inc.* United States of America, 2000.

31. Sloan, E. D., Koh, C. A., ***Clathrate Hydrates of Natural Gas***, *CRC Press*, 3rd Edition. United States of America, 2008.

APPENDIX A

COMPARISONS BETWEEN MEG AND METHANOL WITH FULL FRESH WATER LOADING JUMPER TEST RESUTLS

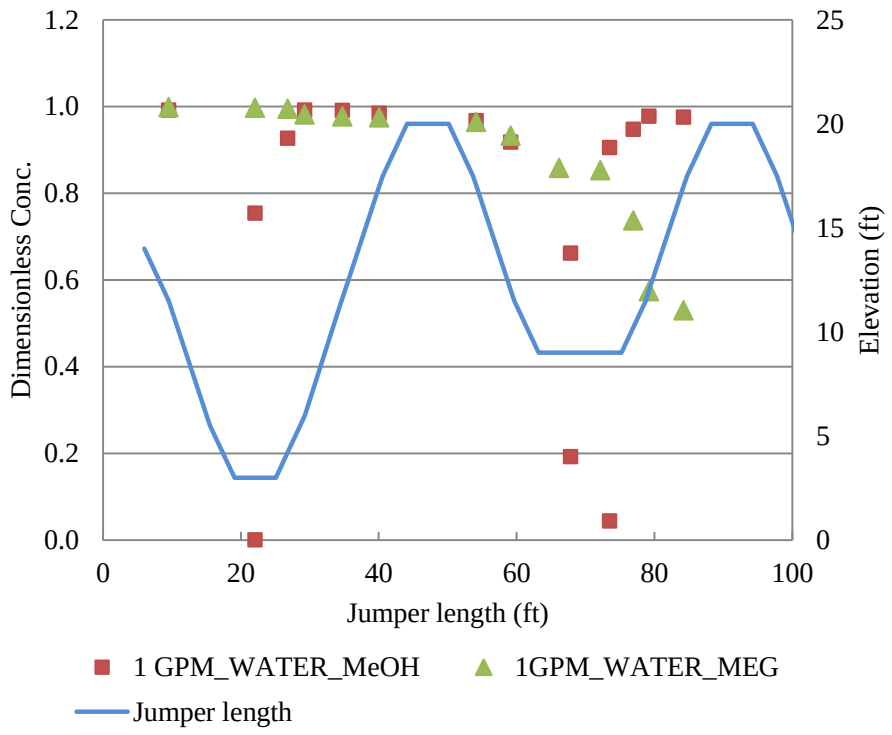

FIGURE A - 1: COMPARISON RESULTS – MEG AND METHANOL AT 1 GPM

Comparison between MEG and methanol at 1 gpm injection rate test results from full fresh water loading, one jumper volume displaced tests

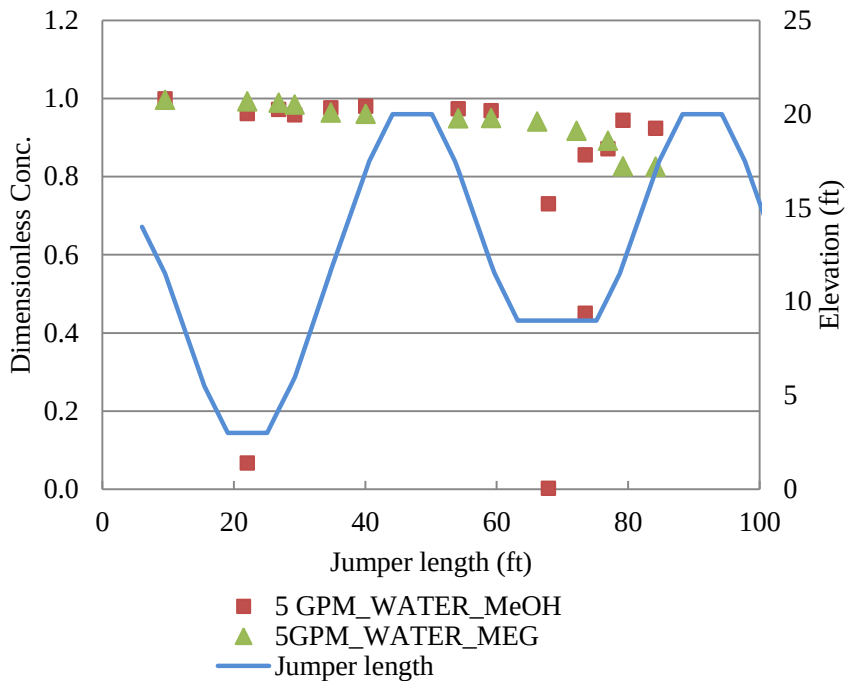

FIGURE A - 2: COMPARISON RESULTS – MEG AND METHANOL AT 5 GPM

Comparison between MEG and methanol at 5 gpm injection rate test results from full fresh water loading, one jumper volume displaced tests

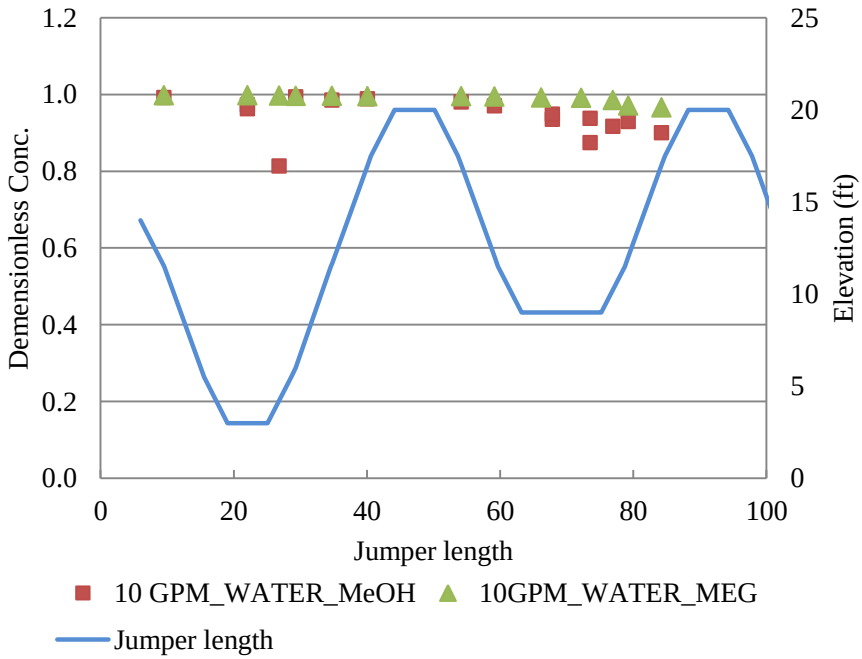

FIGURE A - 3: COMPARISON RESULTS – MEG AND METHANOL AT 10 GPM

Comparison between MEG and methanol at 10 gpm injection rate test results from full fresh water loading, one jumper volume displaced tests

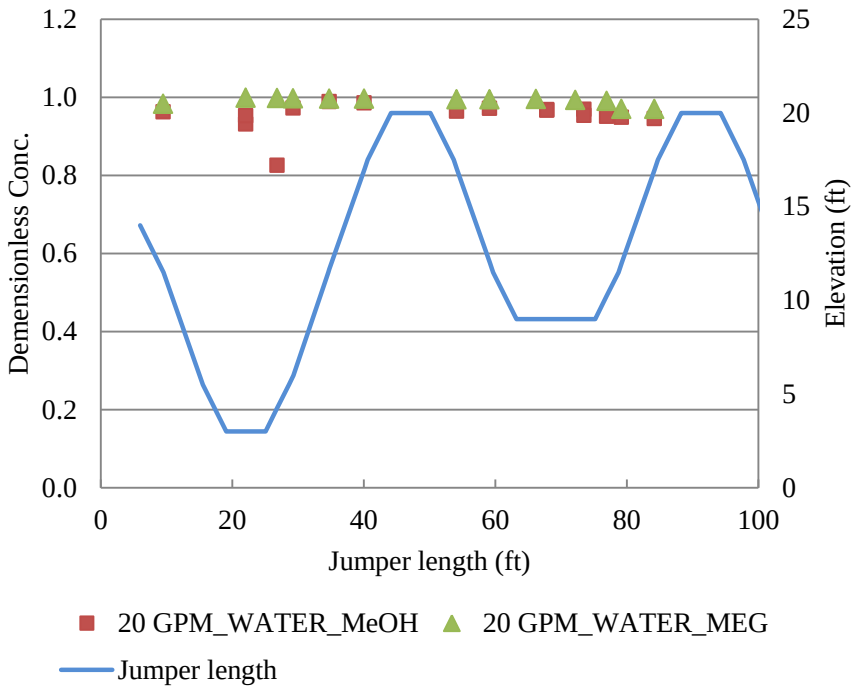

FIGURE A - 4: COMPARISON RESULTS – MEG AND METHANOL AT 20 GPM

Comparison between MEG and methanol at 20 gpm injection rate test results from full fresh water loading, one jumper volume displaced tests

APPENDIX B

COMPARISONS BETWEEN MEG AND METHANOL WITH FULL 12% BRINE LOADING JUMPER TEST RESUTLS

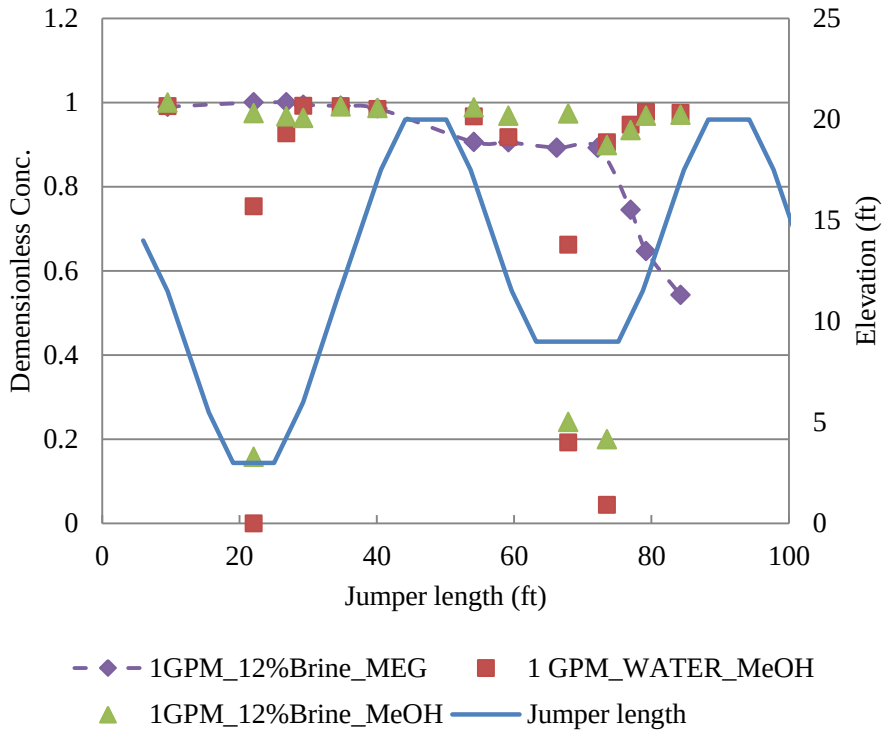

FIGURE B - 1: COMPARISON RESULTS – 1 GPM

Comparison between MEG and methanol at 1 gpm injection rate test results from full 12% brine loading, one jumper volume displaced tests

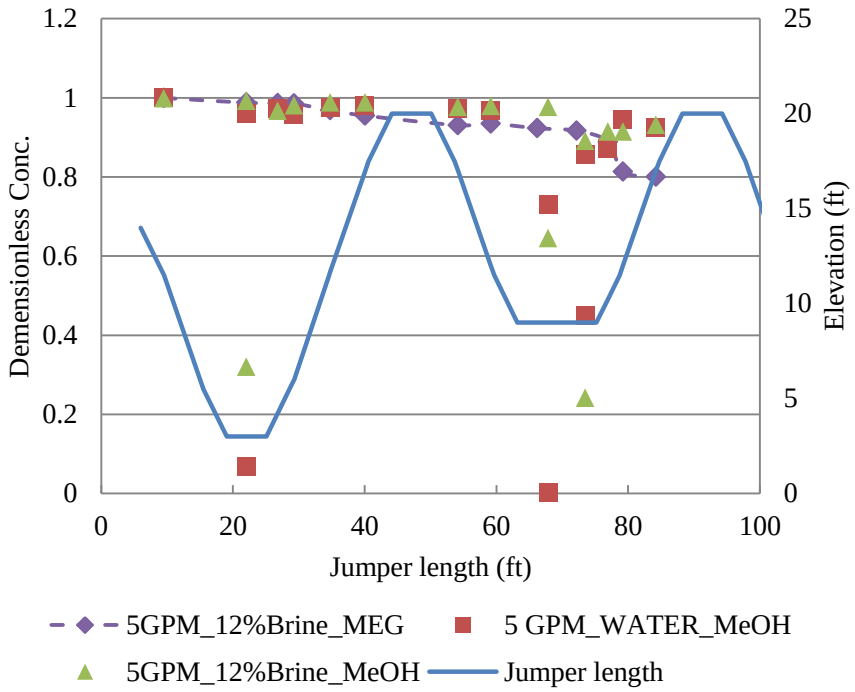

FIGURE B - 2: COMPARISON RESULTS – 5 GPM

Comparison between MEG and methanol at 5 gpm injection rate test results from full 12% brine loading, one jumper volume displaced tests

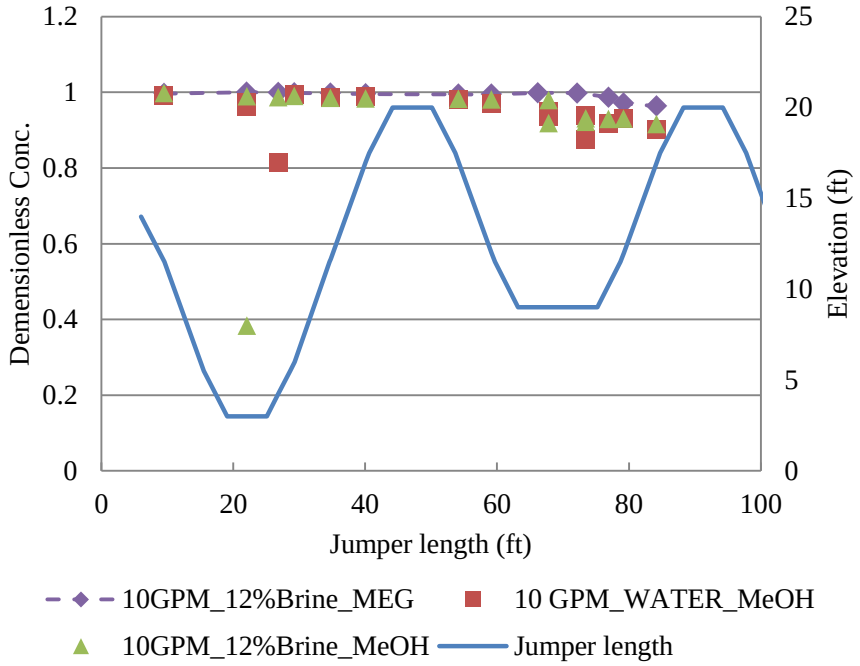

FIGURE B - 3: COMPARISON RESULTS – 10 GPM

Comparison between MEG and methanol at 10 gpm injection rate test results from full 12% brine loading, one jumper volume displaced tests

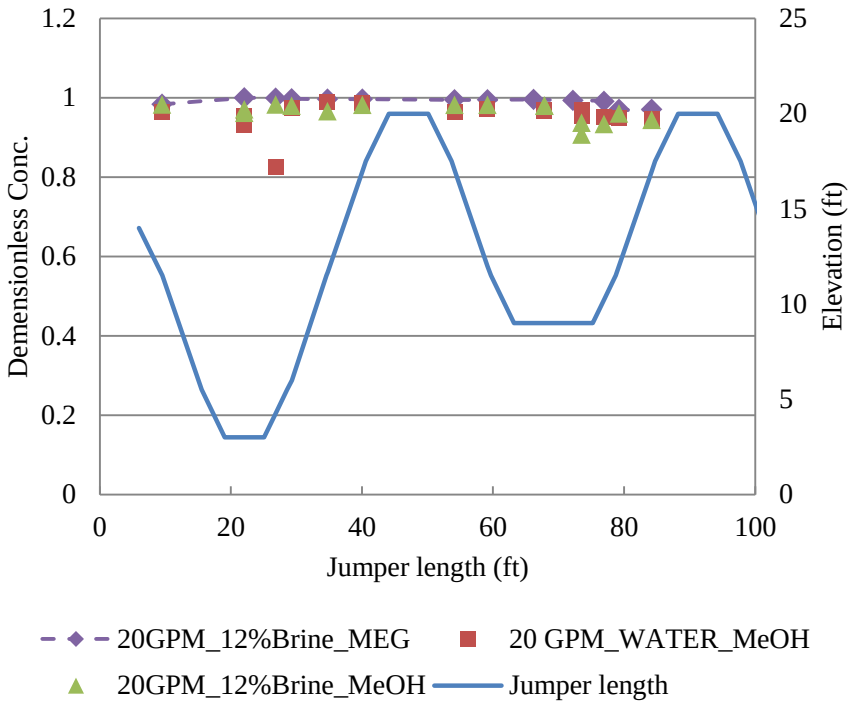

FIGURE B - 4: COMPARISON RESULTS – 20 GPM

Comparison between MEG and methanol at 20 gpm injection rate test results from full 12% brine loading, one jumper volume displaced tests

APPENDIX C

P&ID OF JUMPER FACILITY

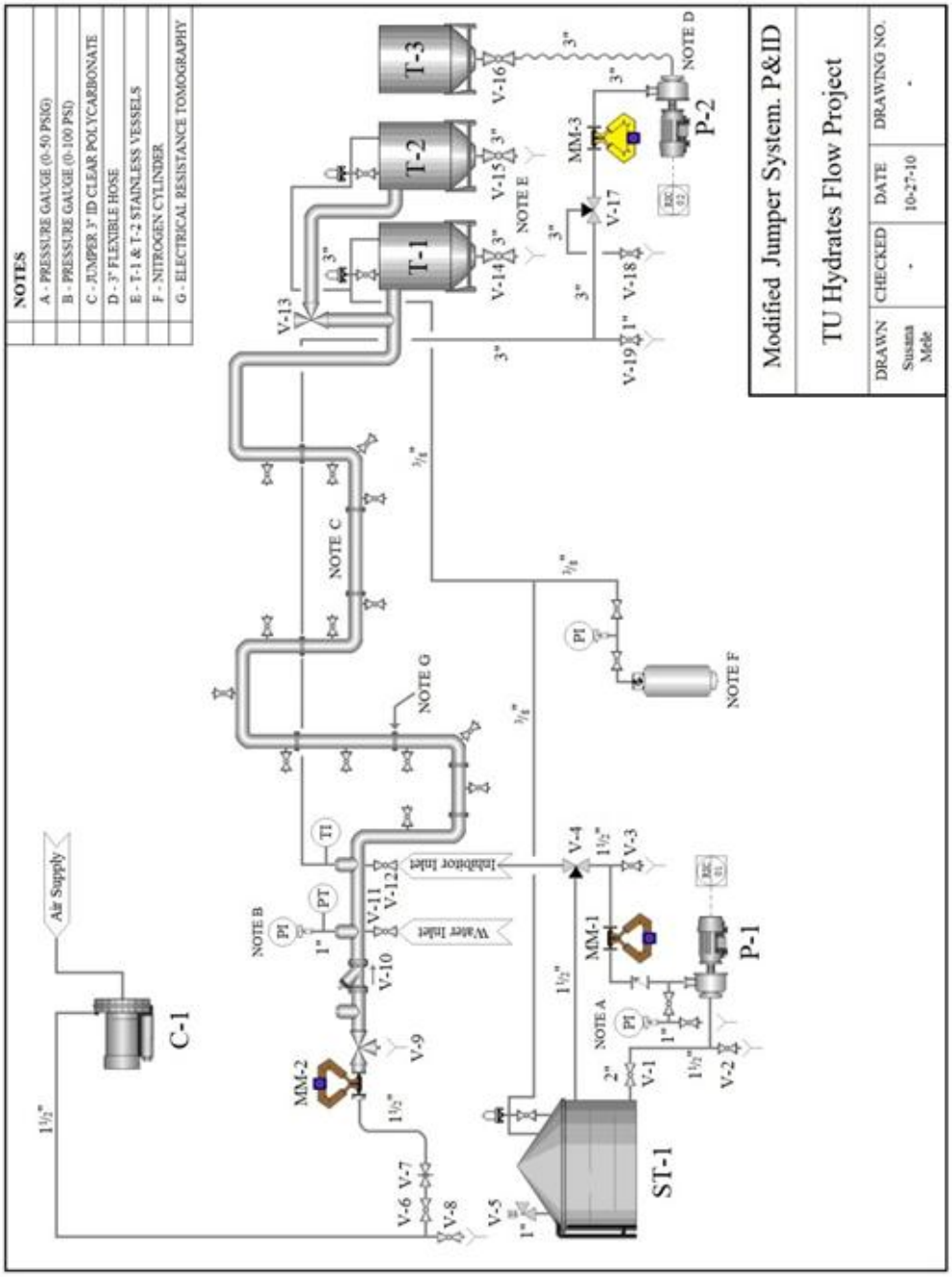

APPENDIX D

THI jumper displacement tests injection flow rate converting to injection velocity

For MEG tests,

gpm	ft/s
0.74	0.02
1	0.05
4.84	0.19
5	0.2
9.97	0.45
10	0.45
20	0.91
20.35	0.92

For methanol tests,

gpm	ft/s
1	0.05
1.22	0.051
5	0.2
5.38	0.24
10	0.45
10.21	0.46
20	0.91
20.49	0.93

APPENDIX E

A prior CFD model had been set up by CD-Adapco and tested against experimental data corresponding to gas restart cases. The good agreement between the gas restart simulations and experimental results led us to believe that Star-CCM+, a CFD package, could accurately simulate injecting THI into jumpers fully loaded with liquid.

The gas-restart model required several modifications prior to use for THI injection simulations. The gas-restart simulation used a two-phase VOF method to capture the interface between the gas and the liquid without requiring an exceedingly fine mesh that explicitly resolved interfacial gradients. Simulating THI injection calls for a multicomponent fluid model, rather than for a multiphase model, because the THIs (MEG and MeOH) of interest are miscible with the water loaded in the jumper. Naturally, the fluid properties also needed updating for the new fluids and were a function of THI mass fraction. Water - MEG solution properties were taken from manufacturer data (Ethylene glycol product guide, 001-00005-0508-CRCG © 2008 The MEGlobal Group of Companies) and literature (J. Fernandez-Sempre, F. Ruiz-Bevia, J. Colom-Valiente, and F. Mas-Perez. Determination of Diffusion Coefficients of Glycols. ***J. Chem. Eng. Data*** 1996, 41, 47-48. Charles H. Byers and C. Judson King. Liquid Diffusivities in the Glycol-Water System. ***J. Phys. Chem.*** 1966, 70, 2499-2503. G. Ternström, A. Sjöstrand, G. Aly, and Å. Jernqvist. Mutual Diffusion Coefficients of Water + Ethylene Glycol and Water + Glycerol Mixtures. ***J. Chem. Eng. Data*** 1996, 41, 876-879.). The water - MeOH solution properties were found in the ***CRC Handbook of Chemistry and Physics*** (David R. Lide, ed. 77th edition, CRC Press 1996, p. 8-65) and a paper by Derlacki et al. (Z.J. Derlacki, A.J. Easteal, A.V.J. Edge, and L.A. Woolf. Diffusion Coefficients of Methanol and Water and the Mutual Diffusion Coefficient in Methanol-Water Solutions at 278 and 298 K. ***J. Phys. Chem.*** 1985, 89, 5318-5322.). The density difference

between the water and the two THIs of interest suggested that buoyancy would play a role in flow, particularly at lower flow rates, so the effect of gravity was included in the model. The buoyancy effects in the jumper risers and downcomers could manifest as a waving, swirling, turbulent flow, so the model setup used Reynolds-Averaged Navier-Stokes equations with the SST k-Ω turbulence model and an all y+ wall treatment.

The simulations were performed using Star-CCM+ version 7.02.011. In Star-CCM+, as well as other CFD packages, the spacial and temporal domains over which the governing equations and boundary conditions are solved must each be discretized, or divided into discrete segments that span the entire domain. The spacial domain is partitioned into a collection of polyhedral cells called a mesh, as shown in

Figure E - **1**. The temporal domain of the problem is subdivided into a series of time steps.

Figure E - **2** illustrates how the accuracy of the solution increases as the number of cells increases, up to the point where other limitations, such as the time step size or solver tolerances, govern the accuracy of the solution. The computational cost of the solution also increases with the cell count. Just as accuracy increases with cell count, it increases with decreasing time step size, as seen in Figure E - 3, until a point at which other inaccuracies govern the solution. It can also be seen in Figures E - 2 and E - 3 that further increasing the cell count and decreasing the time step size will yield negligible improvements in accuracy at substantially greater computational cost.

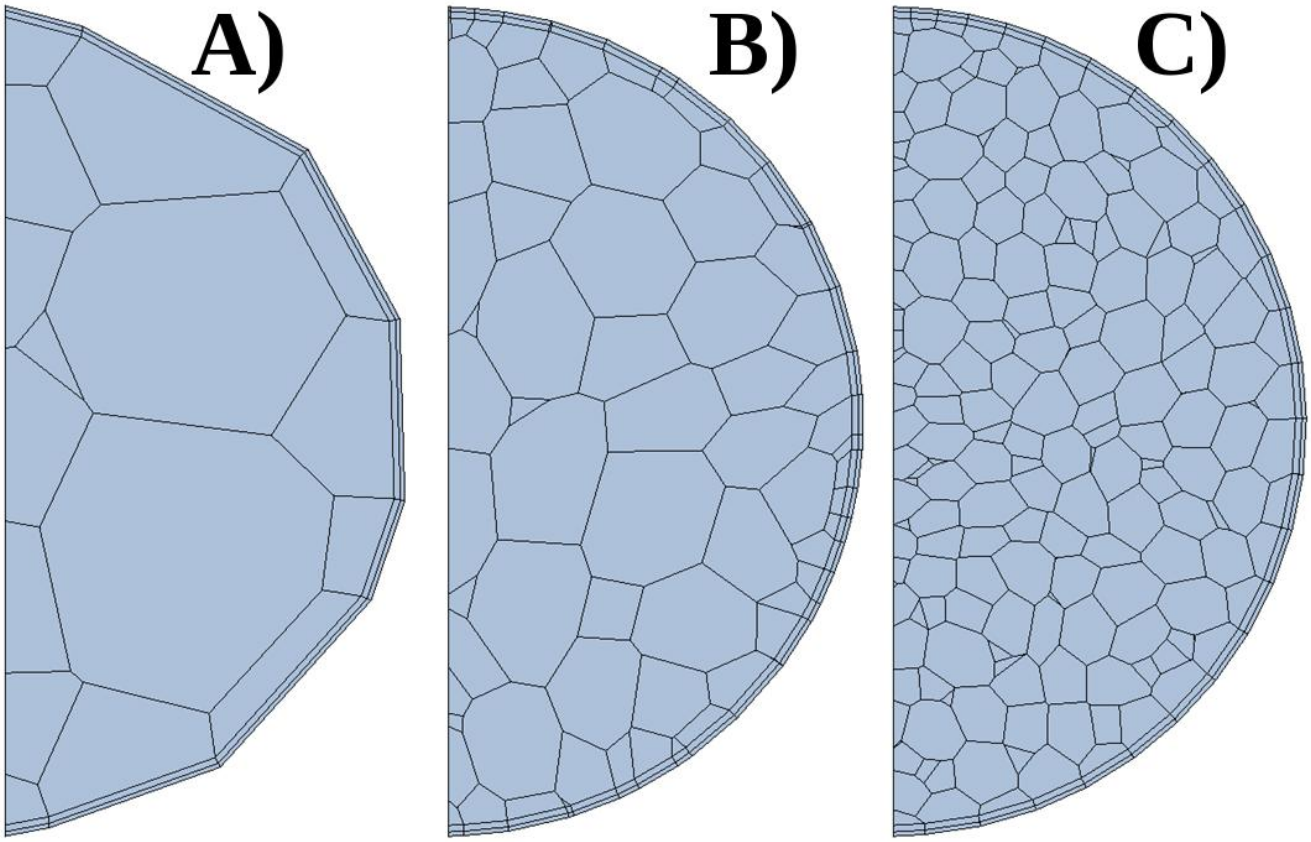

FIGURE E - 1 - SYMMETRIC CROSS SECTIONS OF THE JUMPER

Discretized into meshes with different sizes and numbers of cells.
The cross section A) came from the jumper discretized into 64,000 cells, B) 935,000 cells, and C) 1,900,000 cells.

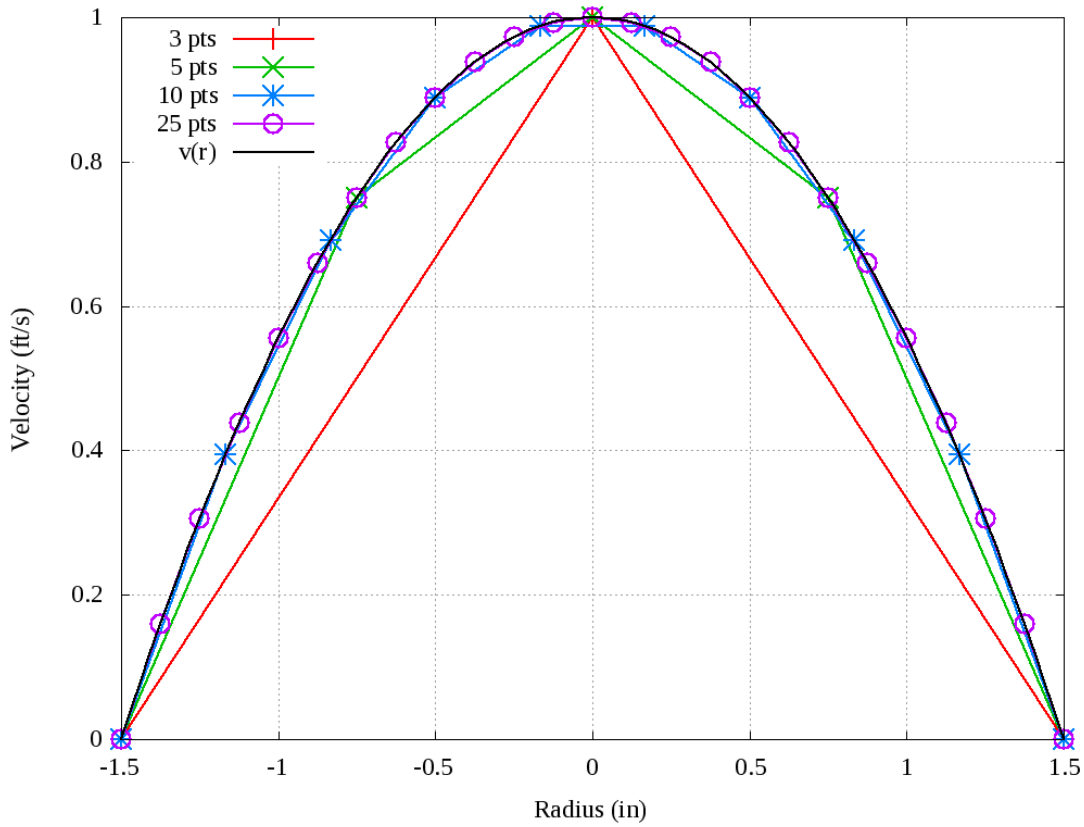

FIGURE E - 2 - DISCRETIZING THE JUMPER

Discretizing the jumper into smaller, more numerous cells increased the accuracy of the velocity profile.

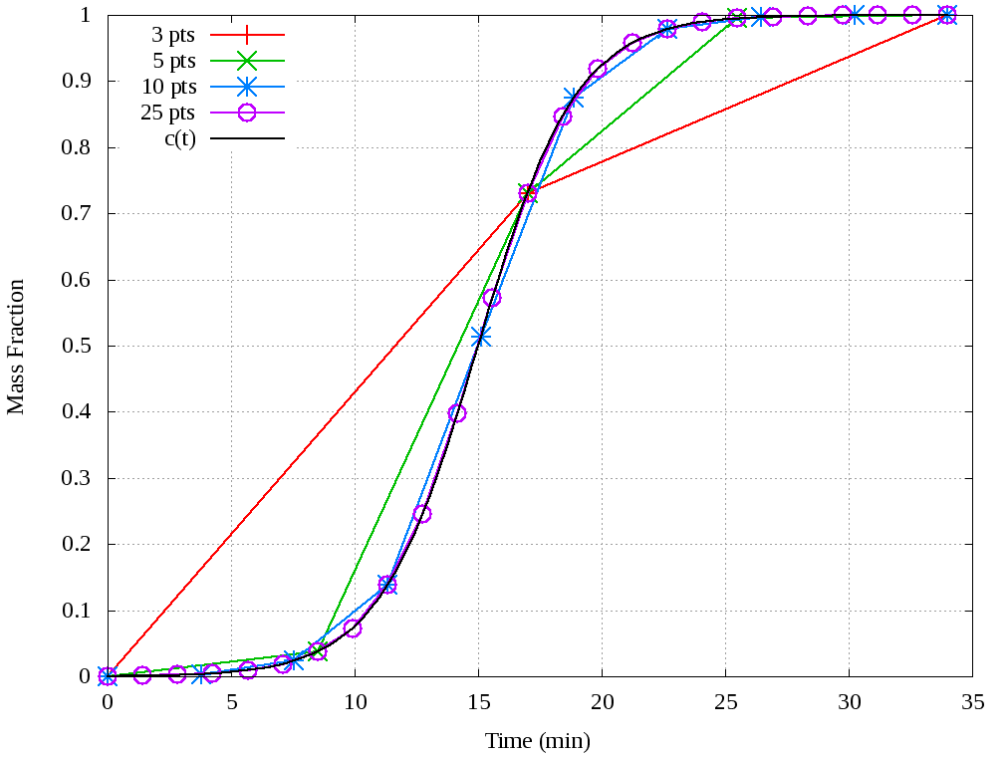

FIGURE E - 3 - INCREASING THE NUMBER OF TIME STEPS INCREASES THE TEMPORAL ACCURACY OF THE SOLUTION IN THE JUMPER

The mesh used in the gas-restart simulations required rebuilding because the jumper dimensions had changed due to various repairs and improvements being made after the gas-restart experiments. The changed mesh and models required a new round of verification studies to make sure the mesh and time step size do not limit the accuracy of the solution. The verification process tested a matrix of meshes and time steps to minimize the error due to mesh size and time step size, while ensuring that the final solution required minimal computational effort.

Seven meshes were built with cell counts from 64K up to 1,900K cells. Time step sizes from 0.5 to 0.025 s were tested on the best meshes. In each simulation the MEG mass fraction was monitored at the first five sample ports shown in Figure E - 4 during a simulation of 600 s flowing 1 gpm 80 percent MEG in water into a jumper loaded with water. The time steps were at 1 s intervals with 20 iterations per time step.

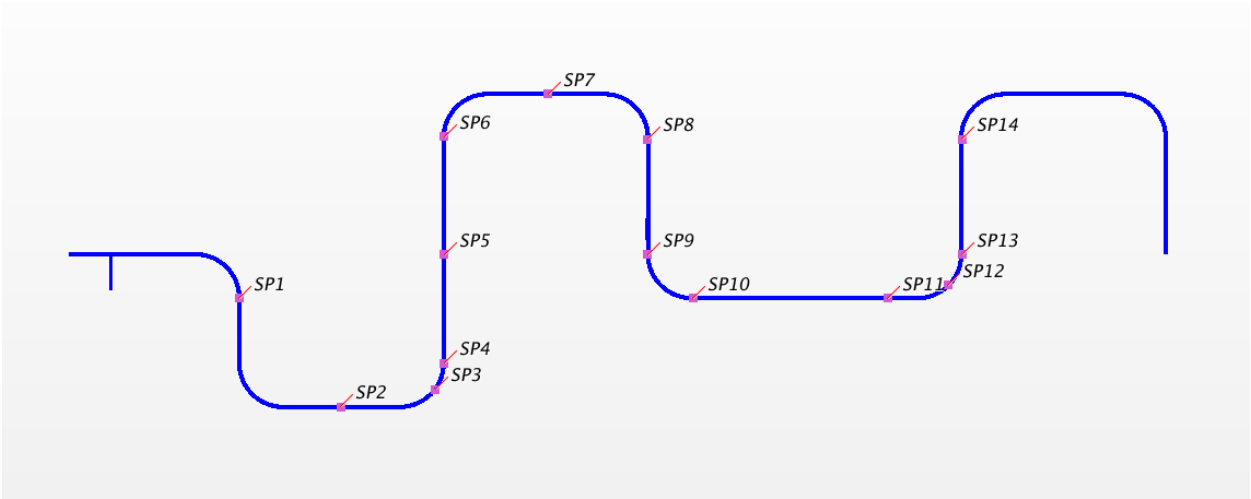

FIGURE E - 4. – CONCENTRATION IN JUMPER

Concentration in the jumper simulations was monitored at 14 points corresponding with the experimental sample collection points.

Figure E - **5**, the mass fraction plot at sample point 1, shows that the solutions on the two coarsest meshes (64K and 105K cells) differed markedly from the others in their behavior, particularly when the mass fraction is less than 0.1. The meshes for 494K, 935K, and 1,900K cells have very similar solutions at all five points (results not shown), exemplifying the expected behavior of the solution converging as the cell count increases. To further examine the effect of mesh size required minimizing the inaccuracies in the simulations due to the time step size.

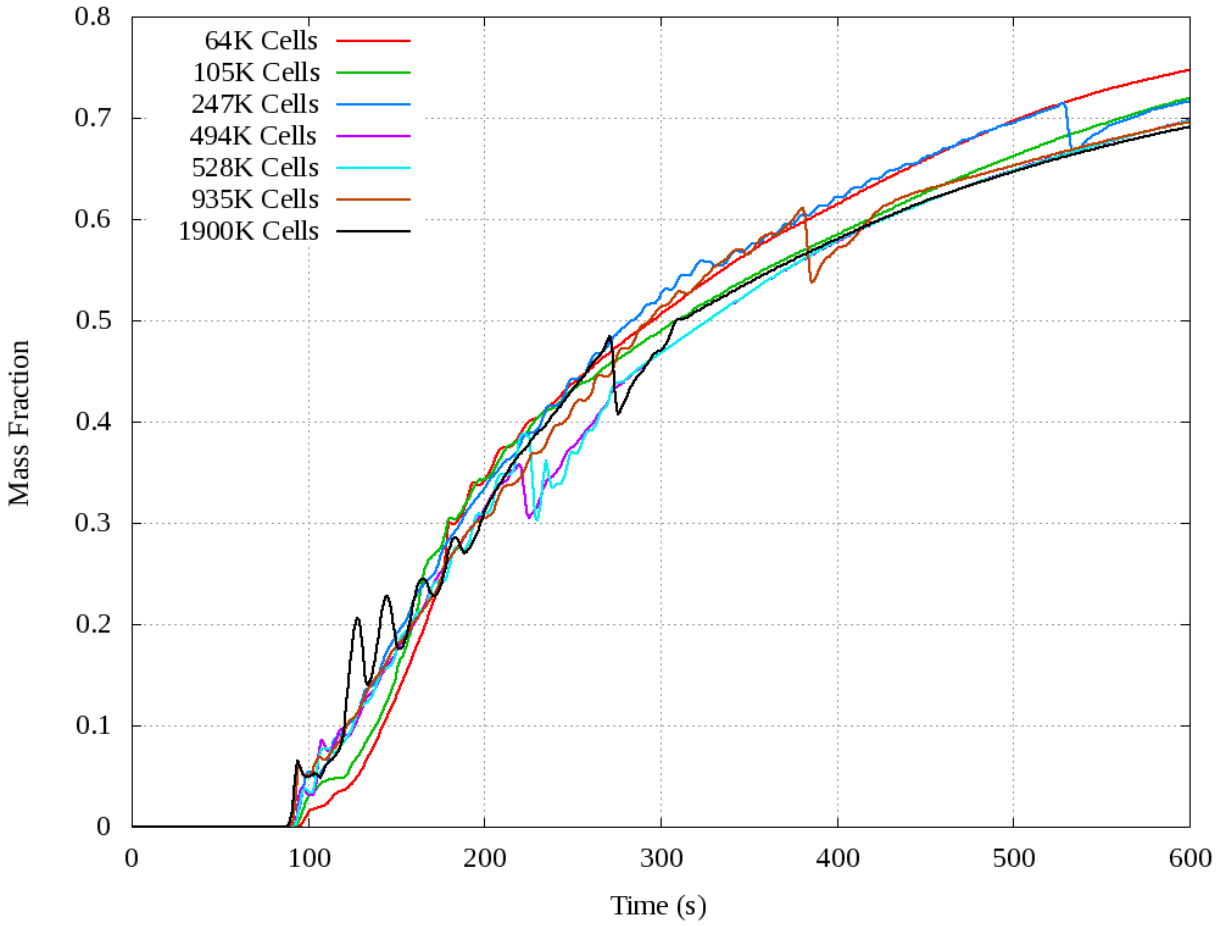

FIGURE E - 5 – SIMULATION RESULTS AT SAMPLE POINT 1

The 3 smallest meshes are producing different results from the other 4 meshes at 600 s.

To verify the time step independence of the solutions for the 494K, 935K, and 1,900K cell meshes, the time step was set to the largest value for which convergence could be achieved using five iterations per time step. Then the time step was decreased and the problem solved again until the most recent solution matched the one prior to it. At this point, the solution was considered 'time step independent'. The penultimate time step should be used in further simulations, since the last time step did not appreciably alter the solution but did take twice as long to compute.

Simulating 10 minutes of the jumper displacement process took 81 hours on 24 CPUs (Xeon X5550 @ 2.67GHz) using the 1,900K cell mesh, 54 hours on 16 CPUs with the 935K cell mesh,

and 23.7 hours on 8 CPUs with the 494K cell mesh. The 494K cell simulations used time steps of 0.5, 0.25, 0.1, and 0.05 s. The 935K cell simulations used time steps of 0.25, 0.1, 0.05, and 0.025 s. The 1,900K cell simulations used time steps of 0.1, 0.05, and 0.025 s. In each case the last two time steps had highly similar results. The results in

Figure E - **6** from the 935K cell mesh at sample point 1 demonstrate this convergence and are illustrative of the results for the other two meshes as well.

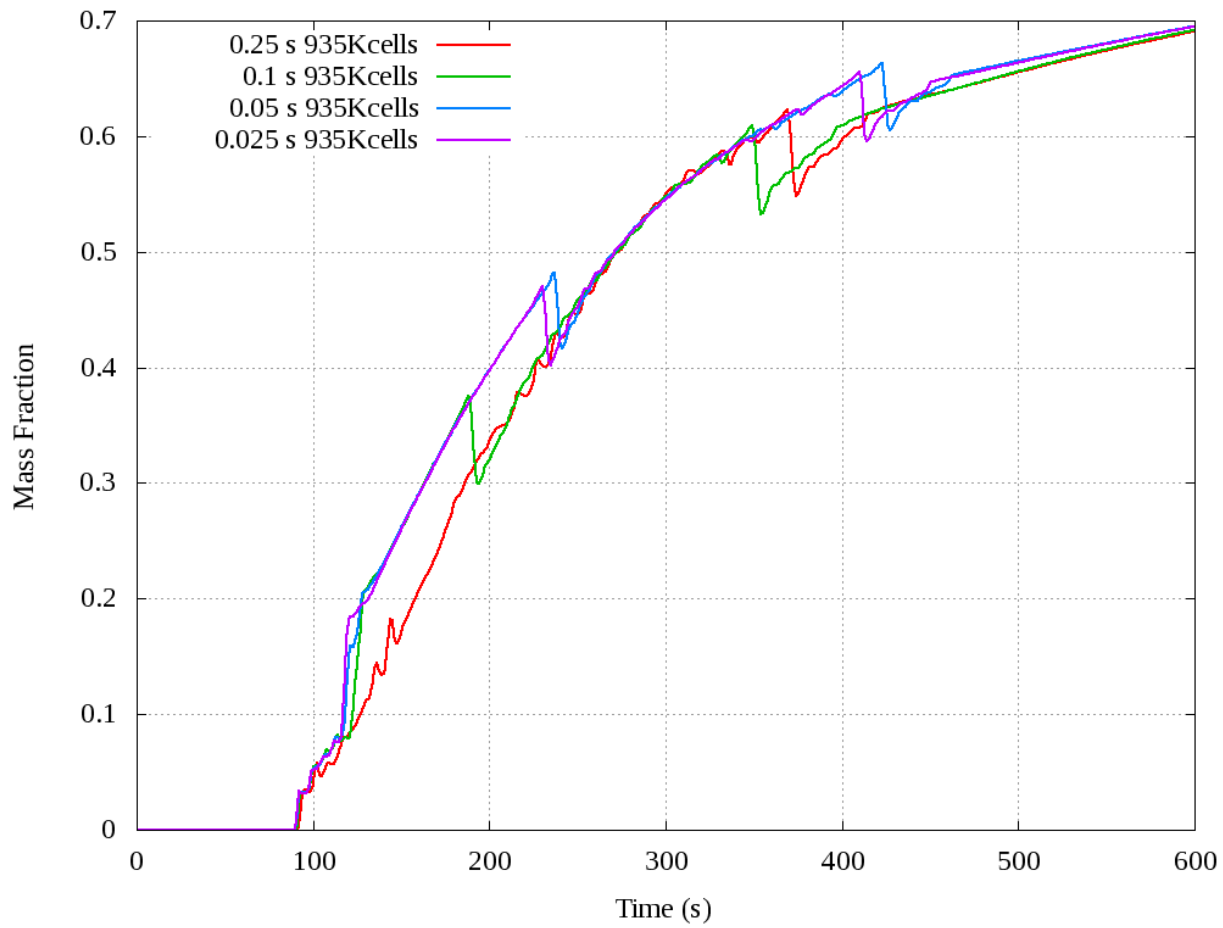

FIGURE E - 6 – SAMPLE RESULTS

Decreasing the time step for the simulation on the 935K cell mesh increased the solution accuracy. This result is typical of the results for the 494K and 1900K cell meshes.

The time step independent solutions on the 494K, 935K, and 1,900K meshes were compared to one another at each of the five sample points. Two of the five resulting mass fraction vs. time profiles are shown below in

Figure E - **7** and

Figure E - **8**. At sample point 1 the three solutions converged to the same value at 600 s. The sharp decline and subsequent rise in concentration shown in the solutions between 200 and 450 s is a noteworthy difference between the simulations. These rapid concentration changes in the jumper's first downcomer were caused by the side-to-side motion of the heavy MEG rich fluid falling down past a stream of rising, lower density water. The concentration at sample point 1 increased slowest on the 494K cell mesh, while the 935K and 1,900K cell solutions developed more similarly to one another.

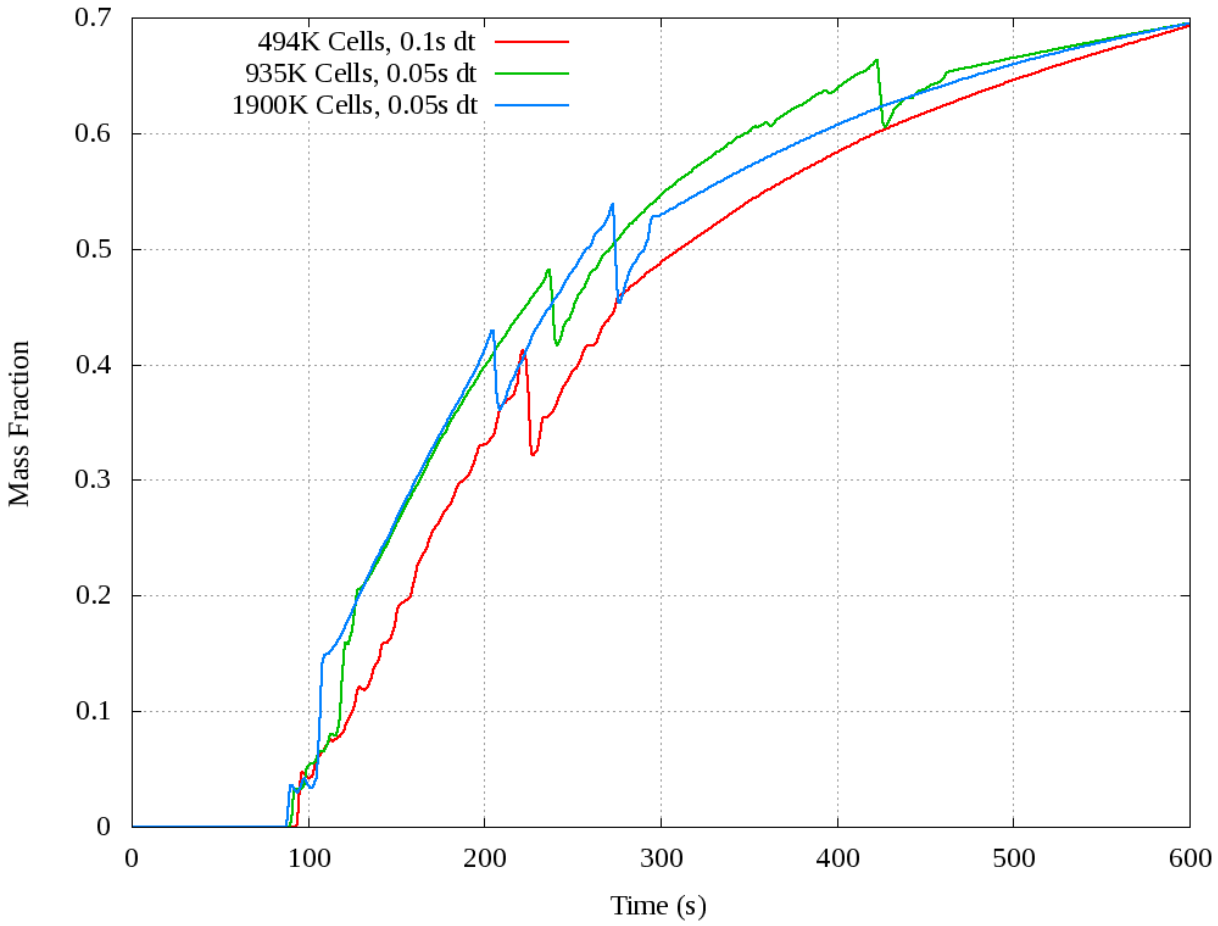

FIGURE E - 7 – SAMPLE RESULTS

Sample point 1 in the jumper's first downcomer.
The three solutions approach the same end point, but have different transient responses.

Sample point 3 in the elbow just after the first low section of the jumper showed the same trend, with the 494K cell solution differing from the higher cell meshes and the 935K cell solution approaching the 1,900K cell solution. The plots of the solutions at sample points 2, 4, and 5 showed similar behavior. These results show that the 1,900K cell mesh is the most accurate of those tested and produces a markedly different solution from the 935K cell mesh in terms predicting the transient fluid behavior in the downcomer. It is probable that halving the cell size again, thereby doubling the mesh size, will yield an improved solution. However, this action will also increase the simulation run time to complete a full jumper displacement from approximately 11.5 days using the 1,900K cell mesh to over 23 days. The results from the 1900K and 935K cells are already so similar that it is doubtful the small improvement in accuracy gained by using a 4000K cell mesh will be worth the doubled computational cost.

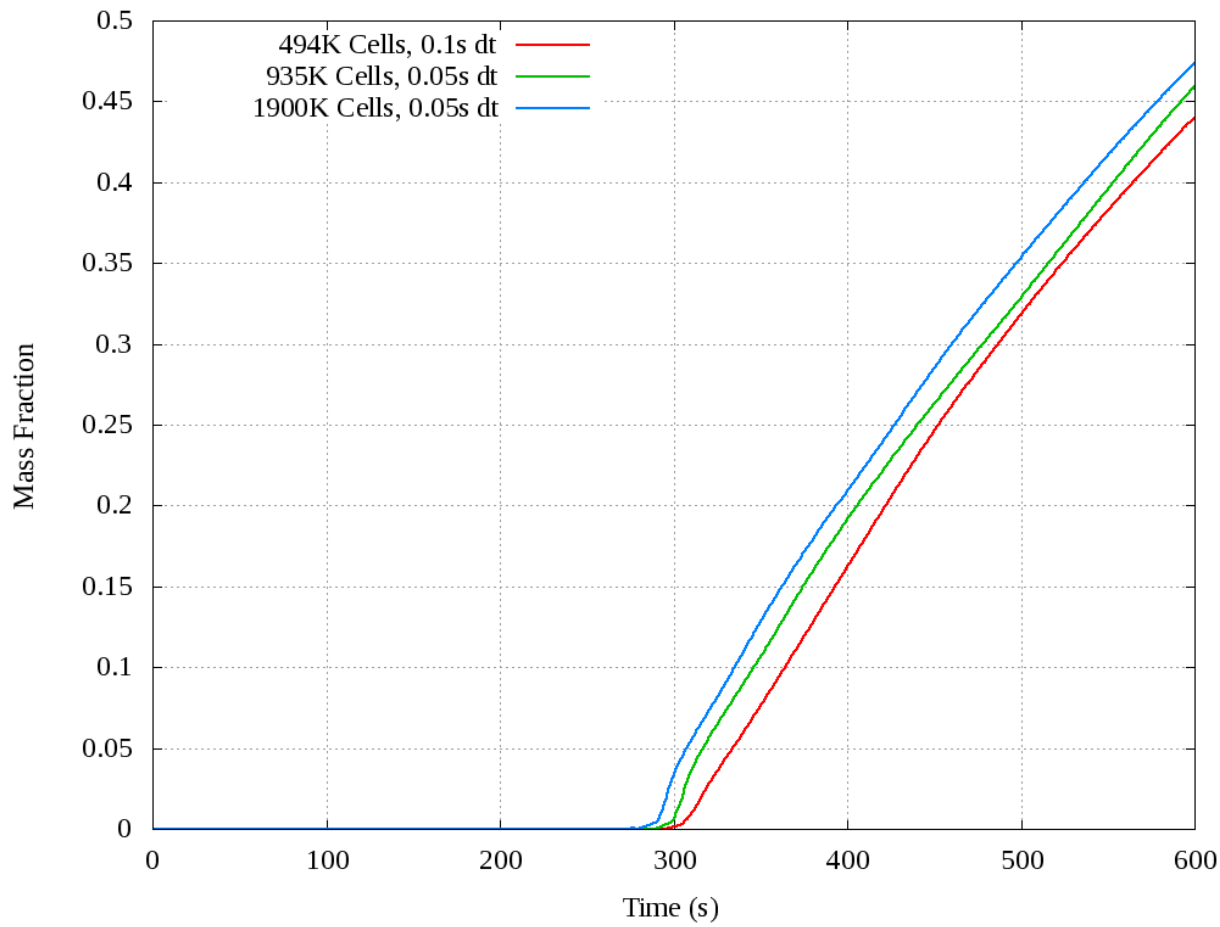

FIGURE E - 8 – SAMPLE RESULTS

Sample point 3 in the elbow after the first low horizontal section of the jumper.
The 935K cell solution approaches the 1900K cell solution while the 494K cell solution does not.

MEG Simulation Results

The test matrix called for MEG experiments and simulations with nominal flow rates of 1, 5, 10, and 20 gpm. The verification work was done at 1 gpm. The verified mesh and time step can be used in the 5, 10, and 20 gpm cases by scaling the time step so that the Courant number (velocity*time step/cell size) is unchanged for each simulation. So, if, for example, the velocity increases by 10-fold to go from the 1 gpm case to the 10 gpm case the time step should decrease by a factor of 10 to ensure that the mesh and time step are capable of resolving the flow features at the increased flow rate.

The MEG/water simulations have been run according to the test matrix. In all the simulations the MEG mass fraction was monitored at 14 sample points equating to those of the physical jumper. The nominal flow rates were 1, 5, 10, and 20 gpm. Actual flow rates from the pump flow vs. rpm curve were 0.8, 4.84, 9.97, and 20.35 gpm, respectively. The test matrix projected experiment run times of 2,280, 454, 227, and 114 s for the 1, 5, 10, and 20 gpm flow rates. Simulations were run concurrently with these experiments on the repaired jumper due to the long simulation run times (11 days each). The experimental flow rates and run times deviated somewhat from the test matrix. Therefore, the following comparisons of simulations and experiments were made at the simulated time when the volume of MEG/water injected to the jumper matches the volume injected during the experiment. Some 20 gpm experiments were performed, but hardware issues occurred such that the exact flow rates and run times are not known, rendering a comparison to simulation no more than a guess.

The simulations and experiments show qualitatively similar behavior in

Figure E - **9**. The 0.8 gpm MEG/water simulation shows the same behavior in the first downcomer as seen in video footage of the experiment: heavy MEG solution sliding down the pipe while water rises past it. The 4.84 gpm MEG/water simulation shows the same behavior in the low horizontal sections as seen in the experiment. In the first section, a heavy MEG layer extends along the bottom with a water layer above and then soon develops into a plug-like flow. In the second horizontal section there was a definite plug flow.

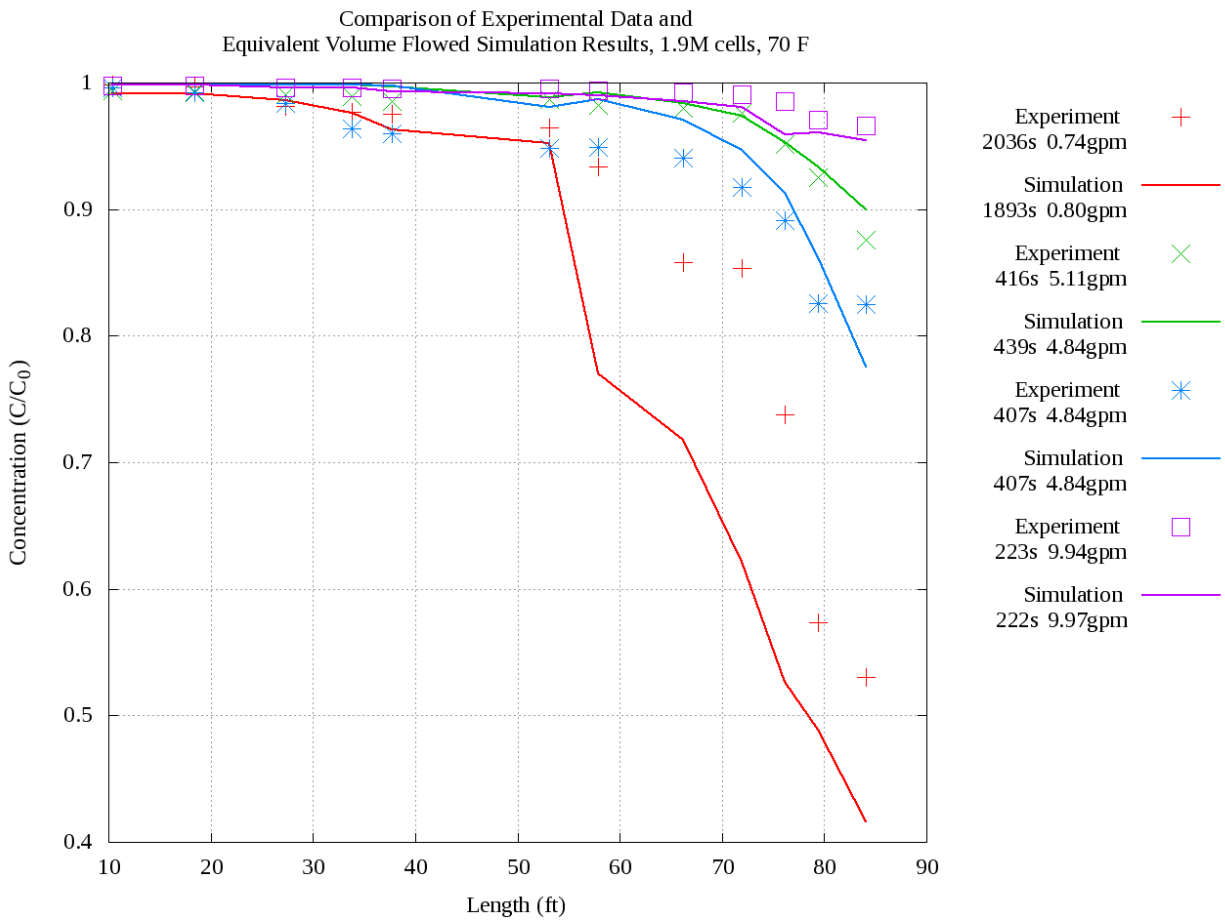

FIGURE E - 9 - COMPARISON OF MEG INJECTION EXPERIMENTS TO CORRESPONDING SIMULATIONS.

The 1 gpm nominal flow rate case was simulated with an expected flow rate of 0.8 gpm, but the experimental flow rate was off by 7.5 percent and was 0.74 gpm. The experiment ran for 2,036 s, and the comparable point in the simulation was at 1,893 s when an equivalent amount of MEG/water had been injected.

Figure E - **10** shows the simulation predicted the experiment well through point 8, but points 11 and 12 were off by around -28 percent and point 14 was off by -21 percent.

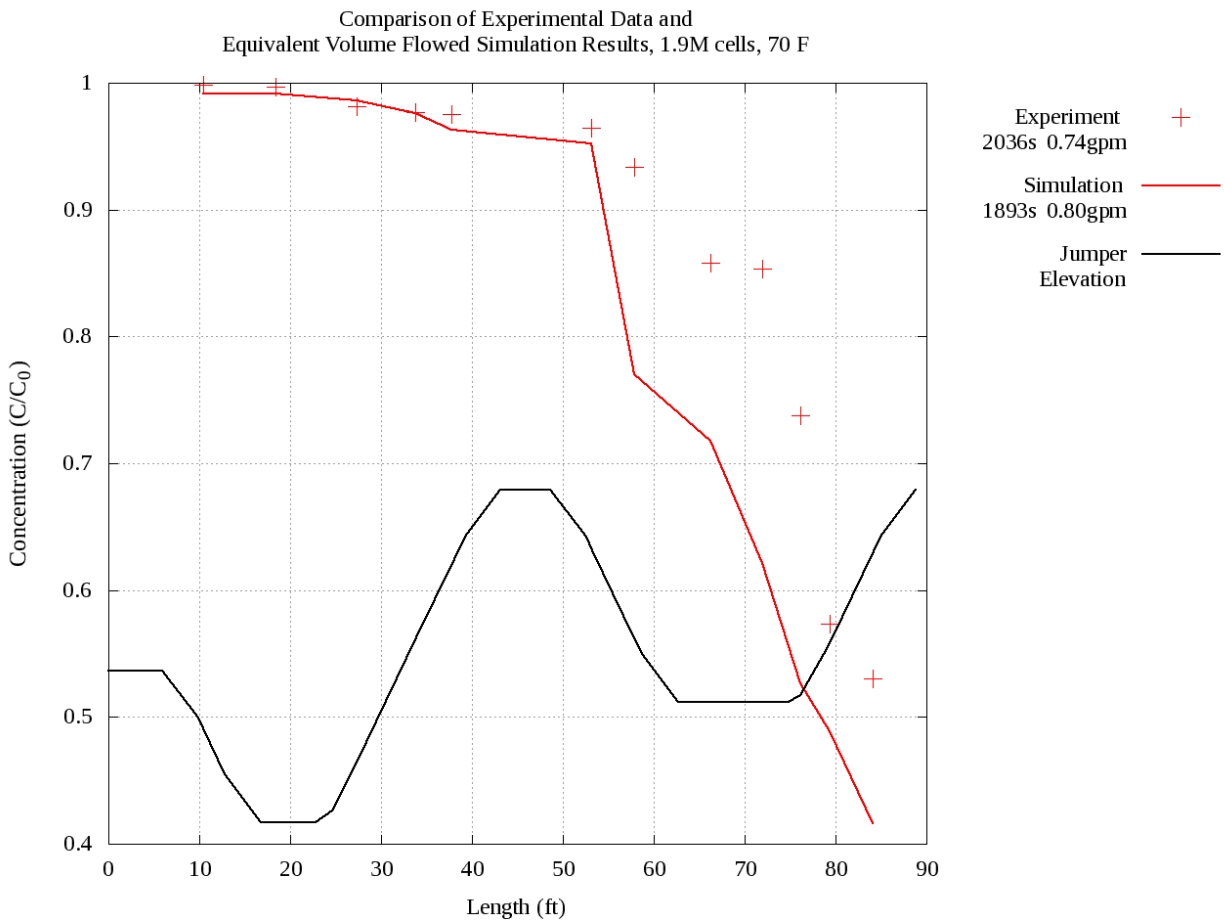

FIGURE E - 10 – MEG EXPERIMENT – 1 GPM

One gpm MEG experiment and simulation results agree qualitatively.

The experimental samples collected from the jumper were not all drawn simultaneously at the end of the experiment. Rather, they were drawn over the course of 15 minutes starting some small time after the pump was switched off and the graduate student could get back to the jumper. This allowed gravity settling to alter the concentration at some sample points more than others prior to collection. Extending the simulation time another 15 minutes with the injection flow rate set 0 gpm gives a different concentration profile within the jumper.

Figure E - **11** illustrates the change in concentration between the end of a 1 gpm run at 2,280 s and when the last sample is collected 15 minutes later. The greatest changes are in the high

horizontal section of the jumper and the downcomer and low horizontal section that follows it. The settling effect ranged from +4.3 to -4.6 percent, relative to the instantaneous samples at 2,280 s.

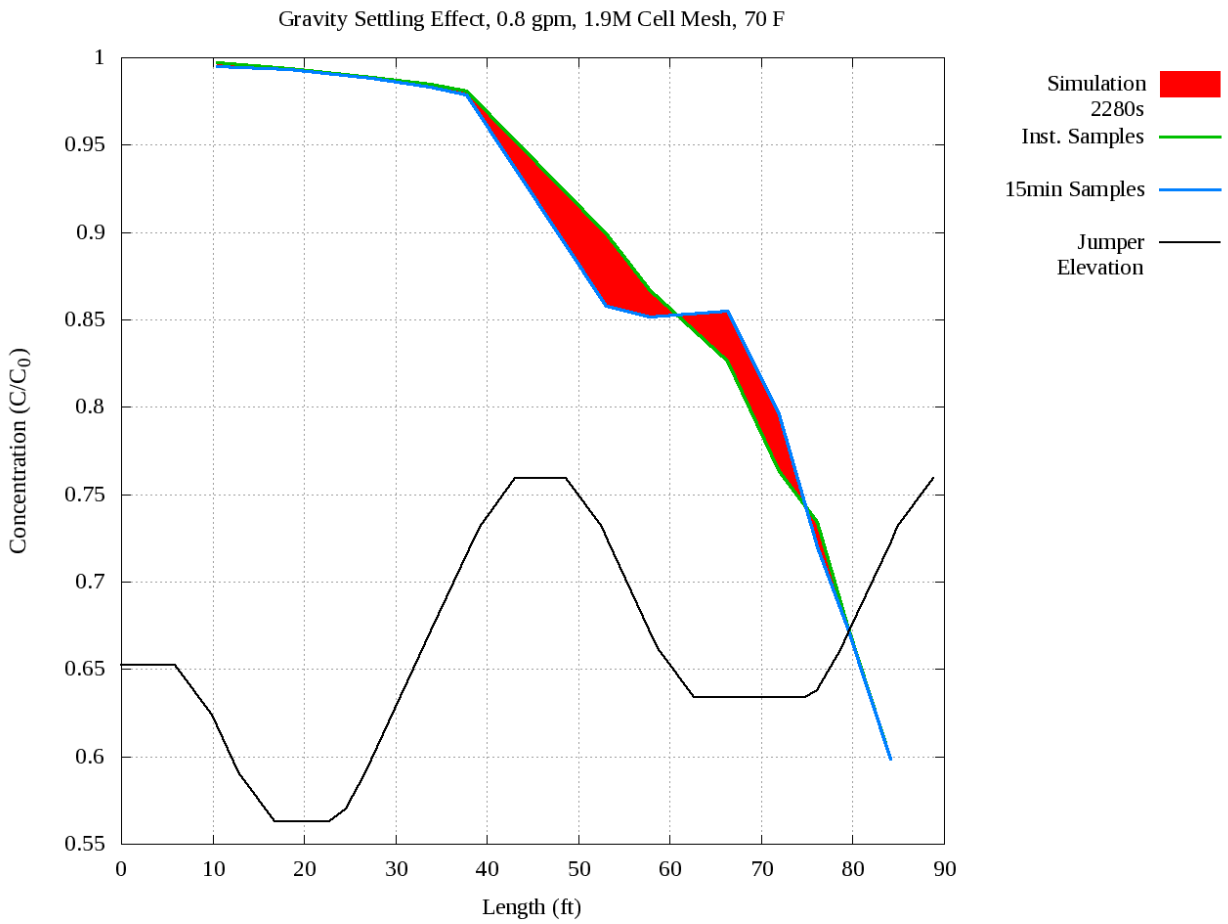

FIGURE E - 11 – GRAVITY SETTLING EFFECT

The 15 minutes over which the samples were collected allowed for gravity settling to alter the MEG concentration profile. The instantaneous sample reflect the concentration at 2280s when the flow was set to 0 gpm and the 15 min samples show the concentration in the jumper after 15 minutes.

The 5 gpm nominal flow rate case was simulated with an expected flow rate of 4.84 gpm. In one case the experimental flow rate was off by 5.6 percent and was 5.11 gpm. In the other case, the expected flow rate of 4.84 gpm was achieved. The experiment with 5.11 gpm flow rate ran for 416 s, and the comparable point in the simulation was at 439 s when an equivalent amount of MEG/water had been injected. The simulation predicted the experiment well, as the discrepancy between the simulation and experiment ranged from -0.3 to 2.8 percent. The experiment with a

4.84 gpm flow rate ran for 407 s, and the comparable point in the simulation was at 407 s when an equivalent amount of MEG/water was injected. The simulation predicted the experiment well as the discrepancy between the simulation and experiment ranged from -6 to +4.3 percent.

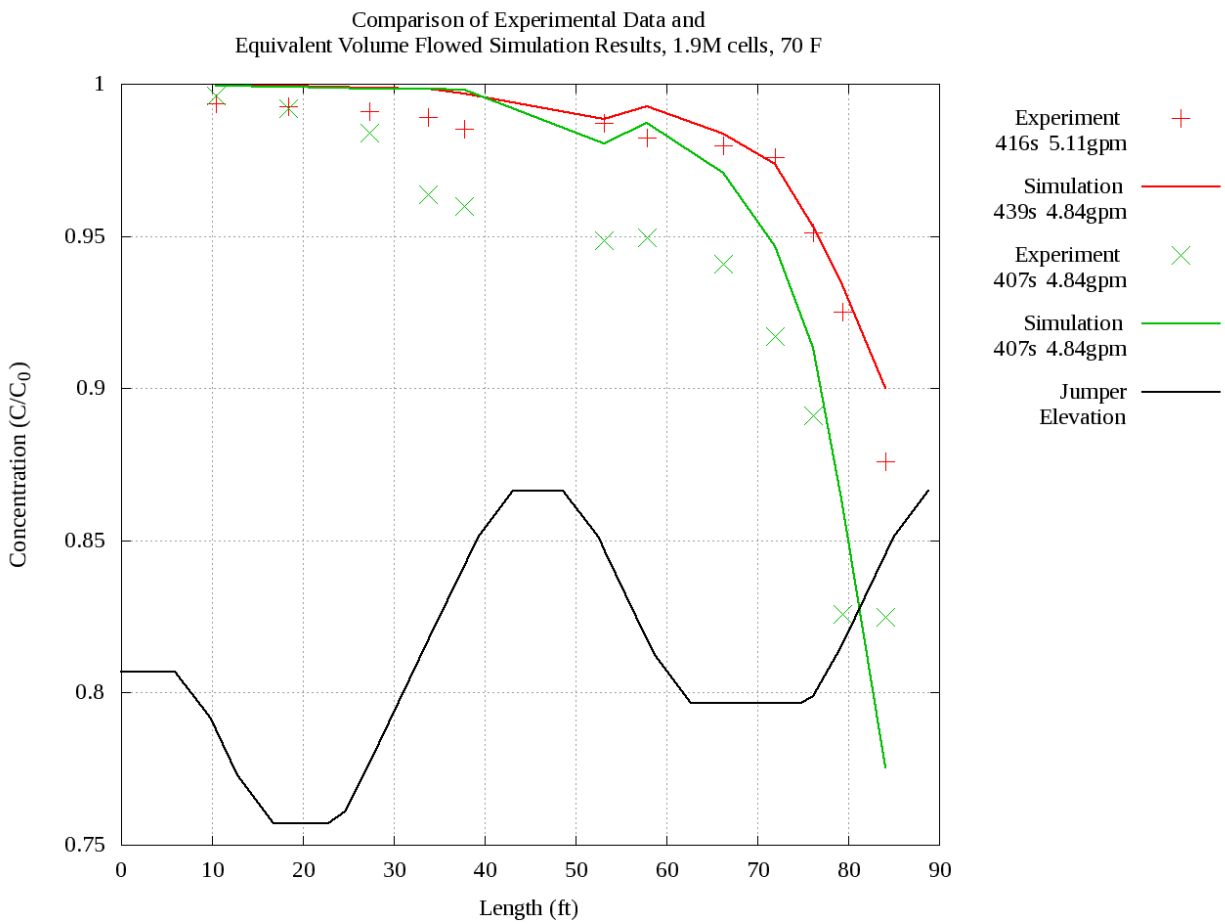

FIGURE E - 12 – MEG SIMULATIONS AND EXPERIMENTS AT 5 GPM

The MEG simulations and experiments at 5 gpm compare both qualitatively and quantitatively well. The differences between experiment and simulation range from 4.3 to -6%.

Figure E - **13** shows that the possible concentration change due to simulated settling in the 5 gpm case ranged from +2.1 to -0.3 percent, relative to the instantaneous samples at 454 s. The settling effect decreased, relative to 1 gpm, because the variation in concentration was much smaller when the pump was switched off. The normalized concentration at 454 s only ranged from 0.93 to

1.0. However, the experimental data had a larger concentration range (0.825 to 1.0) than the 5 gpm settling simulation. So it appears that the actual settling effect in the 5 gpm experiments was approximately 3 percent, or so - greater than the simulated values for 5 gpm, but less than that of the 1 gpm simulation. This means that the settling effect might account for almost half of the discrepancy between the simulation and the experiment at 4.84 gpm.

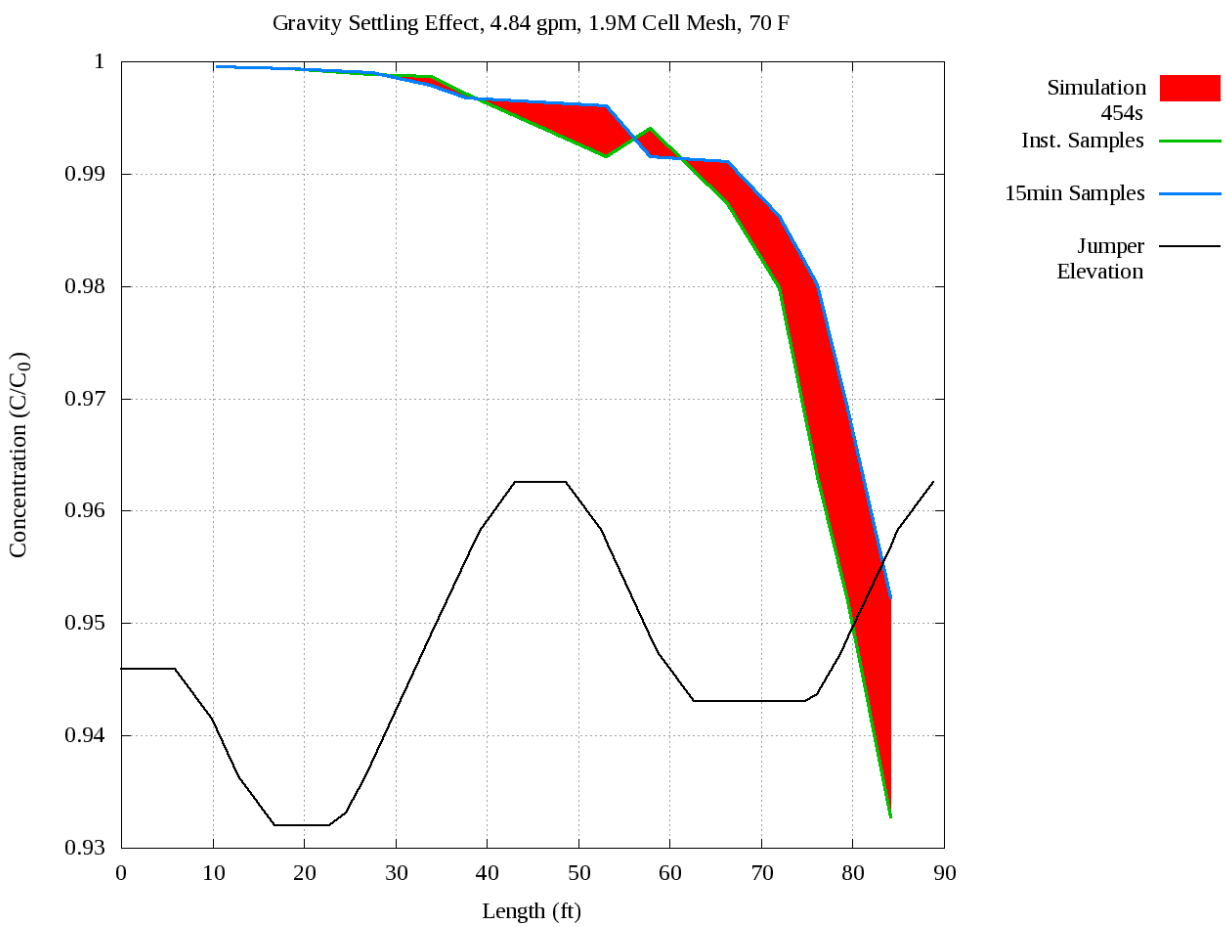

FIGURE E - 13 – GRAVITY SETTLING EFFECT – 2% CONCENTRATION CHANGE

The 2% concentration change predicted by the settling simulation for the 5 gpm MEG gives a lower bound on since the variation in concentration from 0.93 to 1.0 at 454 s is less than that seen experimentally (0.825 to 1.0).

The 10 gpm nominal flow rate case was simulated with an expected flow rate of 9.97 gpm. The experimental flow rate was very near the expected value of 9.94 gpm, off by only 0.3 percent.

The experiment ran for 223 s, and the comparable point in the simulation was at 222 s when an equivalent amount of MEG/water was injected.

Figure E - **14** shows that the simulation predicted the experiment well, as the discrepancy between the simulation and experiment ranged from -2.6 to 0.1 percent.

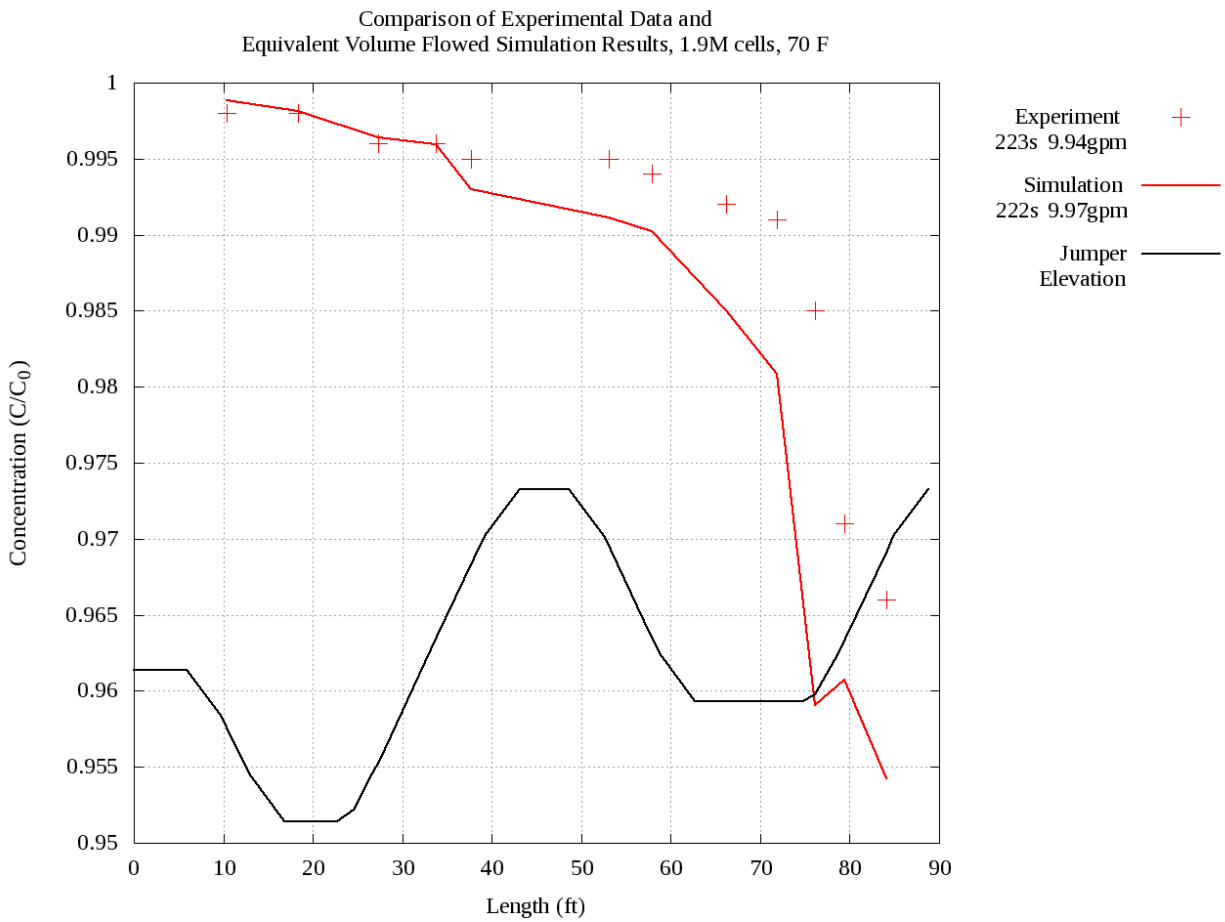

FIGURE E - 14 – MEG EXPERIMENT AND SIMULATION AT 10 GPM

The MEG experiment and simulation at 10 gpm match very well, as the difference between the two ranges from -2.6 to 0.1%.

The settling effect ranges from +1.3 to -0.3 percent in

Figure E - **15**. As in the 5 gpm case, the small amount of change stems from the small variation in the concentration throughout the jumper at the end of the 10 gpm simulation. Once again, the settling effect may account for around half the difference between the simulation and the experiment.

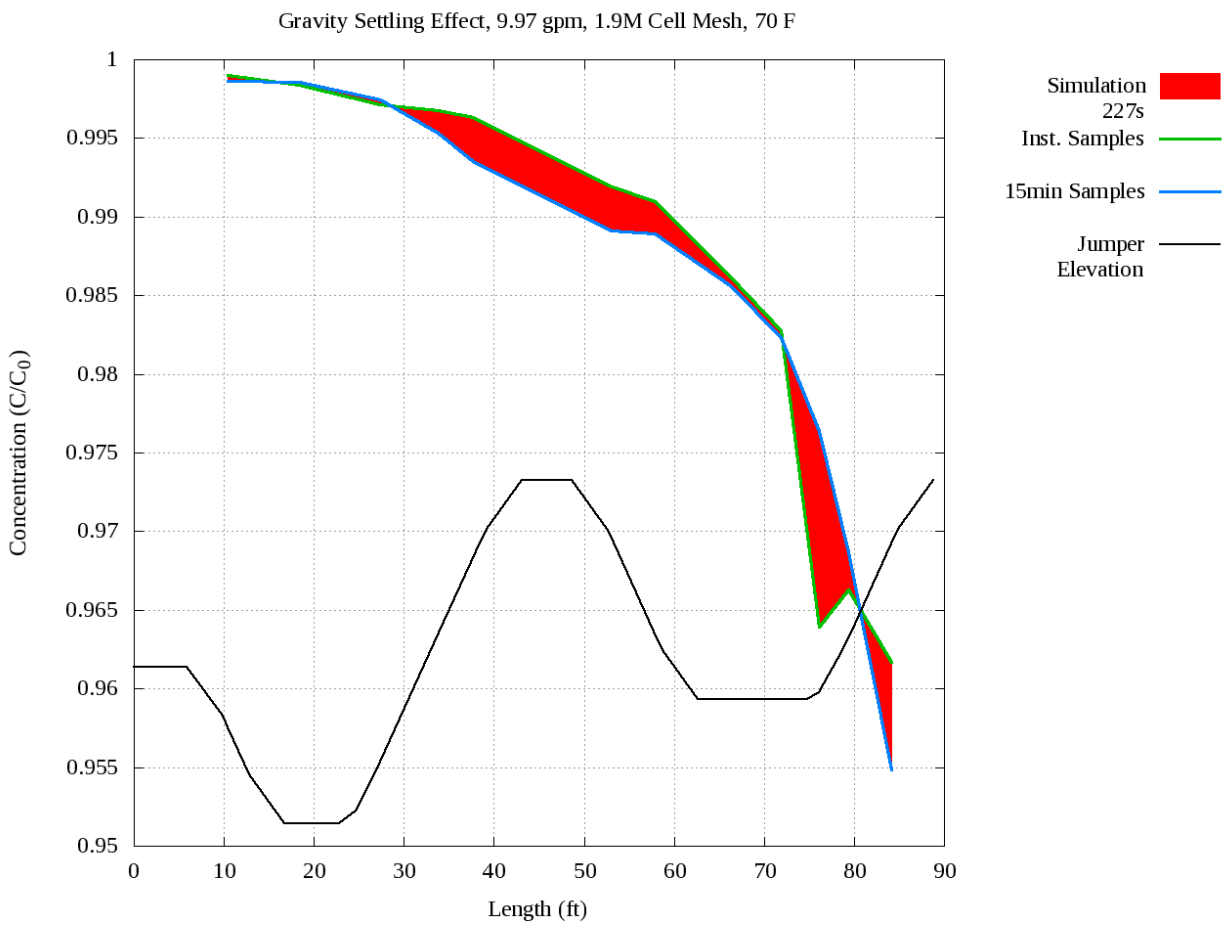

FIGURE E - 15 – GRAVITY SETTLING EFFECT

The settling effect after injecting 10 gpm MEG is small, about 1.3%, because the concentration along the jumper only varies between 0.96 and 1.0 at the end of the simulation.

The 20 gpm experiments lacked exact flow rates and pumping times, so an accurate comparison could not be made, although the simulation was run at the conditions specified in the test matrix.

Figure E - **16** shows that the settling effect ranges from +1.7 to -1 percent.

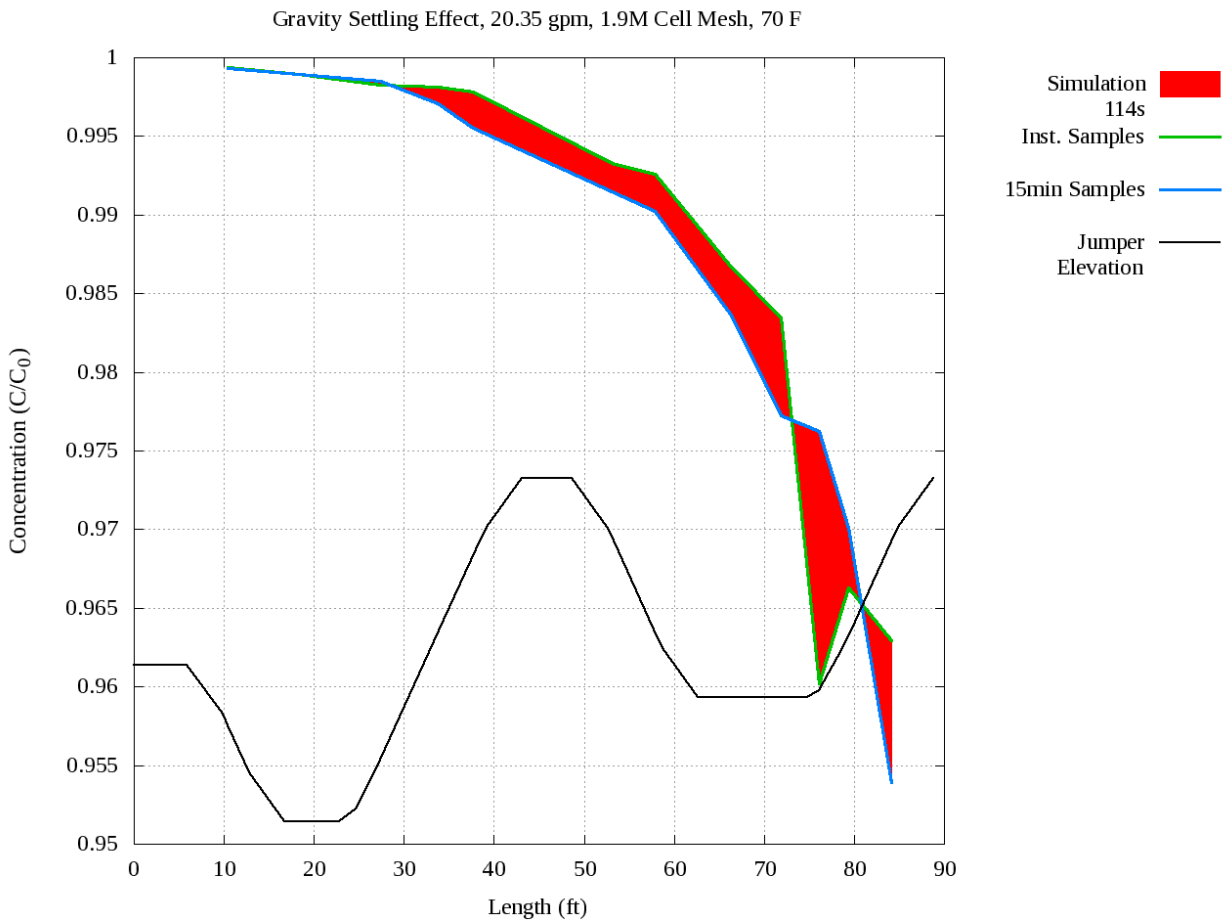

FIGURE E - 16 – MEG EXPERIMENTS AT 20 GPM

The MEG experiments at 20 gpm lacked sufficient detail to make a comparable simulation. The settling effect was small: 1.7% to -1%.

MeOH Results

Methanol/water simulations have also been run at nominal flow rates of 1, 5, 10, and 20 gpm. Actual flow rates from the pump flow vs. rpm curve were 1.22, 5.35, 20.21, and 20.49 gpm, respectively. The expected experiment run times were 1,718, 388, 211, and 113 s for the respective 1, 5, 10, and 20 gpm flow rates. Some of the experimental results had slightly different flow rates and run times. The following comparisons of simulations and experiments were made at the simulated time when the volume of MeOH/water injected to the jumper matched the volume injected during the experiment.

The MeOH simulations did not match the experiments as well as the MEG simulations did.

Figure E - **17** shows all the MeOH simulations and experiments on a single plot. The horizontal regions were particularly different between the MeOH simulations and experiments because there should have been two layers, one methanol rich and the other water rich, according to the experiments, but the simulation did not have the two layers at the end. The simulations did show two layers in the horizontal sections early in the run, but the layers disappeared prematurely. Aside from the horizontal sections and the last two sample points at 1 gpm, the simulations and experiments were within 10 percent of one another.

Figure E - **18** to

Figure E - **21** show the nominal flow rates and matched experimental data individually.

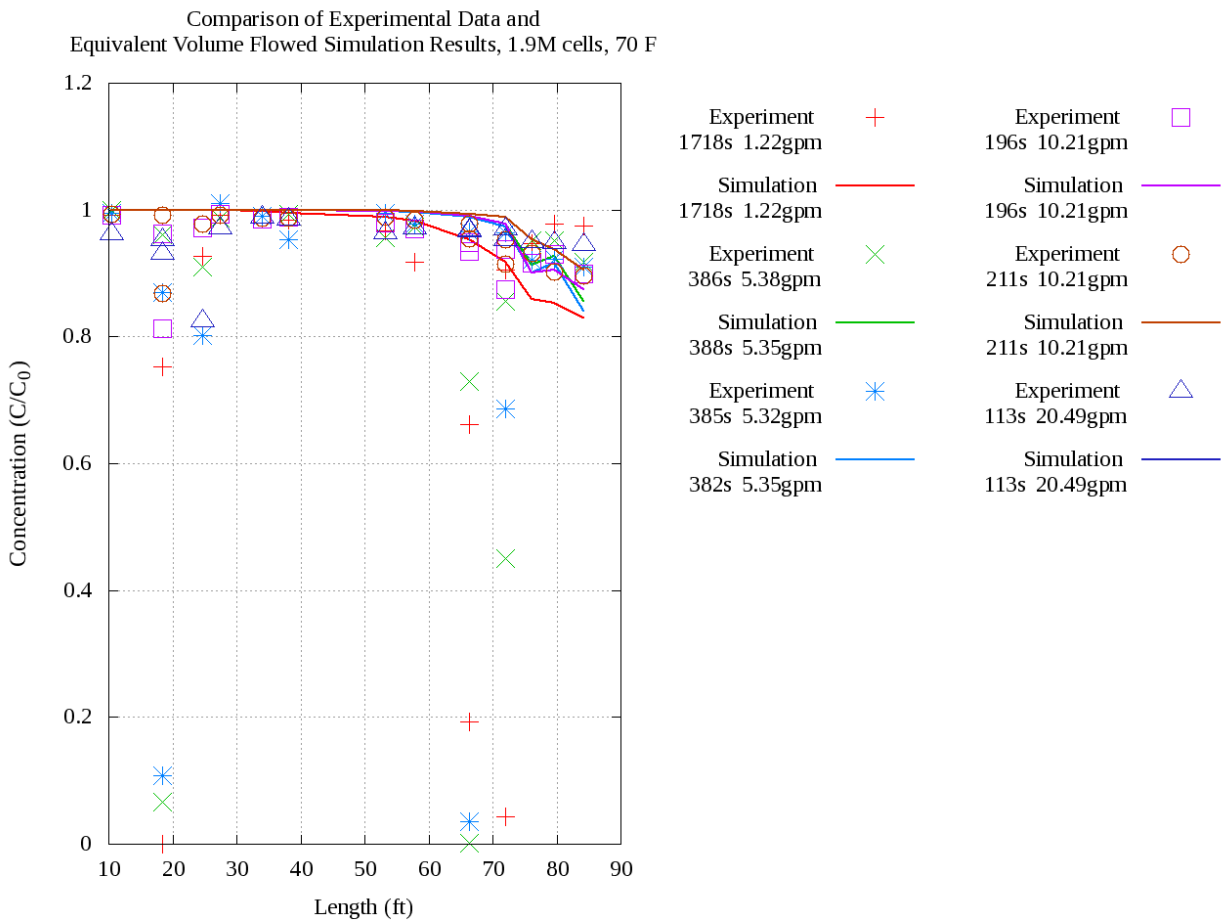

FIGURE E - 17 – METHANOL SIMULATION RESULTS

Methanol simulation results did not reproduce the low concentrations seen in the experiments. The low MeOH concentrations reflect a stationary water rich phase below a flowing MeOH rich upper layer in the lower horizontal sections.

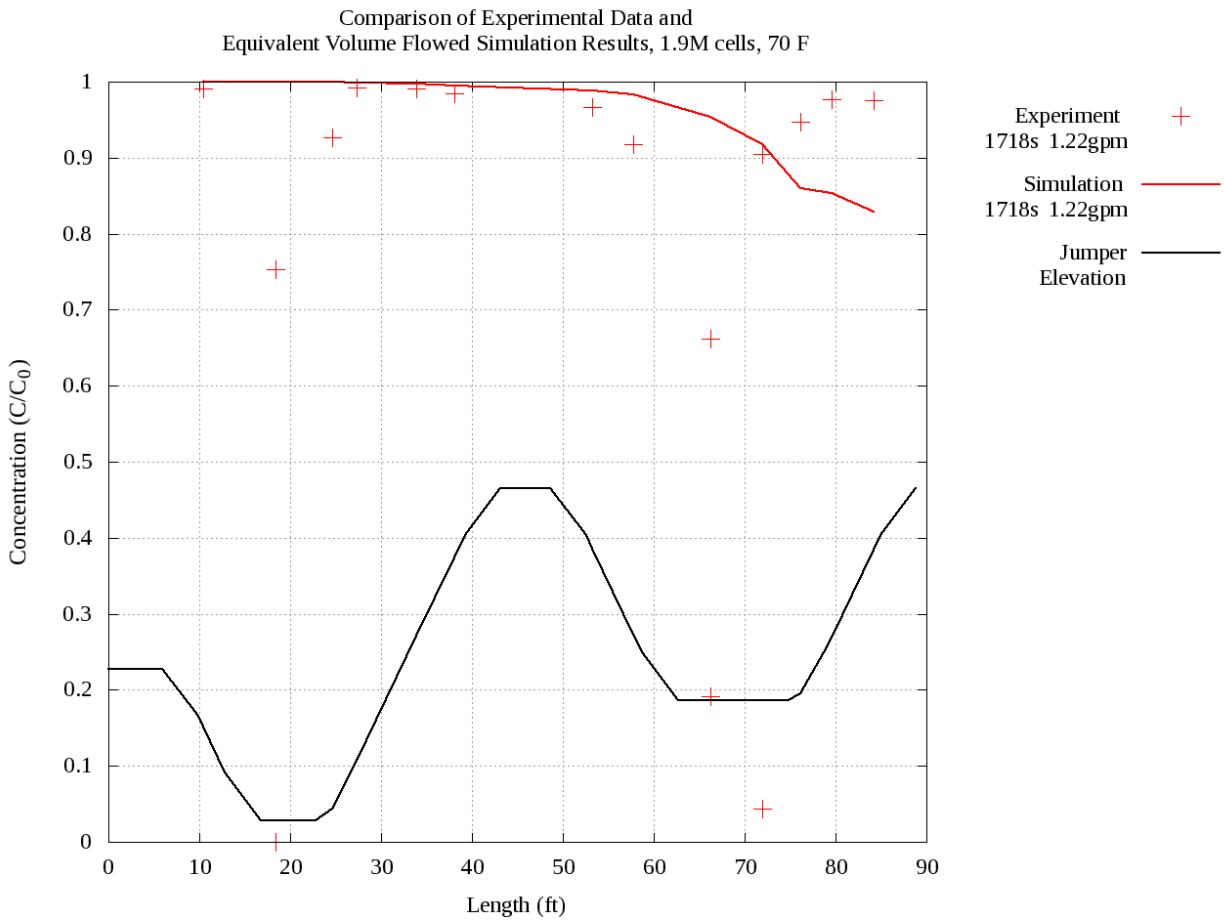

FIGURE E - 18 – 1 GPM MEOH SIMULATION

The 1 gpm MeOH simulation had two layers in the horizontal sections early in the run, but they disappeared by the end as shown here.

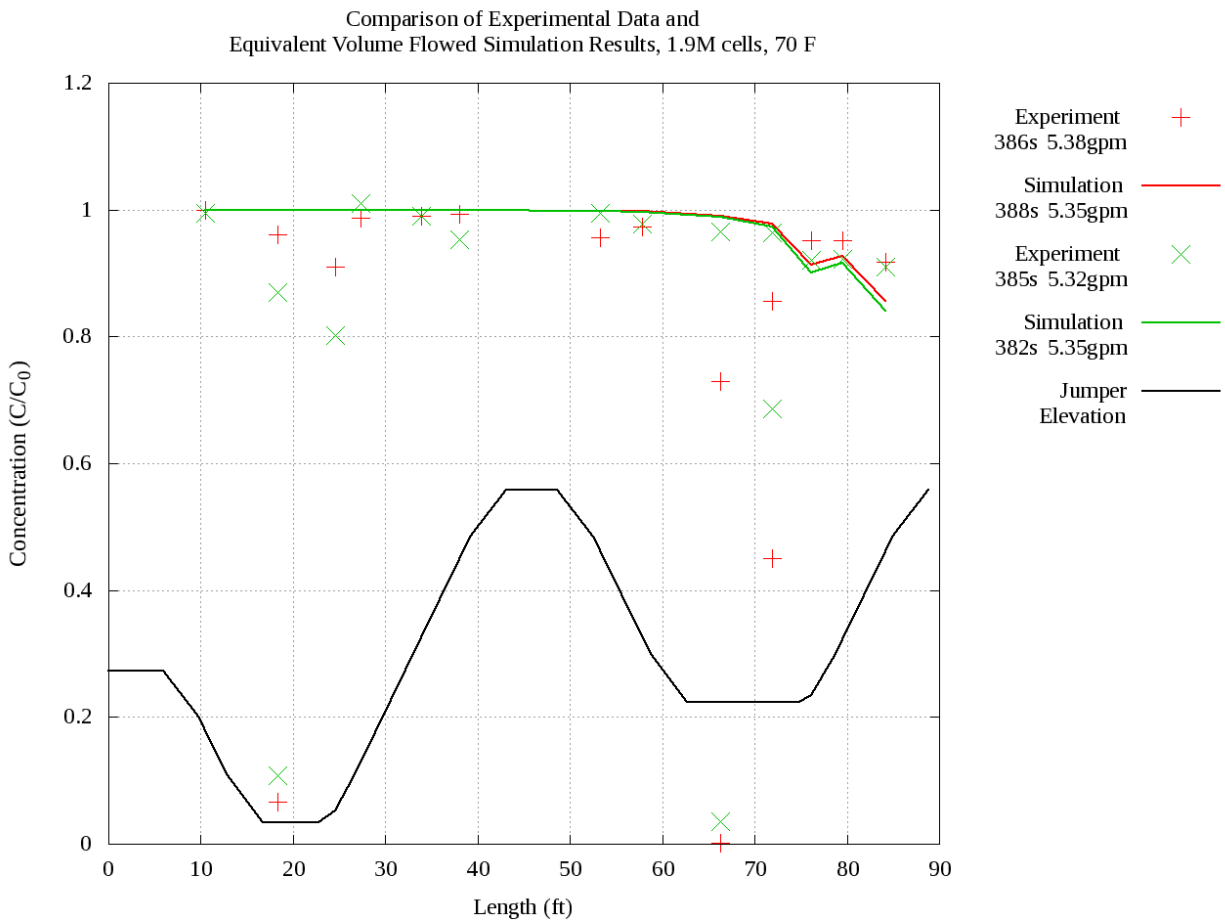

FIGURE E - 19 – 5 GPM MEOH SIMULATION

The vertical sections of the5 gpm MeOH simulation appear similar to the experiments, but the two layers in the horizontal sections were not present at the end of the simulation.

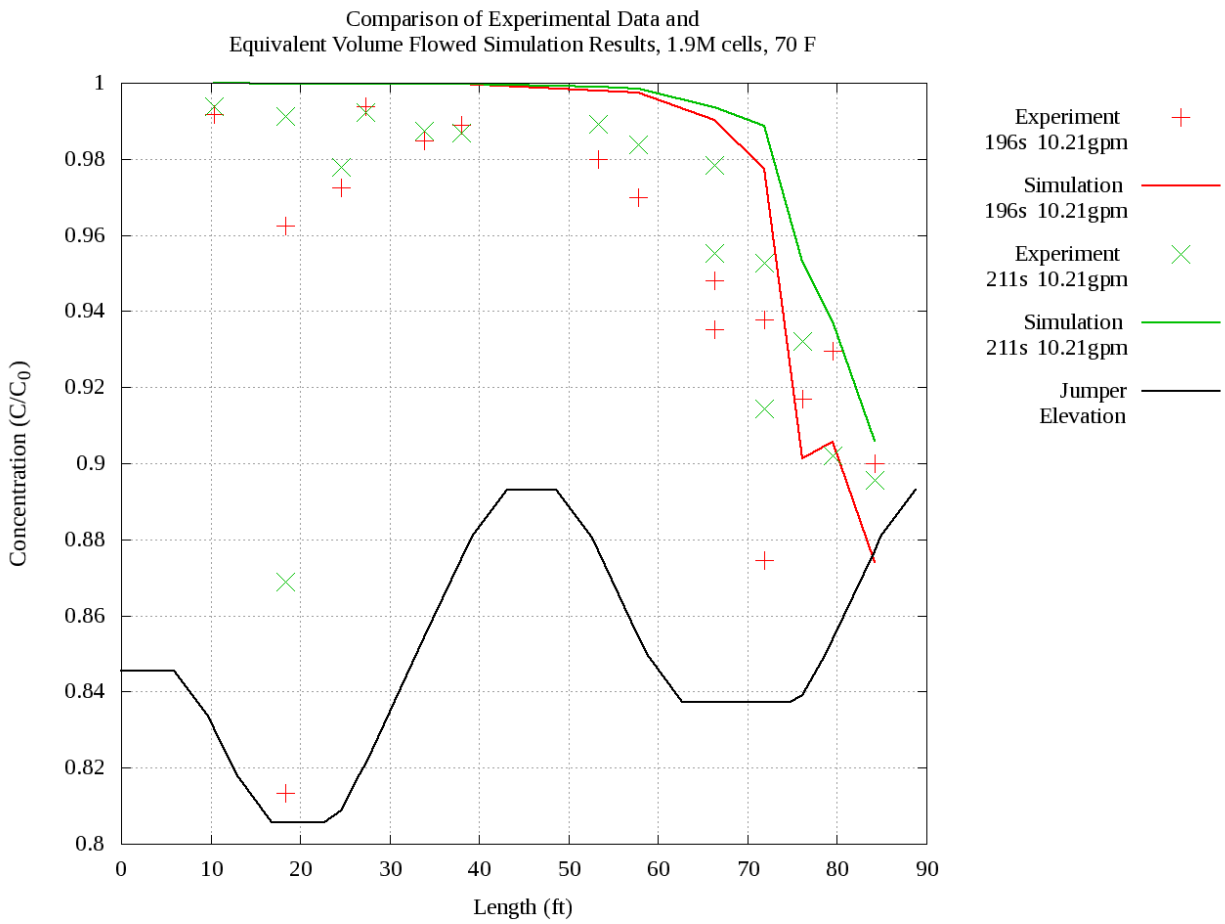

FIGURE E - 20 – 10 GPM MEOH SIMULATION

The 10 gpm MeOH simulations had the same difficulty as the 1 and 5 gpm simulations. The two layers in the horizontal sections were missing at the end of the simulation.

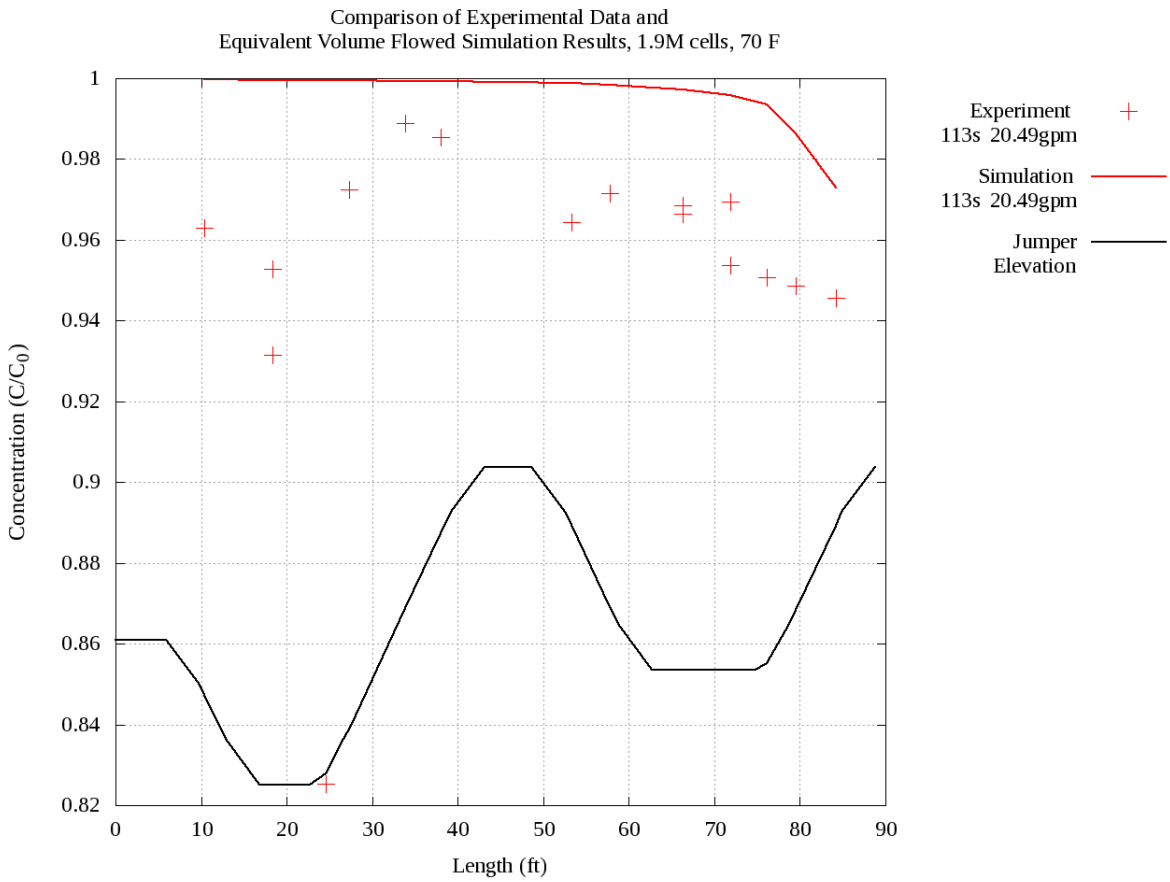

FIGURE E - 21 – 20 GPM MEOH SIMULATION

The 20 gpm MeOH simulation does not properly predict the two layers in the horizontal sections at the end of the simulation, just like the other MeOH simulations.

The early dissipation of the stratified flow in the horizontal sections of the MeOH simulations suggested that there was too much dispersion in the simulations, relative to what occurs physically in the experiments. It was unlikely that the fluid properties were the cause of this extra dispersion. The properties of MeOH/water solutions were not available at a range of temperatures, but the MEG properties were. Temperature sensitivity simulations done with the MEG simulation showed only ± 2.0 percent change or less in the concentration profile along the jumper when decreasing the temperature from 70°F to 50°F or increasing the temperature to 100°F from 70°F.

The excessive dispersion probably arose from the k-Ω turbulence model or from limitations imposed by discretization. The effect of alternate turbulence models was tested on a reduced

physical domain to shorten the computation time. The reduced domain stopped at the top of the first riser. Except for changing the turbulence model, all other conditions and fluid properties were kept the same. Results from the abbreviate domain with the different models are shown in Figure E - 22. A detached eddy simulation (DES) was used to try to improve on the turbulence modeling. The DES results still had two distinct layers at the end of the simulation, an improvement over the k- Ω results. However, the lower layer in the DES results had far too much MeOH relative to the experiment. The experimental dimensionless measurement was 0 MeOH, while the MeOH content of the DES simulation ranged from 0.3 to 0.65, depending on the relative location within the lower layer.

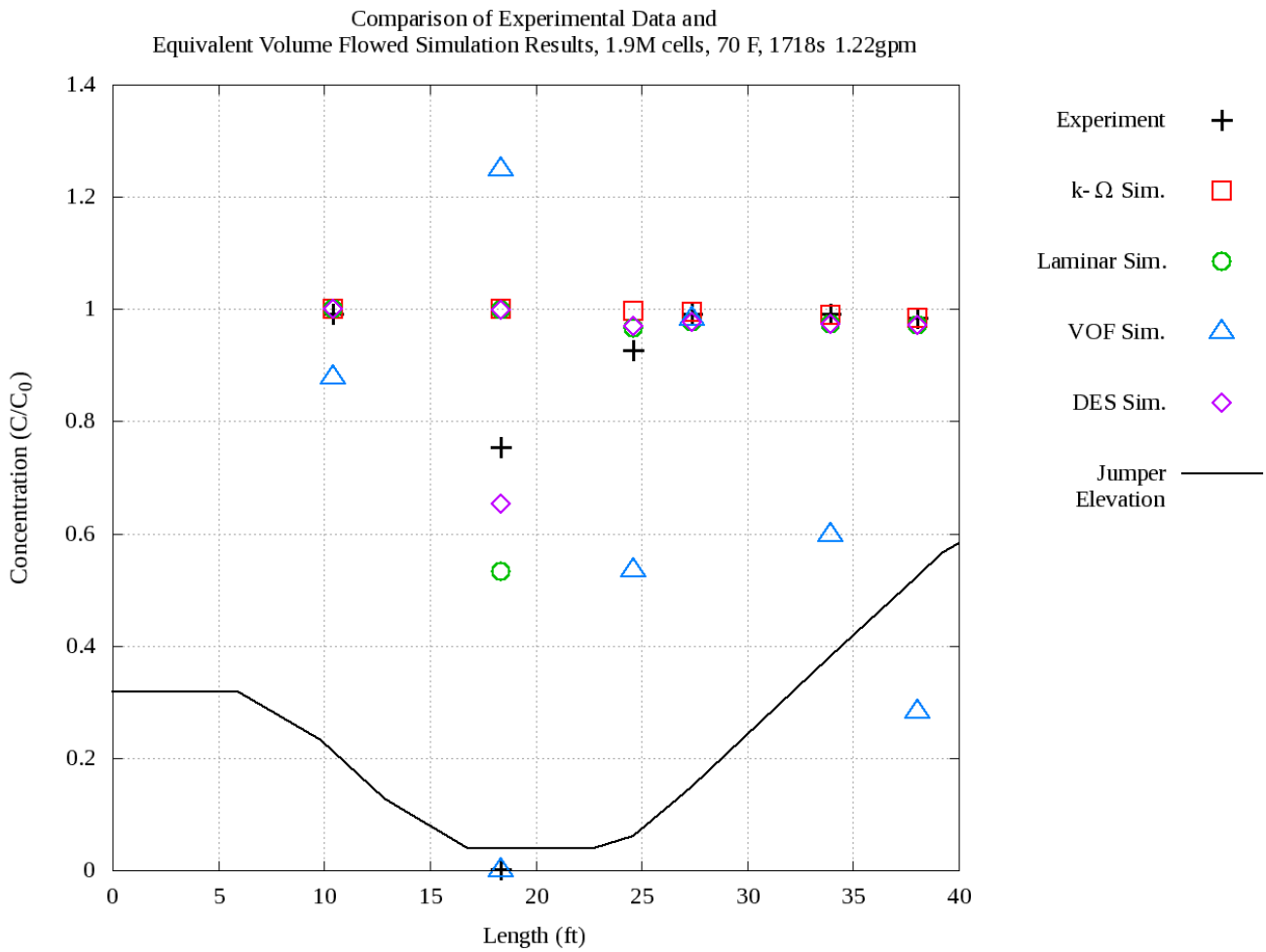

FIGURE E - 22 – COMPARISON OF EXPERIMENTAL DATA AND EQUIVALENT VOLUME FLOWED SIMULATION RESULTS

Testing multiple models suggested that there was too much turbulent dispersion in the k-o and DES simulations.

Although the laminar simulation had no turbulence, it too failed correctly predict the MeOH concentration in the horizontal section. The VOF model captured the interface between the layers in the horizontal section, but did not allow for correct mixing in the vertical sections.

A laminar simulation was also run to eliminate the turbulence model completely along with any effects it may have had on the simulation. Although the laminar simulation produced two layers in the horizontal section at the end of the simulation, the concentration in the horizontal section of the laminar simulation still deviated from the experiment, with a MeOH concentration in the water layer ranging from 0.18 to 0.53.

Having removed turbulence, but not remedied the discrepancy between the simulation and the experiments, it was likely that the problem was either a faulty/incorrect sub-grid fluid-fluid interaction model or a discretization error. Simulating the mixing of the MeOH and water with a turbulent volume of fluid (VOF) method provided insight on both of those counts because it treated the methanol and water as separate, immiscible phases and was designed to capture phase interfaces on meshes where the cells are larger than the thickness of the interface. The VOF simulation successfully reproduced the stationary water layer with no MeOH seen in the experiment, but it did not accurately match the experimental results in the vertical sections of the jumper.

Considering the results of the alternate models together points to the current discretization scheme inadequacy for the fluid models available in Star-CCM+. A more refined mesh with cells small enough to capture the concentration gradient at the water rich/MeOH rich interface would require far too much computation time to be useful for troubleshooting or production simulations. Developing and testing alternative sub-grid fluid-fluid interaction models similar to the VOF model but with capabilities to handle both the horizontal and vertical sections properly would exceed both the scope and budget of the current project.